Phenomenology of alternative gravity models from galactic kinematics

Submitted in partial fulfillment of the requirements
of the degree of

Doctor of Philosophy

by

Esha Bhatia
(Roll No. 196121010)

Supervisors:
Sovan Chakraborty
Sayan Chakrabarti

Department of Physics
INDIAN INSTITUTE OF TECHNOLOGY GUWAHATI
2024

Esha Bhatia
Roll No. 196121010
Department of Physics
Indian Institute of Technology Guwahati
Guwahati, India
email: b.esha@iitg.ac.in

Declaration

I hereby declare that works presented in the thesis entitled "**Phenomenology of alternative gravity models from galactic kinematics**" have been carried out by me under the supervision of **Dr. Sovan Chakraborty and Dr. Sayan Chakrabarti** at the Department of Physics, Indian Institute of Technology Guwahati, India. The thesis has not been submitted anywhere else for any degree. Works presented in the thesis are all my own unless referenced to the contrary in the thesis.

Date: 31-01-2025

Signature

Certificate

Dr. Sovan Chakraborty
Associate Professor
Department of Physics
Indian Institute of Technology Guwahati
Guwahati, India
email: sovan@iitg.ac.in

It is certified that the work contained in the thesis entitled "**Phenomenology of alternative gravity models from galactic kinematics**" by Ms. Esha Bhatia (Roll No. - 196121010), a Ph.D. student in the Department of Physics, Indian Institute of Technology Guwahati is carried out under my supervision and has not been submitted elsewhere for the award of any other degree.

Signature

Date: 31-01-2025

Certificate

Dr. Sayan Chakrabarti
Associate Professor
Department of Physics
Indian Institute of Technology Guwahati
Guwahati, India
email: sayan.chakrabarti@iitg.ac.in

It is certified that the work contained in the thesis entitled "**Phenomenology of alternative gravity models from galactic kinematics**" by Ms. Esha Bhatia (Roll No. - 196121010), a Ph.D. student in the Department of Physics, Indian Institute of Technology Guwahati is carried out under my supervision and has not been submitted elsewhere for the award of any other degree.

Date: 31-01-2025

Signature

Acknowledgements

With the culmination of my rewarding five-year Ph.D. journey, I express my sincere gratitude to the individuals who enriched this experience and contributed to its success.

I am deeply indebted to my thesis advisors, Dr. Sovan Chakraborty and Dr. Sayan Chakrabarti, for their unwavering support, insightful mentorship, and invaluable expertise. Their guidance and stimulating discussions were instrumental in shaping this research and fostering my academic growth. I am truly fortunate to have worked with them, and I look forward to continuing our collaboration.

I also extend my sincere appreciation to my doctoral committee—Dr. Debaprasad Maity (Chair), Dr. Subhaditya Bhattacharya, and Dr. Bibhas Ranjan Majhi—for their insightful feedback and constructive criticism. Their thoughtful questions and expert guidance were invaluable in refining this work. I am particularly grateful to Dr. Maity for his leadership and support. I appreciate the time and effort invested by the anonymous reviewers, whose feedback, though challenging at times, ultimately resulted in a stronger and more impactful contribution.

I would also like to acknowledge the significant contributions of Dr. Arunansu Sil, Dr. PK Giri, Dr. Charudatt Kadolkar, Dr. Bibhas Ranjan Majhi, and Dr. M.C. Kumar, with whom I had the privilege of working as a teaching assistant. Their encouragement and intellectually stimulating discussions were a vital part of my development, and I especially thank Dr. Kadolkar for his motivating influence and his excellent explanations of the complex topics.

I am grateful to the past and present Heads of the Department of Physics—Prof. Bosanta Ranjan Boruah, Prof. Subhradip Ghosh, and Prof. Perumal Algarswamy—for cultivating an environment that fosters academic excellence. Their leadership and support were deeply appreciated.

I thank the Department of Physics and my institution for providing the necessary resources and infrastructure for my research. I am particularly grateful to Sidananda and Basab sir for their invaluable assistance in navigating departmental processes and resolving various challenges.

My heartfelt thanks go to my research group members, Madhurima Chakraborty, Prantik Sam-

rah, Tarun, Soumen, and Dikshit for their encouragement and support, which served as a constant source of motivation.

I am deeply grateful to my batchmates and hostel friends for their camaraderie and support. Their friendship made this journey both enjoyable and memorable.

To my family, my most heartfelt thanks. Their unwavering belief in me, even during the most tumultuous times, provided the strength and encouragement I needed to persevere. This accomplishment would not have been possible without their constant love and support.

Finally, I extend my sincere gratitude to everyone who contributed to this academic journey, whether mentioned explicitly or not. Your support, guidance, and encouragement were essential to the successful completion of my Ph.D. thesis.

Abstract

The observations across different scales of the Universe often diverge from the predictions of General Relativity. These discrepancies between theoretical expectations and observational data leave a large room to explore and study alternative gravity models. Therefore, the phenomenological analysis of alternative gravity theories at astrophysical scales also becomes crucial for assessing their consistency. In this thesis, we explore a few alternative gravity models in the galactic scales expanding into two regimes: the ultra-diffuse galaxies (UDGs) and the rotationally supported galaxies. For the former, we study the velocity dispersion data from three UDGs. For the latter, we analyze the galaxy rotation velocities from the Spitzer Photometry and Accurate Rotation Curves (SPARC) database. For UDGs, the alternative gravity model parameters are statistically fitted to the velocity dispersion (VD) observations. Observed UDGs like NGC1052-DF2 and NGC1052-DF4, which exhibit minimal dark matter and align with Newtonian dynamics, are analyzed using a couple of $f(R)$ gravity models and Renormalization Group correction to General Relativity (RGGR). For this, we assume that the motion of galaxies within the cluster follows isotropic motion, i.e., the radial and tangential anisotropy components are equal. The chosen gravity models are consistent with the observational VD of both the UDGs when parameters are constrained locally and globally. The same analysis is extended to the dark matter-dominated UDG, NGC1052-DF44, however here we focus on the radial anisotropy of the VD. In particular, for NGC1052-DF44, we compare three alternative gravity models-Modified Newtonian Dynamics (MOND), $f(R)$ gravity, and RGGR with a dark matter scenario modeled using a Navarro-Frenk-White (NFW) halo and investigate the role of anisotropy in explaining modified kinematics. We find that only two alternative gravity models out of the three considered, viz. MOND and RGGR remain competitive with the NFW DM profile. Additionally, the anisotropic VD scenario with constant anisotropy suggesting a tangential motion is found to be statistically comparable with the conventional isotropic motion. Moving ahead to the second part of the thesis, we use the SPARC data and examine the galactic kinematics

under two alternative gravity frameworks: RGGR and a Yukawa Modified Gravity (YMOG). YMOG considers a general Yukawa term added to the Newtonian gravity model. We analyze the consistency of these models and investigate how the free-model parameters correlate with galaxy morphology. Additionally, we assess the goodness of fit using the standard empirical relations such as the Radial Acceleration Relation (RAR) and the Baryonic Tully-Fisher Relation (BTFR). Our analysis shows that both models, that is, RGGR and YMOG, compete well with an alternative NFW DM model.

Contents

List of Abbreviations

RC	Rotation Curve
SPARC	Spitzer Photometry for Accurate Rotation Curve
ΛCDM	Λ Cold Dark Matter
GR	General Relativity
E-H	Einstein Hilbert
DM	Dark Matter
JWST	James Web Space Telescope
NFW	Navarro Frank White
VD	Velocity Dispersion
UDG	Ultra-Diffuse Galaxies
RGGR	Renormalization Group correction to General Relativity
MOG	Modified Gravity
MOND	Modified Newtonian Dynamics
EFE	External Field Effect
RAR	Radial Acceleration Relation
BTFR	Baryonic Tully Fisher Relation
LSB	Low Surface Brightness
H	Hubble type
Q	Quality factor
MCMC	Monte Carlo Markov Chain
BIC	Bayesian Inference Criteria

Chapter 1

Introduction

General Relativity (GR), proposed by Einstein in 1915 [1] is a theory of gravity that describes the curvature of spacetime caused by mass and energy, offering important insights across different scales [2, 3]. On a local scale, such as our solar system scales, GR explains phenomena like Mercury's perihelion precession, gravitational time dilation critical for GPS accuracy, and light deflection observed during solar eclipses. On astrophysical scales, GR governs the behavior of extreme compact objects such as black holes (BH) and neutron stars (NS), predicting phenomena like accretion disks, relativistic jets, and gravitational waves (GW) from binary BH-BH, BH-NS or NS-NS mergers [4, 5], and generating the image of the BH at the center of the M87 and Sgr A^* galaxies [6]. On cosmological scales, GR underpins the structure and evolution of the Universe, describing the Big Bang, cosmic expansion via the Friedmann equations [7], and the role of dark energy in accelerating this expansion. Across these scales, GR remains indispensable in interpreting observations and guiding our understanding of the fundamental nature of the Universe. Since its inception, GR has undergone rigorous experimental and observational testing and has consistently been validated across a wide range of scales, as mentioned above. The theory, therefore, is always regarded as a very robust theory of gravitation. However, despite its success, there are strong indications that the theory is incomplete

[8]. There are certain phenomena that GR alone cannot fully explain and, therefore, it faces many challenges, such as the singularity problem [9], incompatibility with quantum mechanics [10], unprecedented expansion of the Universe [7], and large velocities at galactic scales that go against stable structure formation for clusters and galaxies [11, 12, 13, 14]. These discrepancies typically have prompted the exploration of modification of the theory of gravity going beyond GR. It may be mentioned in this context that one of the motivations for considering modified theories of gravity, along with other issues, is the persistent observational evidence for dark matter (DM) and dark energy (DE), both of which remain invisible and undetectable by conventional means, yet are believed to constitute a significant portion of our Universe's mass-energy content. One of the most notable challenges comes from observing galactic rotation curves (RC). Standard gravitational intuitions prompt that the outer regions of galaxies, far from the central mass, should experience lower velocities in their rotation due to the lack of significant gravitational influence from the galactic core. However, observations reveal that objects, even in the outermost regions of galaxies, move at unexpectedly high speeds, leading to the hypothesis of a missing mass. The DM component can account for this discrepancy. In addition to the baryonic matter (composing 3% of the energy budget), DM is responsible for the flatness of the observed rotational velocity of the galaxies and large velocity dispersion (VD) in the clusters famously known as the missing mass problem [15, 16]. While GR can incorporate the effects of DM through its gravitational influence, the nature of DM itself remains elusive. This motivates alternative models, which can propose that gravity behaves differently at low accelerations, potentially negating the need for DM in explaining the observed rotation curves. On the cosmological front, GR in the ΛCDM framework provides a description that describes a homogeneous and isotropic nature of spacetime in an expanding Universe, famously known as the Friedmann-Lemaitre-Robertson-Walker (FLRW) Universe. However, ΛCDM, despite its success, suffers from the discrepancy between observation and simulation, such as core-cusp, missing satellite, and too-big-to-fail problems [17, 18, 19, 20, 21, 22, 23], to name a few. The accelerated expansion of the universe, observed through redshift measurements of distant supernovae and the cosmic microwave background, the Hubble tension are some of the issues where modified gravity theories gain attention [24, 25]. In the context of GR, the introduction of DE is necessary to explain the observed acceleration. However, alternative models of gravity, such as $f(R)$ theories or braneworld cosmology, suggest that the acceleration could be due to a modification in the gravitational laws at large scales [26], potentially offering a deeper understanding

of cosmic expansion without invoking the mysterious dark energy component.

The present thesis focuses on the galactic scales and explores the kinematics in different modified gravity scenarios. The galactic RC traces the radial kinematics of stars from the center to the outer radius [12, 13, 14]. On scales of galaxies, where velocities are typically much smaller than the speed of light (c), GR is well-approximated by Newtonian gravity, which predicts that the orbital velocity decreases with the square root of the radial distance from the center ($v \propto 1/\sqrt{r}$). Measurements of the net circular velocity within galaxies provide crucial information about the distribution of total mass present. Early studies revealed that the baryonic mass within the galaxy or cluster of galaxies [11, 12, 13, 14, 27] is insufficient for a hierarchical structure formation [28, 29, 30]. The alternative scenarios involve introducing a weakly interacting, invisible component, the DM, which is Occam's razor to the solution for the missing mass problem. Thus, in addition to the baryonic mass, DM contribution also affects the overall kinematics of the galaxy [31, 32, 33, 34]. Fritz Zwicky, in his observation of the Coma cluster, was the first to measure the anomalous large velocity within the cluster, hence coining the term "dunkle materie" (DM) [11]. A similar observation of the flatness of the circular velocity in the outer region of spiral galaxies was compiled by Vera Rubin in her famous 1980 article [35]. One of the DM profiles that has been extensively looked into is Navarro-Frenk-White (NFW), which is obtained from the N-body simulations of particles [36]. However, the NFW model predicts a cuspy profile at the central region of the galaxy. In contrast, the observations of low surface brightness galaxy suggest a core-like distribution, thus suffering from the core-cusp issue [37]. The other proposals to the DM profile include DC14 [38, 39, 40, 41], which, unlike NFW, incorporates the effects of baryonic feedback. Alternatively, the phenomenology of a cored DM profile, such as the Burkert profile, provides a promising fit to observational data [42, 43, 44].
As already mentioned at the beginning of this discussion, an alternative solution to these galactic kinematics issues involves modifying the Einstein-Hilbert (EH) action [26, 45], which governs spacetime dynamics in GR. This approach adds terms, such as scalar, vector, or tensor fields, to the Ricci scalar in the action. Few other exemplary modifications to GR include Kaluza-Klein theory [46, 47], Weyl's unified field theory [48], Einstein-Cartan theory [49, 50]. The modification proposals may also include theories allowing a varying nature of the gravitational coupling constant with space and time, such as Brans-Dicke theory [51, 52]. Similarly, theories such as higher derivative Gravity by Stelle demonstrate that the issue of non-renormalizability of GR can be evaded at the one-loop level when higher derivative terms are coupled to matter fields

[53]. Along a similar timeline, theories involving modification to the action of GR by replacing the Ricci scalar with a generalized $f(R)$ functional form also gained momentum [54, 55]. Another widely discussed extension to GR, the Gauss-Bonnet gravity [56], includes the higher-order curvature terms obeying the Lovelock theorem. The important point to note, in the context of our work on galactic kinematics, is that all the alternative gravity theories mentioned above share a common feature: the modified weak-field potential valid on galactic scales introduces an extra contribution to the Newtonian gravity potential, which may depend on specific free parameters fundamental to the model. The study of alternative theories of gravity has shown promising results in explaining various observations on galactic scales [26, 57, 58, 59, 60, 61]. In fact, these observations can also be used to constrain the alternative gravity models; for example, the observed mass distribution and gas dynamics of the galaxy clusters can provide insight into the behavior of the models on large scales and constrain the parameters for the alternative gravity theory [62, 63, 64, 65, 66]. Similarly, low surface brightness (LSB) galaxies are expected to be dominated by a large amount of DM. LSB galaxies are such that their surface brightness is significantly fainter than the background and have a central brightness of roughly $\mu_0 > 23$ mag/arcsec^2 [67]. Thus, understanding the modified kinematics for a gravity model on galactic scales is crucial to determine its validity [63, 68, 69, 70]. Beyond the galactic scales, the increased robustness of the recent observational data also helps us understand the alternative gravity model. This can even lead to the rejection of modified gravity models otherwise successful. For example, observations of GW put a stringent constraint on the graviton mass, thus rejecting theories predicting massive interacting particles [71, 72, 73]. The study of these modified gravity scenarios look into both the model building and the phenomenology aspects. Our work, in particular, focuses on the phenomenological aspects of such models in observable galactic systems. It may be stressed that modified gravity theories should not be presented as replacements for GR but rather as extensions or alternatives in specific contexts where the classical framework shows limitations. By exploring potential modifications to gravitational laws, one can aim to reconcile the observed discrepancies, whether by introducing new matter (DM), new forces (DE), or new principles of gravity itself. Thus, while GR remains an indispensable tool for understanding our Universe, the requirement for modified gravity theories reflects the limitations of GR in addressing certain cosmological, astrophysical, and galactic phenomena, urging the exploration of a more comprehensive theory of gravity that can account for all observed scenarios.

In particular, our work involves a few selected modified gravity models from the literature, such as modified Newtonian dynamics (MOND), $f(R)$ (with a couple of specific functional forms), Yukawa MOG (YMOG), and renormalization group correction to general relativity (RGGR). These gravity models depend on certain free parameters tested against the observations. For example, one of the gravity models viz. MOND [63, 74, 74], defined by an acceleration scale, is extensively studied in the literature. MOND successfully explains a wide range of observations [75, 76, 77]. The other model, generally termed the $f(R)$, replaces the Ricci scalar (R) in the action of gravity by a generalized $f(R)$ functional form. Depending on the choice of this generalized functional form, the parametrization may differ among different $f(R)$ models. This includes models such as Starobinsky [78], Hu-Sawicki [79], to name a few. However, the $f(R)$ models must obey certain stability criteria and be free from ghosts, which restrains the functional form of the $f(R)$ model [80]. We also probe the phenomenological gravity model incorporating the Yukawa-like correction to Newtonian gravity [81, 82, 83]. Such an expression is commonly found in the weak-field potential limit of many alternative gravity models and is modeled using coupling and scale parameters [82]. The literature also suggests the prospect of quantum gravity models such as renormalization group correction to general relativity [61, 84, 85, 86, 87, 88, 89], that studies the running of the coupling parameter with energy scale. The model focuses on the infrared behavior of the RG running to understand the kinematics on the astrophysical scales. However, the RG flow of G is expected to converge to a non-Gaussian fixed point, consistent with asymptotic safety, thus evading the issue of non-renormalizability of GR. General to all these models, for an alternative gravity model to be called fundamental, it must satisfy the observations at different scales of the Universe. Additionally, the precise nature of the experiments reveals that GR is validated on the solar system scales that restrict the alternative gravity models to regain a correct Newtonian limit. This motivates the implementation of screening mechanisms [90, 91, 92, 93] that are looked into for many gravity models to ensure their validity at the solar system scale. The mechanism is a theoretical construct that suppresses the effect of the modified gravity in high-density environments such as solar systems, thus regaining the correct GR limit.

As mentioned earlier, the work in this thesis focuses on the galactic regime where we tested the alternative gravity models to study the kinematics of ultra-diffuse galaxies (UDGs) and rota-

tionally supported galactic systems. UDGs are relatively small galaxies that are sub-categories of the Low Surface Brightness (LSB) galaxies, where the dynamics are measured using VD. Regarding the rotationally supported galaxies, we use the Spitzer Photometry and Accurate Rotation Curves (SPARC) data containing the mass models for a large collection of rotationally supported galaxies, along with the net RC and the individual baryonic component velocities. Both systems are used for testing the consistency of the alternative gravity models. The consistency of the gravity model is quantified using statistical tools such as goodness of fit and Bayesian Information Criteria (BIC). The two versatile regimes, i.e., UDGs and SPARC, to test the models provide us with a wide range to check the viability of the constrained parameters. In particular, to the rotationally supported galaxies, we further corroborate our claims towards the models by looking into certain empirical relations, viz. radial acceleration relation (RAR) [94] and baryonic Tully-Fisher relation (BTFR) [95] that are satisfied by the observational data from the SPARC. Additionally, to quantify our claim towards the favorability of alternative gravity models, we compare our results with a DM paradigm, where the NFW profile expresses the density of the halo. Hence, we divide the thesis discussion into two main parts. In the first part, we discuss the VD analysis of the UDGs for the alternative gravity models. In the latter part, we focus on the RC analysis of alternative gravity in the SPARC galaxies.

The kinematics of the UDGs are probed in the context of the specific choices of MOND, $f(R)$ model, and RGGR. In particular, we look into both DM-dominated and deficit UDGs. The DM-dominated DF44 [96] also looks into the impact of three anisotropy scenarios on the modified kinematics. The results clearly show that the three gravity models are consistent with observed VD kinematics. Among the different choices for the anisotropic parameters, isotropic motion is favored for all three gravity models. A comparison of the YMOG case with an NFW profile clearly shows that both MOND and *RGGR* behave equally well with the DM profile, whereas $f(R)$ is slightly disfavored. In contrast to DF44, the kinematics of DM-deficit galaxies such as DF2 [97], and DF4[98] are analyzed in the perspective of $f(R)$ and RGGR. As both these DM deficit galaxies are of similar sizes, we perform a global as well as local analysis for the alternative gravity models. We find that the gravity models can be accommodated to explain the current observations of both galaxies.

The second part of the thesis focuses on a detailed RC analysis of the SPARC galaxies for

RGGR and YMOG. We also verify the results by studying empirical relations RAR and BTFR. A comparison of the RGGR model with a DM profile shows that the gravity model behaves equally well with the observations. In contrast to local analysis, as in the case of RGGR, we look into a global study of the YMOG model. Our analysis shows that when the galaxies are grouped based on the morphological type, a global fit for the Yukawa model is consistent with the observed RC. We also verify the consistency of the global analysis with empirical relations such as RAR and BTFR. An additional check of the YMOG model includes a comparison with the observed normalized additional velocity (NAV)[99].

In this chapter, we introduce the necessary ingredients for the following thesis discussions in brief detail, for example, the galactic systems, the different gravity models, and the empirical relations. In the following Sec.1.1, we provide a brief discussion about the galactic systems that are looked into to study the behavior of alternative gravity models. Both UDGs and the SPARC galaxies are briefly described. In the Sec.1.2, we discuss the gravity models probed in the present thesis, i.e., MOND, YMOG, $f(R)$, and RGGR. Sec.1.3 briefly discusses the technique employed to constrain the model parameters of the gravity models. The final section Sec.1.4 discusses the outline of the present thesis.

1.1 Galactic kinematics

The subsection discusses the different galactic kinematics relevant for studying alternative gravity models. A key step in understanding the galactic kinematics is the classification of galaxies [100, 101]. In galactic scenarios involving frequent mergers over a time scale comparable to the Hubble time, systems may evolve into a spheroidal structure known as elliptical galaxies. The observed decline in the star formation activity for such galaxies suggests that the galactic systems are predominantly composed of old stellar systems. The second major class is spiral galaxies, where the gas collapses into a rotating disk. Compared to the elliptical galaxies, spiral systems contain more gas and dust and are thus observed to show new star formation. Most galaxies observed in the Universe contradict the strict dichotomy, i.e., they have a disk structure with a central bulge superimposed at the center and a diffuse gas. Depending on the presence of bulge structure and the spiral arms, the galaxies are classified based on the Hubble system.

Elliptical galaxies are subclassified from E0 (nearly spheroidal, ellipticity $e \equiv 0$) to E7 (highly elongated, $e \equiv 0.7$), where $e = 1 - b/a$ with a and b being the semi-major and semi-minor axes, respectively. The morphology additionally consists of the lenticular galaxies (S0), which occupy an intermediate position between the ellipticals and spirals. In the Hubble tuning fork diagram, spiral galaxies are classified based on the size of the central bulge and the tightness of the spiral arms. Type Sa spirals consist of galaxies having tight spiral arms and a prominent bulge. In types Sb and Sc, the bulge size gets smaller, and the spiral arms become progressively looser. Among the spiral types, there are galaxies having a bar-like structure in addition to the disk and bulge structure as mentioned above. Such galaxies, in addition to the specified notation incorporating the size of the bulge and spiral arms, are represented via SB.
The third category includes irregular galaxies, which, in contrast to elliptical and spiral galaxies, show a lot of evolution in brightness due to stellar activity, thus lacking coherent structure. Such systems appear chaotic with high SFR due to large gas content when compared to spiral and elliptical galaxies. They do not have a well-formed bulge and even contain a diffuse disk component. A more recently recognised class includes ultra-diffuse galaxies (UDGs). Such galaxies exhibit low surface brightness and large physical radius. UDGs are categorised as a subclass of the LSB galaxies and are predominantly composed of DM. However, the studies have observed a few UDGs that are completely devoid of DM. These galactic systems thus become an interesting place to test the consistency of alternative gravity models.

In the following section, we provide a detailed description of the galactic systems we probe to study modified gravity models, i.e., UDGs and rotationally supported systems. Additionally, the kinematics necessary to model the observed and stellar dynamics is also discussed for the two systems.

1.1.1 Ultra-diffuse galaxies and VD

The structure formation in a ΛCDM universe proposes the presence of a DM halo surrounding a galaxy to form a stable galactic system. Similar is the case with UDGs [97], whose structure is similar to that of dwarf spheroidal galaxies, which are diffuse, gas-poor systems with

low surface brightness ($\mu_V \sim 22-25$ mag arcsec^{-2}) and an older stellar population. UDGs are galaxies with low surface brightness dominated by globular clusters, and their galactic kinematics is probed using VD [102, 103, 104]. Such galaxies are known to be a subclass of low-surface brightness galaxies where the estimates for the effective galactic radius is much larger than the ones expected from systems having a median stellar mass of 6×10^7 M$_\odot$ [97]. The structure of UDGs resembles dwarf spheroidal with central brightness $\mu(g,0) \gtrsim 24$ mag arcsec^{-2} and effective radius $r_e \gtrsim 1.5$ kpc [97]. The dynamics of such systems having large-size yet diffuse galaxies are expected to be dominated by large amounts of DM. Thus, studying the modified kinematics of UDGs in an alternative gravity framework helps to check the consistency of the model. For the present thesis, we study the dynamics of three UDGs in the light of alternative gravity models. Among the three UDGs, two, i.e., NGC1052-DF2 and NGC1052-DF4, are found to have almost no DM content present within [98, 105], implying that the Newtonian kinematics can satisfactorily explain the observed VD. The kinematics for the third UDG, namely, NGC1052-DF44, is observed to be dominated by DM [96]. Such contrasting LSBs provide an insightful region to test and validate alternative gravity models [106, 107, 108, 109]; in our study, we have chosen the following models: MOND, $f(R)$, and RGGR.

For UDGs, the measurement of rotational motion is challenging due to their low surface brightness. Thus, the technique of VD is utilized to model the total mass distribution of baryonic matter within. Observationally, VD measures the broadening of the spectral line as objects move within the galaxy. Analytically, VD can be evaluated using the Jeans equation for a spherically symmetric mass distribution. Under the simplest assumption that the motion of the objects within the galaxy is isotropic, i.e., the radial and tangential motion is equal, the solution to the VD is provided by

$$\sigma^2(r) = \frac{1}{\rho(r)} \int_r^\infty \rho(r') a(r') dr'. \tag{1.1}$$

where $\rho(r)$ is the density profile for the UDG. For the case of UDGs, the baryonic distribution, hence, $\rho(r)$, can be approximated by a single density profile, namely, Sersic [110]. Also, $a(r)$ is the acceleration due to gravity. In the case of an alternative gravity model, the expression for the acceleration gets modified, having an additional term to the Newtonian potential. The modified acceleration and the mass modeling might include certain free parameters constrained

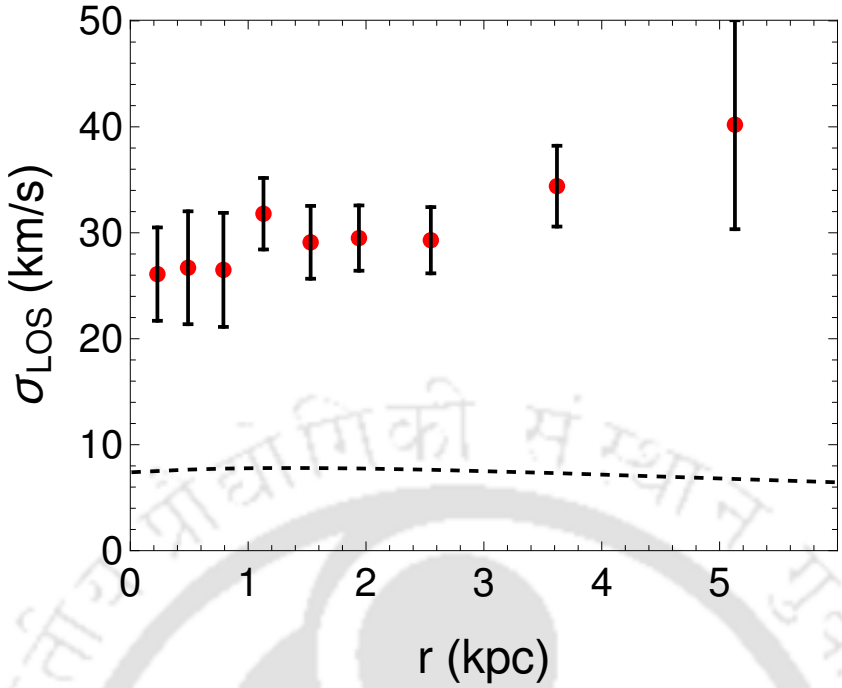

Figure 1.1: VD for the DF44 galaxy in Newtonian gravity. The red dots with error bars represent the observational VD data points for the DF44 galaxy [111]. The black dashed line corresponds to the analytical VD evaluated for an isotropic motion of the galaxy.

from the observations.

Among the three UDGs probed in the present thesis, the kinematics of DF44 is affected by the presence of a large amount of DM within. The baryonic contribution to the DF44 galaxy comes from the globular clusters. The DF44 is one of the largest UDGs observed within the Coma cluster. The radially measured VD for the galaxy is observed to be 41^{+8}_{-8} km/s ($r < 5.1$ kpc), which estimates a large mass-to-light ratio of 48^{+21}_{-14} $M_\odot/L_\odot$ [111]. The large value for the mass-to-light ratio suggests a discrepancy between the dynamical and luminous mass within the galaxy and infers the presence of DM. To model the baryonic component of the spheroidal DF44 galaxy, one assumes a Sersic profile, with the Sersic index $n = 0.94$ and $r_{\rm eff} = 4.7$ kpc [96]. The red dots with the error bar in Fig.1.1 show the observed data points corresponding to the DF44 galaxy. An analytical modeling using the projected VD component of Eq.1.1 where the acceleration a(r) is assumed to be Newtonian is shown via a black dashed line. The plot clearly shows a huge discrepancy between the observed and the measured VD in the Newtonian framework, where the contribution is only due to the baryonic mass present.

The kinematics for DF44 has been previously looked into concerning alternative gravity mod-

els, which suggests a possible explanation for the large observed VD without including the presence of DM [107, 109, 112, 113, 114]. For our analysis, we aim to test the viability of alternative gravity models to explain the kinematics of DF44. In this regard, we test three alternative gravity models, i.e., MOND, $f(R)$, and RGGR, to study the modified VD kinematics of the galaxy. To model the VD for DF44, we study three different assumptions for the anisotropy, which quantifies the direction of the motion of objects within the galaxy. If the velocity dispersion is similar in all directions, the motion is isotropic. Whereas if the stars within the galaxy move faster in the radial direction than in the tangential direction, the anisotropic motion is defined as radial and vice versa. Similarly, the choice for anisotropy can be position-dependent, such that it varies with the radial distance of the galaxy. For the present thesis, we analyze each gravity model for three specific choices of the anisotropy motion, i.e., isotropic, a constant, and a radially dependent Osikpov Merritt profile [115]. We additionally compare our analysis with a well-tested DM scenario where it is assumed that an NFW halo influences the kinematics of DF44.

Contrary to the dynamics of DF44, the UDG, namely NGC1052-DF2, showed almost no presence of DM in them [98, 105]. The net dynamical mass for the 10 globular clusters enclosed within the DM-deficit galaxy DF2 estimated using the mass estimator method (MTE) [116] is predicted to be $3.4 \times 10^8 \mathrm{M}_\odot$ (within the radius of 7.6 kpc) [117]. The baryonic mass estimated from the assumed Sersic profile is 2×10^8 $\mathrm{M}_\odot$ [105] and is almost similar to the dynamical mass. The observed ratio $M_{\mathrm{DM}}/M_{\mathrm{stellar}}$ is of $\mathscr{O}(1)$, which is almost 400 times lower than the values for the typical galaxies enclosed by DM halos [105]. The observed VD for the DF2 is less than 10.5km/s at 90% CL. The luminosity distribution is parameterized using the Sersic profile [100, 110] with Sersic index $n = 0.6$, axis ratio $b/a = 0.85$ and half-light radius as 2.2 kpc. Another UDG observed within the same group, NGC1052, i.e., NGC1052-DF4, shows a similar no DM nature [98]. The spectroscopy and imaging confirmed the presence of 7 globular cluster-like objects within. Similarly, for DF4, the luminosity is estimated by the Sersic profile with Sersic index $n = 0.79$, axis ratio $b/a = 0.89$, and major-axis half-light radius 1.6 kpc. Similar analysis for DF4 showed intrinsic VD measurement of about $4.2^{+4.4}_{-2.2}$ km/s. The ratio of $M_{\mathrm{DM}}/M_{\mathrm{stellar}}$ computed from the VD observation is again of the $\mathscr{O}(1)$, suggesting the existence of a second galaxy lacking DM [98]. The literature for both the UDGs explores many alternative gravity models to accommodate the VD kinematics for both the DM-deficit UDGs

[106, 107, 108, 109, 112, 118, 119]. In our analysis, we showed that the choice of two gravity models, viz., specific functional forms for $f(R)$ and RGGR, is consistent with the observed VD limit for both galaxies.

1.1.2 Rotationally supported galaxies and RC

The dominant contribution for a rotationally supported galaxy comes from the disk, which extends up to a few kiloparsecs (kpc) with a bulge superimposed at the center. In addition to the stellar part, the galaxy consists of diffused gas that extends throughout. The velocity distribution of each component (disk, bulge, and gas), along with the net observed velocity for 175 rotationally supported galaxies, is compiled within the SPARC catalog [120]. The measurements for the stellar components are done at near-infrared (3.6 μm), keeping the mass-to-light ratio (γ) for disk and bulge constant. Also, the diffuse atomic gas present within the galaxy is measured from the Doppler shift of 21 cm $HI/H\alpha$ line. The catalog contains the mass models of galaxies covering a broad range with varying luminosities, morphologies, rotation velocity, gas content, etc. [120]. The morphological type represents the position of the galaxy on the Hubble sequence [121]. The sequence incorporates a broad category of galaxies such as ellipticals, spirals, and late-type. The features of a galaxy, such as bars and bulges, are also significant in grouping the galaxy into different types. Depending upon the bulge size and structure of spiral arms, the SPARC is divided into 4 morphological types. It is also to be noted that the catalog does not include any galaxy with a barred structure. The different morphologies are represented via Hubble type (H), which for the catalog ranges between $H: 0-12$ [121]. The first Hubble category ranges with $H: 0-2$ belongs to the early type, which contains galaxies of type $S0$, Sa, and Sab, respectively. Such galaxies are distinguished by the presence of a prominent bulge at the center and tightly woven spiral arms. The second morphological type consists of spiral galaxies ($H: 3-6$), where features such as bulge and tightness of spiral arms start decreasing. The next two categories include late-type ($H: 7-9$) and starburst ($H: 10-12$). These types contain almost no visible bulge at the center of the galaxy. The last category, i.e., starburst galaxies, are known to have no spiral structure in the outer parts and are characterized by their diffused

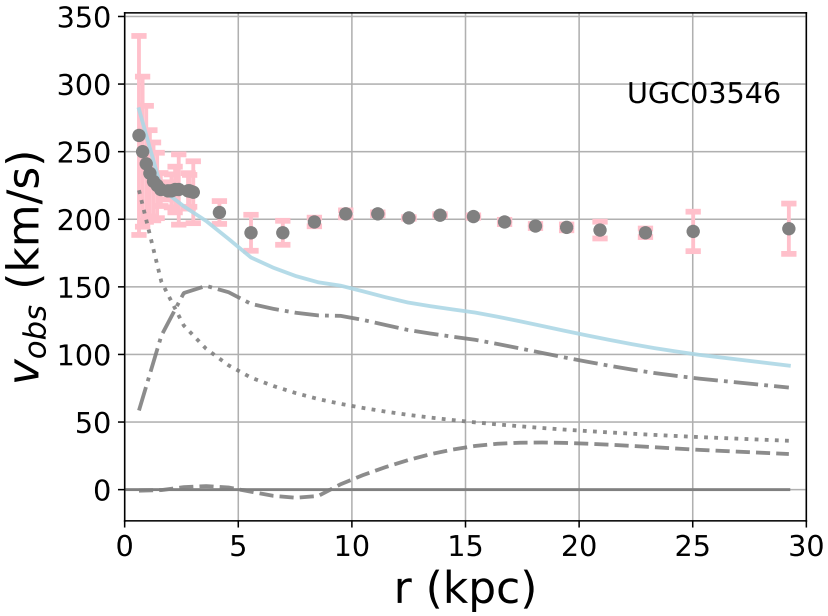

Figure 1.2: Rotation curve for UGC03546 galaxy. The gray dots with error bars in the plot are the radially varying observed circular velocity from SPARC [120]. The dotted, dotted-dashed, and dashed lines correspond to the baryonic components, i.e., disk, bulge, and gas, respectively. The net baryonic contribution evaluated using Eq.1.4 (γ_d, γ_b = 0.5) is represented by the blue solid line.

shape. The starburst galaxies are also known to have a higher star formation rate. It is to be noticed that as the range of Hubble number increases, there is an observed decline in the size of the central bulge, tightness of spiral arms, and resolution of distinctly visible arms decreases. Thus, this catalog represents a wide spectrum of galaxies and makes a versatile ground to test different alternative gravity models. The catalog has been extensively looked into for a variety of DM and alternative gravity models [122, 123, 124, 125, 126, 127, 128, 129, 130, 131, 132]. The objective of such analyses is to explain the discrepancy in the observed circular velocity and baryonic contribution by studying the RC of the galaxies. For the choice of DM models, the additional contribution comes from the choice of DM profile, which, in addition to baryonic matter, contributes to the overall kinematics of the galaxy. Alternatively, the kinematics in the weak-field limit for gravity models such as MOND, $f(R)$, and STVG, to name a few, are probed to explain the observational data. A comparison of the model with the data from the catalog helps to constrain the model parameters of the theory .

Rotation Curve: RC is the radial variation of the net circular velocity measured from the

center of the galaxy to the outer parts. RC measures the dynamical mass distribution within the galaxy. The missing mass problem on the galaxy scale suggests that the baryonic mass of the galaxy is insufficient when compared with the dynamical mass estimated from the observed circular velocity of a galaxy. For a rotationally supported galaxy, such as the Milky Way, the major components responsible for the baryonic mass include a disk, a bulge superimposed at the center, and diffused gas. The velocity estimate can be measured by knowing the density profile of each of the components. Thus, for a given density profile, by solving the Poisson equation, one can estimate the velocity contribution coming from a given component. Due to the linearity of the gravitational potential, the net baryonic contribution will be the sum of individual components. For a disk component, the generally assumed convention involves an exponentially varying radial profile [133]

$$\Sigma_d(r) = \Sigma_0 e^{-\frac{r}{r_d}}, \tag{1.2}$$

where Σ_0 is the central density of the disk and r_d is the disk scale length. Given the free parameters to model disk components (Σ_0, r_d), one can evaluate the velocity and potential contribution for a galaxy [133]. Similarly, the bulge component of a galaxy takes a spheroidal shape. Hence, the density profile can be approximated as a Hernquist profile [134],

$$\rho_b(r) = \frac{\rho_0}{\frac{r}{r_s}\left(1+\frac{r}{r_s}\right)^3} \tag{1.3}$$

where ρ_0 is the central density for the bulge, and r_s is the bulge scale length. For the given estimates of the bulge parameters (ρ_0, r_s), the solution from the Poisson equation for the density profile in Eq.1.3 evaluates the potential distribution for the bulge component. However, the gas present within a galaxy is diffused throughout. Thus, it becomes difficult to assume a universal profile for the gas component that can fit all the galaxies consistently. However, assuming an exponentially varying radial profile similar to Eq.1.2 is a good approximation to model the potential for the gas component. Thus, the baryonic modeling of a galaxy requires knowledge of the mass distribution of different galaxy components. Given the density of each component, one can estimate the net velocity of the baryonic component. Similarly, the net observed velocity of a galaxy can be traced using HI or $H\alpha$ emission lines from the objects present in the

galaxy. The $H\alpha$ emissions are detected in the inner regions of a galaxy and measure the velocity contribution due to ionized gas related to star formation. Alternatively, the HI extends beyond the visible disk and thus is crucial in determining the velocity in the outer regions where the effects of DM dominate. Thus, the Doppler shift of both lines (HI & $H\alpha$) traces the net circular velocity at different points within the galaxy.

The measurements in the SPARC catalog, in addition to the total observed circular velocity $v_{\rm obs}(r)$ with error bars $\sigma_{\rm err}(r)$, contains the radial variation of the velocity for individual baryonic components of a galaxy. The net Newtonian contribution arising from the stellar (disk, bulge) and gas components of a galaxy is defined as

$$v^2_{\rm bar}(r) = \gamma_{\rm d}\, v^2_{\rm disk}(r) + \gamma_{\rm b}\, v^2_{\rm bulge}(r) + |v_{\rm gas}(r)|\, v_{\rm gas}(r); \tag{1.4}$$

where $v_{\rm disk}(r)$, $v_{\rm bulge}(r)$ and $v_{\rm gas}(r)$ represent the disk, bulge, and gas velocity components for a particular galaxy in the SPARC catalog. Following the convention from the catalog, it may be noted that the two baryonic components (disk, bulge) are scaled by a factor $\gamma_{\rm d}$ and $\gamma_{\rm b}$, respectively, which measure the mass-to-light ratio for the disk and bulge part. The $\gamma's$ corresponding to each baryonic component quantifies the relation between the mass of the component and the luminosity. From the study of the stellar population model [135, 136] and from the minimum scatter of BTFR [137], the value of $\gamma_{\rm d} = 0.5$ is found to be optimal. For the present thesis, both the parameters ($\gamma_{\rm d}$, $\gamma_{\rm b}$) in Eq.1.4 are scaled independently for each galaxy and, hence, for our analysis, are referred to as the local parameters for a model. Each term in Eq.1.4 refers to the net potential contribution for a given component, which can also be negative, depending upon the effective influence from the mass within and outside of a given radius. Such a nature has been observed mostly at the inner radius of the gaseous component. The discrepancy of $v_{\rm obs}(r)$ with the baryonic contribution ($v_{\rm bar}$) can be witnessed clearly from the SPARC catalog. To provide an example, we have chosen a specific galaxy, UGC03546, from the catalog and plotted different baryonic velocity contributions to RC, following Eq.1.4 (fixing $\gamma_{\rm d}, \gamma_{\rm b} = 0.5$). We also plotted the total velocity due to Newtonian contribution using a blue solid line. The observed points with error bars are shown with gray dots. Fig.1.2 clearly shows the discrepancy of the $v_{\rm obs}(r)$ with the $v_{\rm bar}(r)$.

SPARC imposes certain selection criteria on the galaxies to be studied. This includes the re-

moval of galaxies with a Quality factor (Q) greater than 2, which suggests the data includes asymmetries and non-rotational motions. Additionally, we remove face-on galaxies with $i < 30^{\circ}$ from our analysis of alternative gravity models, as their orientation makes it challenging to derive accurate rotation curves. This leaves 153 out of 175 galaxies that can be looked into in the alternative gravity framework.

Under the assumption that gravity on the galactic scale is modified, the kinematics of objects within the galaxy have an additional contribution that depends on the choice of the model to explain the visible discrepancies between $v_{\rm obs}$ and $v_{\rm bar}$. To study the kinematics of SPARC galaxies, we look into two alternative gravity scenarios, namely RGGR and YMOG. The modified dynamics for a galaxy in the RGGR and YMOG framework, in addition to the baryonic part ($v_{\rm bar}$), contains a contribution constrained by free parameters that depend on the choice of the gravity model. Thus, comparing the observed velocity with the modified framework can check the consistency of the gravity model. Additionally, the free parameters of the chosen model are constrained using a Bayesian technique based on Monte Carlo Markov Chain (MCMC) algorithm. Using the best-fit parameters from the RC analysis, we also study the two empirical relations, viz RAR and BTFR, that hold true for the observational data from SPARC, as discussed in detail in the following section.

1.1.3 Empirical relations

Empirical relations such as RAR and BTFR are scaling relations that define laws governing galaxy evolution by relating the physical properties of the galaxy. These empirical relationships are universal as they correlate the observed quantities of the galaxy that are independent of any underlying gravity and DM models. Thus, the tightness of the modified RAR and BTFR for a certain gravity model with the fundamental relations helps to test the alternative theories.

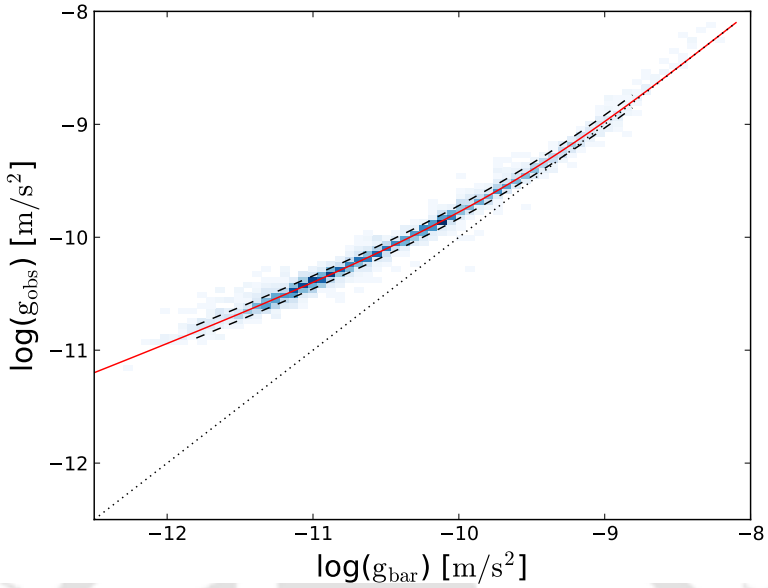

Figure 1.3: The observed RAR from SPARC observations taken from [138]. The red solid line is the mean RAR obtained using Eq.1.5. The individual data points from the observational data of 153 SPARC galaxies are represented by a blue-color scale. The black dashed line represents the root mean square scatter.

1.1.3.1 RAR

The analysis of SPARC data shows that the total baryonic acceleration $(a_{\rm bar}(r) = v^2_{\rm bar}(r)/r)$ cannot explain the net observed acceleration $(a_{\rm obs}(r) = v^2_{\rm obs}(r)/r))$ but follows a certain analytical relation known as RAR [94]. It is also regarded as a scaling law that is significant for probing galaxy dynamics as it provides a universal characteristic to the mass distribution in galaxies, independent of their Hubble type or size. This analysis is also true for the 153 galaxies of the catalog irrespective of their morphological types, thus indicating a new dynamical law governing galaxy kinematics. The empirical RAR obtained from SPARC is defined as [94]

$$a_{\rm obs}(r) = \frac{a_{\rm bar}(r)}{1 - \exp(-\sqrt{a_{\rm bar}(r)/a_*})}, \tag{1.5}$$

where a_* is the acceleration scale parameter and has best-fit value $a_* = 1.2 \times 10^{-10}$ ms^{-2}. For a rotationally supported galaxy, the net centripetal acceleration is defined in terms of the observed

velocity in the SPARC catalog

$$a_{\rm obs}(r) = \frac{v^2_{\rm obs}(r)}{r} = \left|\frac{\partial \phi_{\rm tot}(r)}{\partial r}\right|, \tag{1.6}$$

where $\phi_{\rm tot}$ is the total potential, i.e., total force per unit mass acting on a point particle. On the other hand, $a_{\rm bar}(R)$ is the linear sum of the acceleration for different baryonic components (disk, bulge, and gas) within the galaxy and can be estimated from the SPARC data using

$$a_{\rm bar}(r) = \frac{v^2_{\rm bar}(r)}{r} = \frac{\gamma_{\rm d}\, v^2_{\rm disk}(r) + \gamma_{\rm b}\, v^2_{\rm bulge}(r) + |v_{\rm gas}(r)|\, v_{\rm gas}(r)}{r} = \left|\frac{\partial \phi_{\rm bar}(r)}{\partial r}\right|. \tag{1.7}$$

Both the net circular velocity ($v_{\rm obs}(r)$) and individual baryonic components mentioned in Eq.1.6 and Eq.1.7 are known from the observations in SPARC. The plot in Fig.1.3 taken from [138] represents the observational RAR obtained from the SPARC data. The red line in the plot shows the analytical RAR derived using Eq.1.5. Additionally, the individual data points shown via a blue-color scale relating to the observed and baryonic acceleration are obtained from the SPARC. The plot shows that there indeed is a relation between the two observed quantities, i.e., baryonic and net acceleration compiled in the catalog. This makes the relation empirical as it assumes no prior knowledge about the DM or alternative gravity models and stems from the observational data in SPARC. The relation has been extensively studied in the context of alternative gravity models such as Scalar Tensor Vector Gravity (STVG), MOND, and Weyl gravity, to name a few [139, 140, 141, 142]. For our analysis of the RGGR and YMOG model, we aim to test and compare the behavior of the modified acceleration provided by the alternative gravity model.

1.1.3.2 BTFR

The second empirical relation, namely, the BTFR, shows a tight correlation between the dynamics of the galaxy and the baryonic distribution. BTFR suggests that the stellar mass of the galaxy has a power law dependence on the flat part of the circular velocity,

$$M_{\rm bar} = A V_{\rm f}^{x}. \tag{1.8}$$

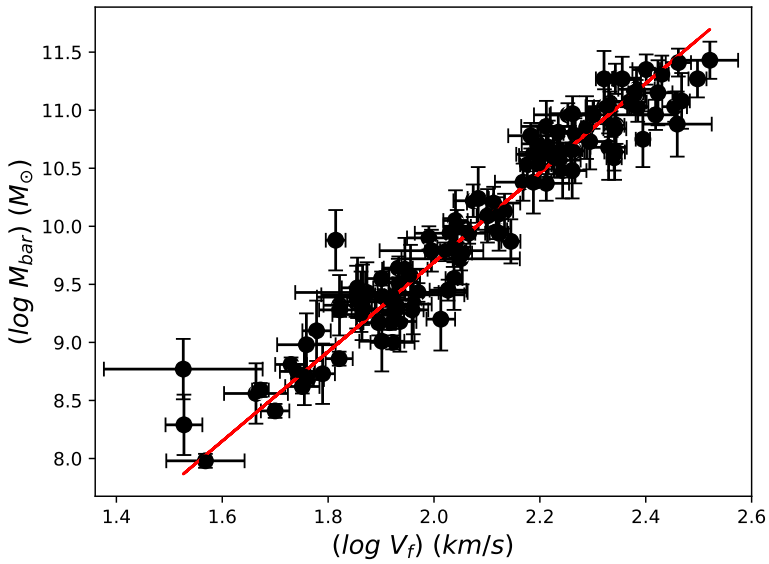

Figure 1.4: The observed BTFR relating the baryonic mass and flat velocity measured at 3.2 R_d. The black dots with error bars are the observed data points [120]. The red solid line is the best fit to the observation, which returns the slope of the line as 4, i.e., $M_{bar} \propto V_f^4$.

Here, M_{bar} refers to the baryonic mass (disk, bulge, and gas) contained within the galaxy, and $V_{\rm f}$ is the velocity measured along the flat part of the RC. BTFR is highly sensitive to the radius at which flat velocity is measured and various definitions for measuring the flat velocity are possible [143]. Thus, the observations compiled in SPARC help to accurately compile the baryonic mass (scaled by mass-to-light ratio) and the flat velocities corresponding to different measurement choices. The plot in Fig.1.4 relates the baryonic mass with the flat velocity (measured at $3.2R_d$) obtained from the catalog for a set of 153 SPARC galaxies. The black data points with error bars are the corresponding baryonic mass versus flat velocity at $3.2R_d$ in the log-log scale. The red solid line fits the observed data points using the BayesLineFit [143] package. The choice of 3.2 R_d ensures that for a pure exponential disk, 80% of the luminous contribution can be experienced at the radius. This also helps to evade the problem where the RC is observed to have a rising nature in the outer radius instead of the expected flatness. Thus, the optimal value of the free parameters (A, x) as obtained from the study of the SPARC catalog are estimated to be $A = 50$ $\mathrm{M_\odot km^{-4} s^4}$, $x = 4$ [95]. Similar to RAR, BTFR is also known to be empirical in nature as it assumes no underlying gravity model and is strictly obtained from the SPARC data. BTFR also acts as a cosmic distance indicator, as the luminosity emitted from a galaxy indicates its distance from the observer. Thus, BTFR is probed to constrain the Hubble constant

(H), concluding that $H < 70$ is rejected with 95% CL [144]. The relation is also studied to provide insights into the evolution and formation of the galaxies and test cosmological models [145, 146]. The tight relation between the observed baryonic mass and measured flat velocity helps to understand the galactic dynamics by probing the effects of the DM or gravity model in shaping the RC.

Analyzing the behavior of the alternative gravity models requires knowledge of $V_{\rm f}$ corresponding to the particular model. The modified velocities for the RGGR and YMOG frameworks depend on free parameters constrained by the RC fitting. Therefore, if alternative gravity models such as RGGR and YMOG explain the RC of galaxies, the $M_{\rm bar}$ versus model-dependent predicted velocity should also follow the observed BTFR. This additional check for the alternative gravity theories verifies the phenomenological consistency for both models.

1.2 Gravity Models

In this subsection, we focus on different alternative gravity models used in the present thesis, namely, MOND, $f(R)$, YMOG, and RGGR. Brief descriptions of the models, along with the existing constraints, are discussed. This is useful as in the later chapters, we study the validity of these gravity models against the observational data (UDGs & SPARC).

1.2.1 Modified Newtonian Dynamics (MOND)

MOND [74] proposes a modification to the Newtonian dynamics below an acceleration scale typically denoted as a_0. Whereas at acceleration significantly above a_0, Newtonian gravity is regained. Thus, at the small acceleration scales where the net acceleration (g) is much smaller than a_0, i.e., $g \ll a_0$, the modification takes the following form [63],

$$g = \sqrt{g_N a_0}, \tag{1.9}$$

here, g_N is the acceleration contribution from the baryonic components. For a test particle moving in circular motion around a massive object of mass M, the radial velocity component balances the centripetal acceleration and is thus defined as

$$\frac{v_c^2}{r} = \sqrt{\frac{GMa_0}{r^2}}, \tag{1.10}$$

where v_c is the net circular velocity. The weak-field velocity thus simplifies to

$$v_c^4 = a_0 GM. \tag{1.11}$$

The above equation shows that the velocity is independent of radius and asymptotically reaches a constant velocity that depends on the mass of the object. The equation is equivalent to the baryonic Tully-Fisher relation that suggests that the baryonic mass contained has a power law dependence with the flat velocity measured in the outer region of the galaxy. However, the standard Newtonian gravity is regained for regions where the acceleration is much greater than a_0 ($g \gg a_0$). The transition from one acceleration region to another is accounted for by introducing an interpolating function in the equation. Hence, the net modified acceleration a in the MOND framework is defined as [74]

$$\mu\left(\frac{a}{a_0}\right) a = a_{\rm N}, \tag{1.12}$$

where $\mu\left(\frac{a}{a_0}\right)$ defines an interpolating function such that for the regions where $a >> a_0$, we regain the correct Newtonian limit. The fundamental constant a_0 defines the transition between Newtonian and MOND gravity. In the above equation, The best-fit value to the global scale parameter obtained from the fit to the RC of spiral galaxies gives $a_0 = 1.14 \times 10^{-8}$ cm/s^2. For our analysis, we assume a standard form for the interpolating function, given by [74]

$$\mu(x) = \frac{x}{\sqrt{1+x^2}}. \tag{1.13}$$

Thus, for a scenario where the internal acceleration (a) within the galaxy is large such that the external effects can be neglected, the effective MOND contribution is [74]

$$a(r) = \frac{GM_{MOND}}{r^2} = \frac{a_N}{\sqrt{2}} \left(1 + \left(1 + \left(\frac{2a_0}{a_N} \right)^2 \right)^{1/2} \right)^{1/2}, \tag{1.14}$$

here a_N is the Newtonian acceleration ($\propto 1/r^2$) dependent only on the baryonic component of a galaxy. The study of MOND on galactic scales for both spiral [75, 76] and elliptical galaxies [147] shows a promising fit for the observations. The model is consistent with the empirical RAR obtained from the SPARC observations [94]. However, the model fails on relativistic scales for observations such as Gravitational Waves and lensing. Thus, relativistic MOND is making headway as it aims to extend the successes of standard MOND and reconcile them with high gravitational fields and large velocity regimes [148, 149].

Due to the fundamental nature of the MOND parameter, the model has been widely tested. It was successful to study mass discrepancy in tidal dwarf [150], RC [75, 76], wide binaries [151, 152], and many more. Contrary to the expectation, the VD dynamics of DM-deficit galaxies such as DF2 and DF4 are inconsistent with the standard MOND model [105, 118]. However, incorporating the effect of the host galaxy NGC1052 on the dynamics of the galaxy (EFE MOND) is studied to have a promising fit with the observational VD [77, 106]. Alternatively, for the DM-dominated DF44 galaxy, the EFE from the host Coma cluster fails to explain the large VD observations of the galaxy. In contrast, a standard MOND scenario fits the observational VD for DF44 well [113]. For our analysis, we focus on studying the kinematics of DF44 for the standard MOND scenario as an alternative to DM.

1.2.2 Yukawa Modified Gravity (YMOG)

One alternative gravity scenario tested for an extensive collection of rotationally supported galaxies is Yukawa MOG [82, 83]. The net gravitational potential (Φ) experienced by a test particle in this YMOG model is influenced by Newtonian ($\phi_{\rm N}$) and Yukawa-like ($\Phi_{\rm Yuk}$) potential that is scaled by a strength parameter β, i.e., $\Phi = \Phi_{\rm N} + \beta\ \Phi_{\rm Yuk}$. The effect of Yukawa

correction arises in the models where the force between particles is exchanged by massive scalar field m_ϕ. Thus, the Yukawa nature, whose effect is similar to the fifth force of scalar nature, can be tested on galactic scales. For the present gravity model, the combination of baryon and DM interaction influences the net contribution of potential. If α_b, α_{DM} is the coupling constant for baryons and DM, the effective potential experienced by a visible particle is thus the sum of baryon-baryon ($\alpha_{\rm b}^2$) and baryon-DM ($\alpha_{\rm b}\alpha_{\rm DM}$) effect. However, the local gravity experiments constrain the baryon-baryon interaction to be negligible, i.e., $\alpha_b^2 \ll 1$, implying that the fifth force is screened on the solar system scales; hence, a similar effect persists for all galactic systems [153]. Thus, the impact on RC from the fifth force is only due to the effect of DM. This leads to the standard Newtonian contribution from the baryonic and DM content with an additional effect from the scale-dependent Yukawa term that does not follow the Gauss theorem, defined as follows [154]

$$(\nabla^2 - \lambda^{-2})\Phi = 4\pi G\rho_{\rm DM}, \tag{1.15}$$

where ρ_{DM} is the density profile for the DM, G is the gravitational constant, and λ is the range of the fifth force, i.e., related to the mass of scalar field ($\propto 1/m_\phi$). As mentioned earlier, it is to be noted that the fifth force is coupled only to the DM content. The solution to Eq.1.15 returns the modified potential with the Yukawa-like correction, i.e.,

$$\Phi(r) = -G\int \frac{\rho(r')}{|r-r'|}(1+\beta e^{-\frac{(|r-r'|)}{\lambda}})d^3r', \tag{1.16}$$

here, $\rho(x)$ is the matter density, which includes the contribution from both baryonic (stellar, gas) and DM. Also, the coupling parameter β can be attractive or repulsive depending on the positive or negative signs that are allowed for the model. The model probed is not unique, and such a nature can also be found in the theories where a scalar, vector, or tensor field mediates the fifth force. Among the earlier works on the model, a Yukawa nature exists in the weak-field potential solution from the exchange of vector bosons. Such a model favors a repulsive coupling with the matter density, hence coined as "antigravity" [155]. Along the same lines, [154] shows that such a repulsive force is successful in creating flatness at the outer radius ($0.4\lambda < r < 2.5\lambda$) if the coupling parameter β exists within the range $(-0.95, -0.90)$. A similar repulsive nature is proposed for an STVG model where a fifth force exists due to an exchange of massive vec-

tor bosons [69, 156, 157]. The model successfully explains the cosmic microwave background radiation in a baryon-dominated universe and is also studied to explain the RC observations for high surface brightness (HSB) and low surface brightness (LSB) galaxies. It is to be noted that none of the models discussed yet include any contribution from DM. Furthermore, the solution to the $f(R)$ lagrangian using Parameter Post Newtonian formalism yields a Yukawa-like suppression [158]. A similar fourth-order gravity analysis includes a repulsive and attractive combination of Yukawa terms that successfully explains the RC only by including the DM component [159]. The Yukawa model is also looked into for a larger set of galaxies present in the HI nearby galaxy survey (THINGS) catalog [160]. The present thesis is influenced by the work done in [83, 161], where a mixed scenario incorporating the effect of DM and YMOG is looked into. In fact, analysis [161] with a group of LSB galaxies finds that a repulsive nature of the coupling parameter can satisfactorily explain the observational data. It is to be noted that the DM profile chosen here has a power-law dependence and is the only source for the baryonic mass distribution. On the contrary, a similar study for a random set of SPARC galaxies is shown to favor an attractive coupling nature of the fifth force [83].

In our analysis, we aim to look into the kinematics of SPARC galaxies to study the RC and constrain the Yukawa parameter in the YMOG framework. The objective of our phenomenological study is to look for the fundamental physics of the Yukawa parameters (β, λ) for a collection of galaxies. A random selection of 40 galaxies has shown a positive result towards the fundamental nature of the coupling parameter β [83]. To further verify the claim, we group the SPARC based on its morphological type and study if such nature persists for a larger subset of galaxies. For this, we compare the observed circular velocity for a subset of a particular morphological type in SPARC with the YMOG contribution written as

$$v_c^2(r) = v_{\rm bar}^2 + v_{\rm NFW}^2(r) + v_{\rm mog}^2(r), \tag{1.17}$$

where $v_{\rm bar}$ is the baryonic velocity contribution arising from the stellar (disk, bulge) and gas components of the galaxy as described by Eq.1.4. Also, $v_{\rm NFW}$ and $v_{\rm mog}$ are the velocity contributions from the DM and Yukawa contributions, respectively. For a choice of DM profile, the potential, hence velocity contribution, can be evaluated by substituting a choice of DM profile in Eq.1.15.

1.2.3 $f(R)$ gravity

$f(R)$ can be considered one of the most extensively studied alternative gravity models. Here, the Ricci scalar in Einstein-Hilbert action is replaced with a $R + f(R)$ or a generalized $f(R)$ functional form [54, 162]. The literature suggests many $f(R)$ models, which satisfy different observational regimes of the Universe [26]. These different choices for the functional form add to the complexity of the theory. The $f(R)$ gravity has been shown to explain the cosmic acceleration without invoking Dark energy (DE) [163, 164]. The model has also been looked into to study the kinematics of the galaxies, clusters of galaxies, and gravitational lensing [165, 166, 167, 168]. However, there can be models such as $f(R) \propto 1/R$, which consistently explains the acceleration of the Universe without the need for DE but suffers from instability, as discussed by Dolgov and Kawasaki [80], which limits the viable forms for the gravity model. The $f(R)$ has been tested at different observational astrophysical regimes to constrain the gravity model parameter. This includes the study of modified distances to Cepheid variables [169], redshift distortions [170], differences in stellar and gas RC of isolated dwarf galaxies [171], searching for fundamental parameters using screening mechanisms in SPARC [92], to name a few.

In what follows, we will briefly introduce the $f(R)$ gravity models. For a more detailed discussion and review, we refer the reader to [26, 70]. For the $f(R)$ model, the action of gravity becomes,

$$\mathscr{A} = \int d^4x\sqrt{-g}[f(R) + \mathscr{L}_{\rm m}] \tag{1.18}$$

Varying the action of gravity with respect to the metric $g_{\mu\nu}$ results in [26, 172]

$$G_{\mu\nu} = \frac{1}{f'(R)}\left\{\frac{1}{2}g_{\mu\nu}[f(R) - Rf'(R)] + f'(R)_{;\mu\nu} - g_{\mu\nu}\Box f'(R)\right\} + \frac{T^m_{\mu\nu}}{f'(R)} \tag{1.19}$$

where $G_{\mu\nu} = R_{\mu\nu} - (R/2)g_{\mu\nu}$ is the Einstein tensor. The prime convention used in the above equation denotes the derivative with respect to the Ricci scalar R. Depending on the choice of the functional form of $f(R)$, one can solve Eq.1.19 to evaluate the potential in the weak-field

limit valid on the galactic scales. Needless to say substituting $f(R) = R$ in Eq.1.19 returns the standard Einstein equation ($G_{\mu\nu} = 0$) in case of vacuum solution. Considering the stability criteria mentioned above, we look into two cases of $f(R)$. The first model assumes a generalized functional form which is Taylor expanded about a flat background ($R = 0$). Similarly, a specific form of $f(R)$ that is $\propto R^n$ is chosen and analyzed for the second model. Solving the equation of motion for the specific choices of $f(R)$ returns a solution with an additional term to the Newtonian potential dependent on free parameters that are constrained from the observations as discussed. Below, we briefly discuss two $f(R)$ models that were used in different choices of the thesis, and we denote them by model A and model B, respectively.

1.2.3.1 $f(R)$ gravity (model A)

Among the many choices for the functional form, we select a generic choice of $f(R)$ gravity model that assumes a Taylor expansion about the Minkowskian background ($R = 0$) [165, 173]

$$f(R) \simeq \sum_{i=0}^{\infty} \frac{f_i(0)}{i!} R^i, \tag{1.20}$$

where $f_i's$ are the coefficients associated with the i^{th} power of Ricci scalar in the expansion. The solution for the model is shown to result in a Yukawa-like correction in the weak-field limit for a general $f(R)$ form. The resultant solution valid for the galactic scales yields a modified potential given as [173]

$$\phi(r) = -\left(\frac{GM}{1+\delta}\right)\frac{1+\delta e^{-r/\lambda}}{r}. \tag{1.21}$$

In the above Eq.(1.21), the additional Yukawa-like term is characterized by δ and λ. Also, as can be seen from the equation above, for a point like baryonic mass M, the Newtonian part is scaled by a factor $\frac{1}{1+\delta}$. Here, δ is the coupling that determines the nature of the additional force and can be attractive or repulsive depending on the sign of the parameter. Following [174], we consider δ to be negative and within the range $-1 < \delta < 0$, implying the repulsive nature of the Yukawa force. Substituting $\delta = 0$ in Eq.(1.21) returns the GR case where potential varies as $1/r$. The parameter λ is the scale length and corresponds to the size of the system under analysis. Thus, λ is not a universal parameter. However, the $f(R)$ model that is looked into

still satisfies the consistency conditions to be a valid theory of gravity. This gravity model has been looked into different regions ranging from galactic cluster dynamics [168] to studying the VD of elliptical galaxies [175]. The analysis shows that the Yukawa model can potentially explain the kinematics on astrophysical scales without any need for DM. The phenomenological parameter δ obtained lies within the range $(-0.7, -0.9)$. The scale parameter λ is also found to be dependent on the size of the systems. The Yukawa-like form for the modified potential is similar to the phenomenological YMOG model discussed above. However, the YMOG model is considered in a mixed scenario where DM and YMOG contributions are incorporated.

For the study of UDGs, we assume the scenario where $f(R)$ explains the dynamics in the presence of only the baryonic matter with no need for DM. For this, we look into the kinematics of DM-deficit galaxies, assuming that the VD motion is isotropic. Similarly, the gravity model is also probed for the DF44 galaxy to check the consistency of the gravity model, which gives an alternative explanation for the DM-dominated galaxy. For our analysis, we aim to constrain the $f(R)$ parameters δ, λ for all three UDGs.

1.2.3.2 $f(R)$ gravity (model B)

The second choice for the $f(R)$ model that we have worked with replaces the Ricci scalar (R) in the E-H action by a power-law form given as $f_0 R^n$ [68]. Here, n is the slope of the Lagrangian for the action of gravity, such that $n = 1$ returns the standard GR case, and f_0 is a constant. Substituting the given functional form in Eq.1.19 and solving the equation of motion in the weak-field limit for the spherically symmetric system yields the potential,

$$\phi(r) = -\frac{GM}{2r}\left[1 + \left(\frac{r}{r_c}\right)^{\beta}\right], \tag{1.22}$$

G is the Newtonian gravitational constant, r_c is the scale radius determining where the deviations from Newtonian gravity become significant, and β controls the shape of the modified term and is related to the power law n as follows,

$$\beta = \frac{12n^2 - 7n - 1 - \sqrt{36n^4 + 12n^3 - 83n^2 + 50n + 1}}{6n^2 - 4n + 2}. \tag{1.23}$$

As β relates to the power (n) of the chosen action of gravity, which is expected to be universal, thus the model parameter (β) is treated as a global value. However, r_c is a scale that is dependent on the mass of the galaxy and, hence, varies with a system that is probed. Under the conditions that the gravity is Newtonian on the Solar system scales and the potential converges at large distances, β is constrained in the range $0 < \beta < 1$ [68]. The modified potential obtained for the R^n choice still shows an asymptotically decreasing behavior similar to the Newtonian model. However, it returns a higher contribution to the net circular velocity, which can explain the inconsistency in RC at a large radius.

A sample of 15 LSB galaxies with $HI/H\alpha$ observations of RC is studied to have a consistent fit with the observations where $\beta = 0.817$ ($n = 3.5$) and r_c being a local variable is constrained depending on the scale of the system [68, 176]. Similarly, the rotation curves of the spiral galaxies are reasonably explained for the above gravity model [177]. This model has also shown a promising fit with observations of Type Ia Supernovae and constraints on PPN parameters [178, 179, 180].

In the present thesis, we study the kinematics of the DM-deficit UDGs under the assumption that the net potential is modified as given by Eq.1.22. Our analysis constrains the model parameters and aims to show that the choice of gravity model is consistent with the observed VD data for DF2 and DF4.

1.2.4 Renormalization group correction to general relativity (RGGR)

One of the alternative formulations to modify gravity involves a quantum gravity extension, such as the Renormalization Group correction to general relativity (RGGR) [61, 86, 181, 182, 183, 184, 185, 186]. This approach suggests that the gravitational constant (G), traditionally considered a fundamental constant, exhibits energy dependence. This energy dependence, analogous to the running of couplings in quantum field theories, could resolve some inconsistencies when attempting to quantize gravity, such as the emergence of non-renormalizable infinities. However, such quantum corrections also give rise to a source of arbitrariness because of the dependence of the corrections on the scale parameter that needs to be correlated to the phys-

ical quantity. For instance, applying Appelquist and Carazzone theorem [86, 87, 187] within the framework of asymptotic safety for a four-dimensional quantum gravity model results in RG evolution for a higher derivative model [188, 189]. The common theme observed among the different approaches of the quantum gravity model is a logarithmic variation of the coupling parameter G. Following [89, 185, 190, 191], our approach studies a general covariant approach to quantum corrections, where the scale parameter depends on the potential energy of the astrophysical system. Previous studies with logarithmic variation in G along with the radial dependence of the scale parameter show a promising fit to the observed RC for both point-like [61, 184, 185] and extended [89, 190, 191] baryonic mass distributions.

The observations in the far infrared region established G as a constant [26]. However, this might not be true if one looks at GR as a field theory in curved spacetime. The beta function for the gravitational coupling constant G is chosen to have a logarithmic dependence on the energy scale (μ) of the Universe. From the dimensional argument, one unique choice for the beta function has been taken to be of the following form [89, 192]

$$\beta = \mu \frac{dG^{-1}}{d\mu} = 2\nu \frac{M^2_{\text{planck}}}{c\hbar} = 2\nu G_0^{-1}, \tag{1.24}$$

where ν is a phenomenological parameter fixed from observational data, and G_0 is the bare value of the gravitational coupling parameter. The logarithmic dependence of G with the energy scale as obtained from the solution of Eq.1.24 becomes

$$G(\mu) = \frac{G_0}{1 + \nu ln\frac{\mu^2}{\mu_0^2}}, \tag{1.25}$$

here μ_0 is the energy scale defined such that $G(\mu_0) = G_0$. As the variation in G is small, the exact value of μ_0 is inconsequential. For the far-infrared (IR) region, where the coupling parameter G is known as a constant, the GR limit is regained by substituting $\nu = 0$. Thus, the coupling parameter G in the Einstein-Hilbert action of gravity follows the RG flow given in Eq.1.25. For observations in galactic scales the variation in ν is of the order 10^{-7} [193]. A similar β function can also be defined for the cosmological constant ($\Lambda(\mu)$) present in the action of gravity. However, due to the negligible effect on the astrophysical scales, it is generally ignored

from the RC analysis of the galaxies [89].

To study the RGGR model on the scales of galaxies, it is required to relate the parameter μ with the energy scale of the system. For example, on the cosmological scales, μ is shown to relate to the energy scale of the Universe, i.e., Hubble constant (H) [60]. Similarly, for the galactic scales, μ has a functional dependence on the potential energy of the system. The choice relating the gravitational potential with the energy scale is such that we regain the correct Newtonian limit and satisfy the well-defined Tully-Fisher relation. The conditions constrain the relation to have the following form [60]

$$\frac{\mu}{\mu_0} = \left(\frac{\phi_{\rm N}}{\phi_0}\right)^{\alpha}, \tag{1.26}$$

where α is a mass-dependent phenomenological parameter constrained by the observations and ϕ_0 is the value of the Newtonian potential at the bare value of the coupling constant (G_0), hence a constant. Also, ϕ_N is the Newtonian potential corresponding to the baryonic mass of the galactic system. Therefore, we have two free parameters in the model, viz. ν and α. The two free parameters of the model, $\nu\alpha \equiv \bar{\nu}$ follow a close to linear relation with the baryonic mass of the galaxy for a selection of rotationally supported galaxies [190, 193]. For the given β-function of G and the choice of energy scale parameter, the solution for the circular velocity valid on galaxy scales is [89, 190]

$$v^2_{\rm RGGR}(r) = v^2_{\rm bar}(r)\left(1 - \frac{c^2\bar{\nu}}{\phi_{\rm N}(r)}\right), \tag{1.27}$$

where $v_{\rm bar}(r)$ is the Newtonian contribution to the velocity, c is the speed of light. The dependence of the phenomenological model parameters on mass or running of gravitational coupling parameters with defined energy scales suggests that the free parameter changes with the scale of the problem and, hence, is not universal. However, the phenomenological study of the RGGR model on elliptical and disk galaxies shows the best-fit value of $\bar{\nu}$ lies in the range of $10^{-6} - 10^{-8}$ and favors the observed dynamics of the galaxies that were looked into [190, 192]. In fact, a phenomenological study for a selection of galaxies [193] finds the $\bar{\nu}$ to have a nearly linear relation with the baryonic mass. Additionally, the constraints obtained on the solar system scales suggest the parameter $\bar{\nu}$ to be of the order of 10^{-17} [192]. The limit is much smaller than

the galaxy rotation curve estimates. This, however, is expected as the parameter $\bar{\nu}$ is found to have a linear dependence on the baryonic mass of the system. Compared to the spiral galaxies, the mass contained within the Solar system is about ten times less, thus making the value of $\bar{\nu}$ at solar system scales consistent. Similarly, in the case of Ultra-diffuse galaxies, whose masses are comparatively smaller than the rotationally supported galaxies, the evaluated $\bar{\nu}$ turns out to be 10^{-8} [194].

For our analysis, we look into the kinematics of UDGs and SPARC in the RGGR framework. We additionally constrain the model parameter $\bar{\nu}$ for the galactic system probed and study the claim of linearity of the free parameter with the baryonic mass. In our analysis, we aim to check the consistency of the gravity model with observational data from the galaxies.

DM profile: The consistency of the alternative gravity models with the observational data can be verified by comparing their phenomenology with an alternative perspective. For this, in most of the present work, a comparative analysis is performed using a choice of DM profile. For the purpose of this thesis, we have used the well-known NFW profile throughout different chapters whenever we compared our results from alternative gravity models with DM results [36, 195]. The NFW profile has the following form [36]

$$\rho_{DM}(r) = \frac{\rho_s}{r/r_s(1+r/r_s)^2} \tag{1.28}$$

where, ρ_s is the characteristic density and r_s is the scale radius. From the N-body simulation of the DM particle, the free parameters of the NFW model are found to have a relation such that the concentration parameter $c = r_{200}/r_s$ and virial mass $M_{200} = (4\pi/3)200\rho_{crit}r_{200}^3$. Thus, the free parameters of the NFW halo can be related to c and M_{200} as follows,

$$\rho_s = \frac{200}{3}\frac{c^3\rho_{crit}}{ln(1+c) - \frac{c}{1+c}}, \tag{1.29}$$

$$r_s = \frac{1}{c}\left(\frac{3M_{200}}{4\ \pi\ 200\rho_{crit}}\right)^{1/3}, \tag{1.30}$$

here, ρ_{crit} is the critical density having the magnitude 143.84 $M_\odot/kpc^3$. Also, to reduce the number of DM parameters, we use the $c - M_{200}$ relation, which is valid for galaxy-sized halos [83, 196]

$$c(M_{200}) = 10^{0.905} \left(\frac{M_{200}}{10^{12} h^{-1} M_\odot} \right)^{-0.101}, \tag{1.31}$$

here, h is 0.671 [197]. Using the relation in Eq.1.31, the contribution from the DM density profile can be seen to be dependent only on a single parameter, i.e., M_{200}. Thus, the choice of $c - M_{200}$ relation reduces the number of free parameters that must be constrained from the RC observations and is also a valid approximation for the galactic scale that is probed in the thesis. The velocity contribution for the DM-density provided in Eq.1.28 thus takes the following form,

$$v^2_{\rm NFW}(r) = \frac{4\pi G r_s^3 \rho_s}{r} \left[-\frac{r}{r+r_s} + \log\left(1 + \frac{r}{r_s}\right) \right]. \tag{1.32}$$

In the above equation the parameter ρ_s and r_s are related to a single parameter M_{200} via Eq.1.29, 1.30, and Eq.1.31, respectively. Thus, for our analysis, we require a single parameter M_{200} that needs to be constrained from the observations.

1.3 Methodology

The alternative gravity models discussed above rely on free parameters that need to be constrained using observational data. To achieve this, we employ computational methods grounded in Bayesian inference. In the present thesis, for most scenarios, we utilize the Monte Carlo Markov Chain (MCMC) algorithm to sample the posterior distributions of the model parameters. MCMC provides a powerful framework for exploring high-dimensional parameter spaces. MCMC generates a statistically representative array of parameter values by creating a Markov chain that asymptotically converges to the target posterior distribution. The sampler allows for a robust estimation of both the best-fit parameters and the credible intervals. The efficiency of the MCMC depends on the choice of the proposal distribution. The features of the MCMC algorithm include quantifying the parameter uncertainties, along with their degeneracies and cor-

relations. This proves to be crucial for distinguishing and comparing competing gravity models.

A general structure that defines an MCMC for a given observational data set $\mathscr{D}$ involves a product of the posterior probability $\mathscr{P}(\theta|\mathscr{D})$ and priors $\pi(\theta)$ for unknown set of parameters θ and is defined as

$$\mathscr{P}(\theta|\mathscr{D}) \propto \mathscr{L}(D|\theta)\pi(\theta), \tag{1.33}$$

where $\mathscr{L}(D|\theta)$ is the likelihood, which determines the probability of data for a given model with free parameters, and $\pi(\theta)$ represents the priors imposed on the free parameters. Assuming that the errors on the observed circular velocity follow a Gaussian distribution, the likelihood for each galaxy is written as

$$\mathscr{L}_g = (2\pi)^{-n/2}\left\{\prod_{i=1}^{n}\sigma(r_i)^{-1}\right\} \times \exp\left\{-\frac{1}{2}\sum_{i=1}^{n}\left(\frac{v_{g,\mathrm{obs}}(r_i) - v_{\mathrm{tot}}(r_i,\vec{\theta})}{\sigma(r_i)}\right)^2\right\},$$

here, n represents the number of observational data points over which the likelihood is summed. Also, $v_{obs}(r)$ and $\sigma_{err}(r)$ are the observational datapoint defined at a given radius and the corresponding uncertainties. The analytical velocity $v_{tot}(r,\vec{\theta})$ computed at a certain radius for a given set of free parameters is model-dependent. The net circular velocities or velocity dispersion in the case of UDGs for an alternative gravity scenario are expressed in terms of their respective free parameters. These free parameters in velocity $v_{\mathrm{tot}}(r,\vec{\theta})$ are phenomenologically constrained by comparing with the observational circular velocity. As an example, for the DM model discussed in the 1.2.4 of Sec.1.2, the NFW choice includes a single parameter M_{200} that needs to be constrained.

Regarding the choice of priors $\pi(\vec{\theta})$, different assumptions can be employed depending on the knowledge of the model parameters. In the present thesis, we consider two types of priors for the parameter estimation i.e., flat and Gaussian priors. This allows us to test the sensitivity of the parameter constraints to prior assumption. In context of the SPARC dataset (as discussed in 1.1.2), the parameters such as mass-to-light ratio for both disk (γ_{d}) and bulge (γ_{b}) are assumed to have no radial dependence on the galaxy. These parameters are treated as free variable and

are constrained using MCMC sampling. Thus, in case of flat priors, the parameters are varied in the range [0.3, 0.8] [83, 198, 199]. For the Gaussian priors, the parameters γ_d and γ_b are considered to have a mean value of 0.5 and a standard deviation of 0.1. To ensure the convergence of the Markov chain, we run the sampler for a sufficient number of steps such that the acceptance fraction lies within the range $0.2-0.5$ [200]. Additionally, by estimating the autocorrelation time (τ) for each galaxy, we discard τ number of steps as burn-in before performing posterior analysis. To achieve convergence, we run a sufficient number of steps, i.e., 50 τ as specified in *emcee* [200].

Additionally, to quantify the preference of one model over the other, we consider the Bayesian Information Criteria (BIC), which approximates the Baye's factor and penalizes models with a greater number of free parameters. BIC is defined as [201]

$$BIC = -2\log\mathscr{L}_{max}(D|\vec{\theta}) + 2k\log(n). \tag{1.34}$$

Here, k is the number of parameters for a given model. Also, n represents the number of data points in each galaxy. To compare the two models, say, model I and II, we evaluate,

$$\Delta BIC = BIC_{II} - BIC_{I}. \tag{1.35}$$

The measure of ΔBIC, if less than 2, implies inconclusive preference between the two models. Similarly, the value of ΔBIC that is between $2-6$ implies a positive inclination towards I. Values of ΔBIC greater than 6 are considered to have a strong inclination toward the I model.

1.4 Outline of the thesis

The thesis is organized into two parts: studying the kinematics of the UDGs and the rotationally supported galaxies.

The first part of the thesis focuses on the kinematics of LSB galaxies. For this, we look into the VD kinematics for two kinds of UDGs, i.e., DM dominated (DF44) and DM deficit (DF2

and DF4). In Chapter 2, we aim to study the kinematics of the DF44 galaxy for three different choices for the alternative gravity models: MOND [63], $f(R)$ [175], and RGGR [190]. DF44 is observed to have almost 98% of the total dynamical mass as DM [96]. To model the VD for an alternative gravity model, we additionally consider the effect of anisotropy on the overall kinematics of the galaxy. For this, we consider three different choices for the anisotropic motion, i.e., isotropic, a constant anisotropy, and a radial profile given by Osikpov- Merritt [202]. We additionally constrain the free parameters for the mass modeling and the choice of gravity model using the emcee package [200]. The emcee package is a sampler that is utilized for the Bayesian parameter estimation. For all three gravity models, we observe that the choice of radial profile is the least preferred among the three. We additionally evaluate the preference between the choice of isotropic and constant anisotropy, which suggests that the result is inconclusive, favoring both models. For the constant anisotropy case, we allow the priors, including both the radial and tangential profiles. In the case of DF44, for all three gravity models, statistics prefer a tangential choice. As the constant anisotropic case is consistent for all the models, we compare it with an alternative DM scenario assuming an NFW profile.

In Chapter 3, we discuss the consistency of the alternative gravity models to explain the observed VD of the DM-deficit galaxies, NGC1052-DF2 and NGC1052-DF4. The two UDGs, namely, NGC1052-DF2 [105] and NGC1052-DF4 [98], are observed to have smaller VD. The measured VD for DF2 is 10.5 km/s at 90% CL, which is comparable with the Newtonian kinematics. The net dynamics of these UDGs are well explained solely by the baryonic matter present within. Hence, they are mentioned as the DM-deficit UDGs. In our analysis, we look into the consistency of two alternative gravity models, i.e., $f(R)$ and RGGR, with the observational VD for both the DM-deficit UDGs. The free parameters of the models are constrained statistically by comparing the VD kinematics in a modified framework with the observational data of both galaxies independently. The modified VD kinematics for both UDGs are studied, assuming the simplest case where the motion is isotropic. Alternatively, as both UDGs have similar characteristics, the model parameters, such as the coupling parameter in generic $f(R)$, n for the power law choice, or mass-dependent parameter for the RGGR, are be constrained globally. Our findings show that when the UDGs are analyzed independently, the gravity models, i.e., $f(R)$ (both generic and power-law) and RGGR, are consistent with the observations. Similarly, for the case where we study both UDGs globally, the model parameters are found to

be similar to the local case and are consistent with the observational VD.

The second part looks into the kinematics of rotationally supported galaxies for two choices of alternative gravity models. The first gravity model probed in Chapter 4 is RGGR, studied independently for the 153 qualifying SPARC galaxies. The RGGR model [89, 190] looks into the energy scale variation of the gravitational coupling parameter G. The weak-field potential valid on a galactic scale introduces an additional term to the Newtonian potential dependent on the potential energy and a mass-dependent free parameter. The free parameters of the model are constrained independently for each galaxy using the Bayesian method, i.e., emcee [203]. We additionally compare the RGGR model with an alternative NFW scenario. The RGGR model turns out to be consistent with the observational RC data and is a competitive choice for a gravity model in comparison to NFW. We additionally justify the linear variation of the phenomenological model parameter with the baryonic mass of the galaxy. Thus, as we go from early-type galaxies to starburst, we see a decline in the magnitude of the free parameter, i.e., early-type galaxies showing a larger value than the starburst. In our analysis, we also look into the two empirical relations satisfied by the SPARC galaxies, namely RAR and BTFR. Our analysis for the eligible SPARC galaxies showed that both relations behave satisfactorily in the RGGR framework.

The second model chosen for studying the SPARC galaxies, as discussed in Chapter 5, is YMOG. Yukawa-like term is dependent on the coupling and scale parameter of the Newtonian potential, and this fifth force interacts only with the DM component. For the DM profile, we assume the well-studied NFW profile and constrain the model parameters of the fifth force morphologically for different kinds of galaxies in the SPARC. The parameters belonging to the baryonic and DM components are constrained locally for each galaxy. We find that the YMOG is consistent with the observational RC when galaxies are grouped and studied based on their morphology. We notice that for the spiral and the late-type galaxies, the coupling parameter is much smaller in magnitude when compared to the early types. Furthermore, we also check the consistency with the RAR and BTFR. We additionally verify the consistency by comparing it with the observational normalized additional velocity (NAV) [99]. We find that YMOG is consistent with the observations only if the global parameters vary with the morphology of the galaxy. Finally, we compile the summary of our work in Chapter 6.

Chapter 2

Velocity dispersion of DM dominant ultra-diffuse galaxies

2.1 Introduction

The ultra-diffuse galaxies (UDGs) are galactic systems having low surface brightness that, in many cases, host excess globular clusters relative to normal dwarf galaxies [102, 104, 204]. This type of galaxy shows both extremes of DM content: some may consist entirely of DM, while others appear to be almost free of DM. The formation history of UDGs still remains an open debate, with proposals calling them failed galaxies that were unsuccessful in achieving the stellar population due to tidal stripping [205], AGN feedback [206, 207], gas stripping [208], galaxy harassment [209], etc. The globular clusters within the UDGs suggest the presence of DM halo, implying that the net kinematics is inconsistent with the velocity dispersion (VD) contribution solely from the baryonic components (except for galaxies which are having extremely low or no DM content, such as NGC1052-DF2 & NGC1052-DF4). One of the largest UDGs observed within the Coma cluster, NGC1052-DF44 (henceforth DF44), having 94^{+25}_{-20} globular clusters,

suggests that 98% of the mass of the galaxy is composed of DM [96]. The mass-to-light ratio of $48^{+21}_{-14}\, M_\odot/L_\odot$ measured within the half-light radius suggests that the total mass present within DF44 ($\sim 10^{12}\, M_\odot$) is comparative to the Milky Way galaxy [96]. The phenomenological study of the DF44 galaxy in the context of the DM model can successfully explain its kinematics. More precisely, the study with a generalized Navarro Frenk White (g-NFW) [210] and DiCintio [38] density profile can explain the kinematics of DF44 satisfactorily [211]. Nevertheless, the kinematics of DF44 is also found to be consistent when probed in the context of alternative gravity models [107, 109, 112, 212].

In this chapter, our analysis aims to look into the consistency of a few selected alternative gravity models in explaining the radial VD measurement. The background literature on DF44 shows that gravity models such as standard MOND, Weyl conformal gravity, and Scalar-Tensor-Vector gravity (STVG) fit the observations well [112, 113]. The analysis in the context of standard MOND, with the UDG mass solely responsible for dynamics, reveals excellent fits, in line with the existing literature [112]. Alternatively, the external field effect (EFE) of the Coma cluster where the galaxy DF44 is embedded may impact the kinematics of the galaxy in the case of MOND. However, [212] showed that incorporating the EFE of the Coma cluster fails to explain the observed kinematics of the galaxy. A similar conclusion was derived for 10 other UDGs within the cluster. The proposal to resolve the inconsistency of EFE with DF44 includes a screening mechanism, higher mass-to-light ratio, inconsistency in the distance measurement, tidal disruption, etc. [212]. Among different scenarios, it was shown that an out-of-equilibrium radial infall of DF44 in the Coma cluster may give rise to an observed higher VD or a suppressed EFE for the UDG [114]. Similarly, gravity models, such as Degenerate Higher-Order Scalar Tensor (DHOST) [107] and non-local gravity [109], are also looked into to explain the kinematics of DF44. It is to be noted that the majority of the analysis on UDG kinematics is in the context of the radial evolution of the VD following the isotropic model. In our analysis, we focus on the impact of deviation from this conventional VD evolution by introducing anisotropic evolution. This anisotropy aspect of the problem becomes important for statistical testing of the alternative gravity models. In this regard, we consider MOND [63, 74, 112] as our reference while comparing alternative gravity models. We analyze three different choices for the anisotropy parameter (viz. radial anisotropy, tangential anisotropy, and zero anisotropy) to explain the observed DF44 VD. We find that a tangential anisotropic motion of the objects

is preferred for DF44. Among the three scenarios, the radial anisotropic choice is the least preferred and is quantified using Bayesian Information Criteria (BIC).

Corresponding to MOND, the acceleration scale parameter is constrained from the prior observations [213, 214]. Hence, the study only includes mass modeling parameters to be fitted. Based on the technique applied for the phenomenology of standard isolated MOND study, we look into two distinctive alternative gravity models. One model assumes a generic functional form $f(R)$ in contrast to the Ricci scalar (R) in the EH action of gravity. Rather than defining a particular form, this model assumes a general expansion of R about a flat background [26, 215]. The choice of the particular $f(R)$ model involves constraining two model parameters, which include coupling and scale radius. On the contrary, the other model is the RGGR [89, 190] that studies the energy scale dependence of the coupling parameter of the theory. On the astrophysical scales, the major contribution to the kinematics arises from the variation of the gravitational coupling parameter. The solution to the potential valid on the galactic scale is dependent on the potential energy of the system and a mass-dependent free parameter.

This chapter is organized as follows. Section 2.2 discusses the analytical method to study the kinematics of UDG and mass distribution of NGC1052-DF44. The section 2.3 discusses the three alternative gravity models we look into to explain the dynamics of DF44. The methodology employed to constrain the model parameter is discussed in Section 2.4. Lastly, we discuss the results obtained and the conclusion of our study in Section 2.5 and 2.6, respectively.

2.2 VD : Formalism

The velocity dispersion (σ) is a measure of the net galactic kinematics [216]. Observationally, VD is measured from the broadened spectral lines as objects move within the galaxy. The radial evolution of the VD is modeled using the Jeans equation for a spherically symmetric mass distribution [100],

$$\frac{1}{\rho(r)}\frac{\partial(\rho(r)\sigma^2(r))}{\partial r}+\frac{\xi(r)}{r}\,\sigma^2(r)=\frac{\partial\phi(r)}{\partial r} \tag{2.1}$$

where $\rho(r)$ is the mass density distribution, $\phi(r)$ is the gravitational potential of the galaxy. The deviation from radial isotropy is measured in terms of the anisotropy parameter $\xi(r)$, defined as

$$\xi(r) = 1 - \frac{\sigma_\theta^2(r)}{\sigma_r^2(r)}. \tag{2.2}$$

Here, $\sigma_r(r)$ and $\sigma_\theta(r)$ are the radial and tangential components of the VD. Depending on the sign of $\xi(r)$, the motion of the object within the galaxy can be either radially ($\xi \geq 0$) or tangentially ($\xi \leq 0$) dominated. However, for an isotropic motion of objects in the galaxy, the radial and tangential components are equal, i.e., $\xi = 0$.

The right-hand side of the Jeans equation involving the gravitational potential of the galaxy $\phi(r)$ can be estimated in the context of Newtonian gravity and for the choice of spherically symmetric mass distribution $\rho(r)$,

$$\frac{\partial \phi(r)}{\partial r} = \frac{GM_N(r)}{r^2} = \frac{G}{r^2}\int_0^r 4\pi\rho(r')r'^2 dr'$$

where G is the Newton's gravitational constant and M_N is the mass within the radius r. Thus, for a choice of $\xi(r)$, solving Eq.2.1, one can obtain $\sigma(r)$ given the $\rho(r)$ for the galaxy. However, the astrophysical observations do not measure the VD but rather the projection of the radial component of the VD on the line of sight (σ_{LOS}). The σ_{LOS} from a 2-D projected distance r to the point of observation is expressed as [217]

$$\sigma_{LOS}^2(r) = \frac{2}{I(r)}\left(\int_r^\infty dr\, \frac{r\,\rho(r)\,\sigma^2(r)}{\sqrt{r^2-r^2}} - r^2\int_r^\infty dr\,\xi(r)\frac{\rho(r)\sigma^2(r)}{r\sqrt{r^2-r^2}}\right),$$

where $I(R)$ is the surface density of the galaxy probed. The computation of Eq.(2.3) for a given gravity model has a large time complexity. Therefore, to improve the computing time, a reduced analytical form for LOS VD, numerically equivalent to Eq.2.3 is used [115]

$$\sigma_{LOS}^2(r) = \frac{2G}{I(r)}\int_r^\infty dr\, \mathscr{K}\left(\frac{r}{r}, \frac{r_a}{r}\right)\, j(r)\frac{M(r)}{r} \tag{2.3}$$

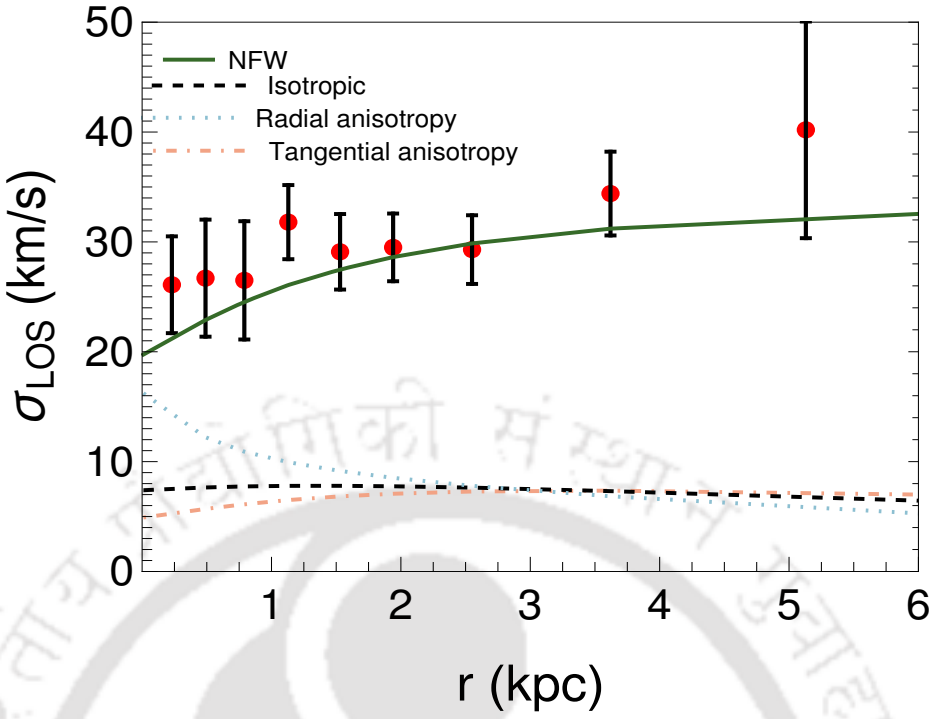

Figure 2.1: The VD for DF44 when the underlying gravity is Newtonian or with an NFW DM halo. The red dots with error bars are the VD data and the effective errors on the observations as defined in [111] for the DF44 galaxy. The plot represents the Newtonian kinematics of the DF44 galaxy for three different choices of the anisotropic profile. The black dashed, blue dotted, and orange dotted-dashed line highlights the $\xi = 0$ (isotropic), $\xi = 0.6$ (radial), and $\xi = -0.6$ (tangential) scenarios, respectively. In addition, the plot also shows the case for a DM profile represented by a solid green line, which shows a consistent fit for the observational data. The density profile for the DM halo is NFW with $M_{200} = 0.70 \times 10^{11}\ M_{\odot}$.

where $\mathscr{K}$ is a kernel function, $j(r)$ is the projected luminosity density and $M(r)$ is the dynamical mass contained within the galaxy. For the case of GR without DM, the mass function is a standard Newtonian mass M_N. Similarly, for the alternative gravity models, a mass function can be determined from the additional components added to the Newtonian potential.

In the case of alternative gravity models, the potential, in addition to Newtonian contribution, will have an extra component depending on the choice of the gravity model. These components, in total, will result in the net dynamics of the galaxy. In this paper, we aim to study the kinematics of DM-dominated DF44 in the context of different gravity models. This requires modeling the distribution of the baryonic content of the galaxy.

Mass model for DF44:

The baryonic contribution for the DF44 galaxy comes from the globular clusters present within. Under the assumption that the structure of the galaxy is spheroidal, the surface brightness can be modeled using the Sersic profile [96] defined as

$$I(r) = I_0 \exp\left[-\beta\left(\frac{r}{r_{eff}}\right)^{1/n}\right]. \tag{2.4}$$

Here I_0 is the central surface density, n is the Sersic index, and β determines the shape of the Sersic profile, which is related to n via $\beta \sim 2n - 0.33 + 4/405n + 46/25515n^2 + \mathscr{O}(n^{-3})$ [119, 218]. The mass modelling estimates for DF44 gives the Sersic parameter $n = 0.94$ and $r_{eff} = 4.7$kpc [96]. Also, the total luminosity of the stellar mass contained within the fiducial distance of 100 Mpc of DF44 comes out to be $L_{\rm tot} = 2.33 \times 10^8 L_\odot$. Given $L_{\rm tot}$, the central surface brightness I_0 in the Sersic profile is calculated from the integrated total luminosity profile, i.e., $2\pi \int_0^\infty r\, I(r)\, dr = L_{\rm tot}$.

However, the measured deprojected luminosity density $j(r)$, obtained from the Sersic profile is given as [219, 220]

$$j(r) = j_0 \left(\frac{r}{a_s}\right)^{-p_n} \exp\left(-\frac{r}{a_s}\right)^{1/n}, \tag{2.5}$$

where $a_s = \frac{r_{eff}}{\beta^n}$, $p_n \simeq 1 - \frac{0.6097}{n} + \frac{0.05463}{n^2}$ [219] and $l_0 = \frac{L_{\rm tot}}{4\pi n \Gamma[(3-p_n)n] a_s^3}$. The mass density ($\rho(r)$) in the context of $M(r)$ is obtained by scaling the projected luminosity density with the constant mass-to-light ratio (γ_*) of the stellar system, i.e.,

$$\rho(r) = \gamma_* j(r). \tag{2.6}$$

For our statistical analysis, γ_* is treated as a free parameter having no radial dependence.

Finally, the kernel function in Eq.(2.3) depends on the nature of the anisotropy parameter. We study the galactic kinematics for three criteria: $\xi = 0$, ξ constant other than zero, and a radially dependent ξ. Regarding the radially dependent anisotropy profile, we consider the Osikpov-

Merritt model $\xi(r) = \frac{r^2}{r^2+r_a^2}$ [202, 221], where r_a defines the scale radius of the anisotropy profile. In this case, the kernel function is expressed as [202],

$$\mathscr{K}(u,u_a) = \frac{u_a^2+1/2}{(u_a^2+1)^{3/2}}\left(\frac{u^2+u_a^2}{u}\right)\tan^{-1}\sqrt{\frac{u^2-1}{u_a^2+1}} - \frac{1/2}{u_a^2+1}\sqrt{1-\frac{1}{u^2}} \tag{2.7}$$

where $u = r/r$ and $u_a = r_a/r$ as defined in Eq.2.3. The simplest assumption is the isotropic motion of the objects in the galaxy, i.e., $\xi = 0$. We also treat ξ as a free parameter that ranges for positive (radial) and negative (tangential) anisotropy.

For the case where ξ is treated as a constant, the kernel function $\mathscr{K}$ in Eq.(2.3) is written as [202]

$$\mathscr{K}(u) = \frac{1}{2}\,u^{2\xi-1}\left[\sqrt{\pi}\frac{\Gamma(\xi-1/2)}{\Gamma(\xi)} + \xi\mathscr{B}\left(\frac{1}{u^2},\xi+1/2,1/2\right) - \xi\mathscr{B}\left(\frac{1}{u^2},\xi-1/2,1/2\right)\right], \tag{2.8}$$

here $\mathscr{B}(x,a,b)$ is the incomplete Beta function.

Now, we assume the scenario where the dynamics of DF44 can be explained using Newtonian gravity. The LOS VD in such a framework for different anisotropy models is shown in Fig 2.1. The black dashed line in the plot shows an isotropic model, i.e., $\xi = 0$ with $\gamma_* = 1$. Similarly, the plot also represents the case where the underlying motion in the Newtonian background has a constant anisotropy. The blue dotted and orange dotted-dashed line in the plot is a case for radial anisotropy, i.e., $\xi = 0.6$, and tangential anisotropy with $\xi = -0.6$, respectively. Indeed, the plot clearly shows that Newtonian gravity alone is insufficient to explain the observational VD for DF44, opening up a scenario for alternative gravity or DM. The plot additionally refers to a most commonly studied scenario assuming a DM halo contributing to the Newtonian dynamics. For this, we look into a well-studied cuspy profile, i.e., NFW [36], assuming the following DM density distribution, $\rho_{NFW}(r) = \frac{\rho_s}{\frac{r}{r_s}\left(1+\frac{r}{r_s}\right)^2}$, where ρ_s and r_s are the characteristic density and radius, respectively. Both the model parameters (ρ_s, r_s) can be correlated to the concentration parameter ($c = r_{200}/r_s$) and virial mass (M_{200}) (see 1.2.4 for more details). Using the similar approach as specified in [211] to model DM halo and keeping γ_* as an additional free parameter, we obtain the constraints on ξ and M_{200} to be -0.8 and $3.98\times10^{10}\ M_\odot$ (c fixed from $c-M_{200}$ relation [222]). The constrained parameters (ξ, M_{200}) are of similar order as reported in [211]. The radial variation of the VD in the DM framework is shown via a green dashed line

in Fig.2.1. The evaluated χ^2_{red} for the particular DM case is 0.75. The green solid line in Fig.2.1 representing the DM case shows that NFW is a consistent choice for the observational VD of DF44.

Thus, DF44 becomes the perfect system to check the alternative scenario of the gravity models in comparison to the DM. In the following, we study and analyze the consistency of the selected three alternative gravity models, i.e., MOND, $f(R)$, and RGGR, to study the kinematics of the DF44 galaxy. In addition to the gravity model parameters, we have model parameters describing the mass content, such as γ_* and the anisotropy parameter (ξ), that are also fitted with the observations.

2.3 Gravity models

The modification to the net potential on galactic scales provides an alternative description to the observed discrepancy between the stellar and the total dynamical mass of a galaxy. In view of this, we would look into the kinematics of a specific ultra-diffuse galaxy, viz. DF44, from the perspective of three alternative gravity models. The models we focus on are MOND, $f(R)$, and RGGR. The phenomenological study of a DM-dominated galaxy such as DF44 in the presence of modified gravity can provide an alternative scenario to explain the overall kinematics without any need to invoke the DM component and, therefore, provides an alternative approach toward studying UDGs that are DM-dominated.

Milgromian Newtonian Dynamics (MOND)

MOND is characterized by an acceleration scale (a_0) as discussed in Sec.1.2.1. The acceleration in the MOND framework for the galactic scales is [63, 74],

$$a(r) = \frac{GM_{MOND(r)}}{r^2} = \frac{a_N}{\sqrt{2}}\left(1+\left(1+\left(\frac{2a_0}{a_N}\right)^2\right)^{1/2}\right)^{1/2}.$$

Here, a_N is the Newtonian acceleration ($\propto 1/r^2$), and $a_0 = 1.14 \times 10^{-8}\ cm/s^2$ [74]. We need to determine the modified mass function associated with the alternative gravity model to analyze the behavior of LOS VD in an alternative gravity framework as defined in Eq.2.3. The mass contribution associated with the MOND framework (M_{MOND}) has an additional contribution dependent on the acceleration scale and can be evaluated from the above equation. Substituting M_{MOND} in Eq.2.3 evaluates the radial line of sight variation of VD in an alternative framework. Although MOND has no free parameters in the model, our analysis includes a mass-to-light ratio γ_* and anisotropy parameter that we aim to constrain statistically. We compare three different anisotropic models associated with the analytical VD profile as discussed in Sec.2.2. The previous literature of MOND that studies the kinematics of DF44 [112] assumes a Sersic-like density model scaled by a mass-to-light ratio to model the UDG. In our work, we give a more robust analysis by utilizing an equivalent reduced form for LOS VD and studying the favorability of three different anisotropic profiles, as discussed above.

$f(R)$ gravity (model A)

The $f(R)$ gravity model selected, replaces the Ricci scalar (R) in the action of gravity with a generalized functional form of $f(R)$ [26, 215] (see Sec.1.2.3.1 for more details). The solution for the potential in the weak-field limit adds a Yukawa-like term to the Newtonian potential given as

$$\phi(r) = -\frac{GM_{mog}(r)}{r} = -\left(\frac{GM}{1+\delta}\right)\frac{1+\delta e^{-r/\lambda}}{r},$$

where δ is the coupling parameter that is assumed to vary within the range $(-1, 0)$ [175] and λ is the scale length, which is characteristic of the size of the galaxy.

Similar to the case of MOND, we examine the modified kinematics of the DF44 galaxy in the $f(R)$ framework. The modified kinematics in the presence of an alternative gravity model is evaluated by substituting the effective mass of the system in the presence of modified gravity model M_{mog} in Eq.2.3. However, unlike MOND, the $f(R)$ model has two free parameters, δ and λ, which need to be constrained. Additional parameters to be constrained from observations

are mass modeling parameters such as γ_* and an anisotropy parameter (dependent on the profile discussed in Sec.2.2).

RGGR

The third model we analyze with respect to DF44 is a quantum gravity model called Renormalization Group correction to General Relativity (RGGR). The RGGR model [89, 190] studies the running of coupling parameters present in the action of gravity on the astrophysical scales. The solution for the equation of motion for the logarithmically varying G (Sec.1.2.4) returns

$$a_{RGGR}(r) = \frac{GM_{RGGR}(r)}{r^2} = a_N(r)\left(1 - \frac{c^2\bar{\nu}}{\phi_N(r)}\right),$$

$a_N(r)$ and $\phi_N(r)$ in the above equation are the Newtonian acceleration and potential contribution, respectively. Also, the gravity model is constrained by two phenomenological parameters, i.e., ν and α, which can be coupled into a single component, i.e., $\bar{\nu} = \nu\alpha$. In the above equation, $\phi_N(r)$ is the Newtonian potential, which in isolated cases corresponds to the potential energy of the galaxy alone. However, DF44 is embedded in the Coma cluster, which might influence the potential energy of the DF44 galaxy. The effect is similar to the violation of the Strong Equivalence Principle (SEP) in MOND.

All three scenarios for modified gravity models stated in this section reduce to Newtonian gravity at a certain limit. The dependence of the alternative model on the baryonic mass component of a galaxy necessitates the modeling of the galaxy under consideration, which incorporates the free parameters (γ_* and ξ). On top of the mass-model parameters, depending on the gravity model, we have additional free parameters that need to be constrained from the observational VD data for DF44. Our analysis uses a Bayesian technique to scan the parameter space for each gravity model uniquely.

2.4 Methodology

The constraint on the model parameters for a given gravity model when compared with the observational VD for DF44 is computed via Markov Chain Monte Carlo (MCMC) sampler [203] as discussed in Sec.1.3. Assuming that the errors in the observations follow a Gaussian distribution, the likelihood is defined as

$$\mathscr{L}(\boldsymbol{\theta}) = (2\pi)^{(-N/2)} \left\{ \prod_{i=1}^{N} \sigma_{err}(r_i)^{-1} \right\} exp \left\{ -\frac{1}{2} \sum_{i=1}^{N} \left(\frac{\sigma_{obs}(r_i) - \sigma_{LOS}(r_i, \boldsymbol{\theta})}{\sigma_{err}(r_i)} \right)^2 \right\}, \qquad (2.9)$$

where N is the number of observational datapoints and σ_{err} represents the uncertainity on the observations for a given distance r_i. Also, $\sigma_{obs}(r_i)$ corresponds to the VD observations, and $\sigma_{LOS}(r_i)$ is the analytical LOS VD calculated at r_i for the alternative gravity model as defined in Eq.2.3. The LOS VD in the modified gravity framework has free model parameters (θ) corresponding to the mass distribution model (γ_*, ξ) and from the chosen alternative gravity model. In the case of MOND, the scale parameter a_0 is fixed from the observations, hence we only study the behavior of mass modeling parameters. The parameters for the $f(R)$ gravity include the coupling parameter β and scale radius r_c. Alternatively, the RGGR model has a single mass-dependent parameter $\bar{\nu}$, phenomenologically constrained from the observations.

This chapter aims to test the gravity models for all three scenarios of anisotropy profiles as discussed in Sec.2.3. The simplest scenario assumes that the tangential and the radial components of the anisotropy parameter in Eq.2.2 are equal (isotropic motion), i.e., $\xi = 0$ and motion of the objects in the galaxy is truly radial. An alternative case assumes that the anisotropy parameter is a constant between $(-\infty, 1)$. The negative values of ξ indicate that the kinematics of the object in the galaxy is dominated along the tangential orbit. Alternatively, $\xi = 1$ indicates that the orbits of the clusters are completely radial. For the third case, we assume the anisotropy profile to have an Osipkov-Merritt form as given in Eq.2.2. This radial profile introduces a free parameter, scale radius (r_a). Thus, in addition to gravity model parameters and mass to light factor, we have additional parameters coming from the choices of ξ in the definition of VD.

For our sampler, we assume flat priors on the parameter space that is varied in a wide range.

For the scenario where ξ is treated as a constant, the parameter varies within a wide range of $(-10, 1)$. This choice for the variation in ξ incorporates the anisotropy parameter's radial and tangential behavior. Similarly, for the third case where $\xi(r)$ has a radial dependence, the anisotropy profile is parameterized by scale radius r_c and is varied across the scale of the galaxy.

To compare the three scenarios and infer the preference of one over the other, we take the help of Bayesian Inference Criteria (BIC)[201] (see Sec.1.3 for a detailed discussion). To quantify the favorability of the model (say A and B), we evaluate

$$\Delta BIC = BIC_B - BIC_A \tag{2.10}$$

A positive difference between the BIC of the two anisotropy scenarios hints towards the preference of the first model over the second. According to the criteria, if the difference is less than 2, it suggests that both the models are performing equally well, and the result is inconclusive. Alternatively, if the difference is more significant than A, it suggests an inclination toward the second model with ΔBIC between $2-6$, implying a positive inclination, and greater than 6 is considered a strong inclination toward the second model.

Model	χ^2_{red}	BIC
MOND	0.39	11.68
$f(R)$	0.89	20.67
RGGR	0.45	15.77
NFW	0.75	17.69

Table 2.1: The table summarizes the goodness of fit and BIC for the DM and the alternative gravity models for a constant anisotropic parameter.

2.5 Results for DF44

For the analysis of three gravity models probed, we employ an MCMC technique to scan the posterior parameter space corresponding to the model. This requires setting the prior range for

the model parameters corresponding to each gravity model. In the present analysis, we assume a flat prior space on each parameter space as compiled in Table.2.5. Depending on the gravity mode, we run a burn-in of 0.1 and ensure that the acceptance fraction lies within $0.2 - 0.5$.

For our analysis, the gravity models are probed assuming three distinct variations of the VD kinematics. For the reference, here we show the corner plots for the MCMC runs only for the case where anisotropy is assumed to be a constant.

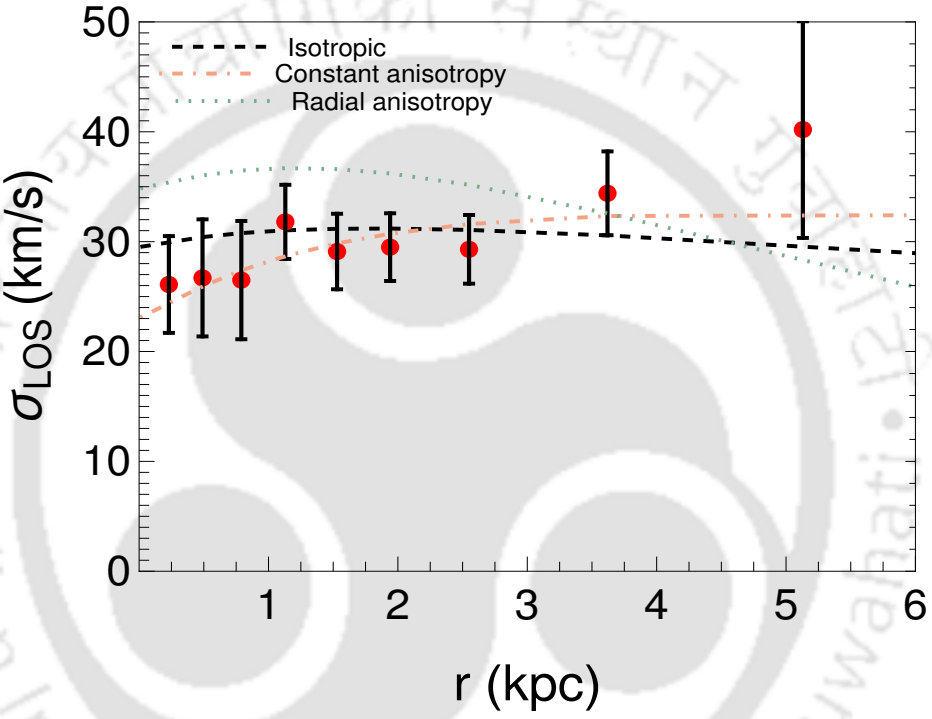

Figure 2.2: The analytical VD radial profile assumes that the underlying gravity is MOND. The red dots with error bars represent the observational data for DF44 [111]. The dashed black line shows the VD profile for an isotropic $\xi = 0$ model in the MOND scenario. The orange dotted-dashed line represents the case for a constant anisotropy, and the green dotted line shows the VD for a radial anisotropy profile as discussed in Eq.2.2.

MOND

Our analysis looks into MOND for different choices of the anisotropy parameter as discussed in Sec.2.2. For the first case, the VD kinematics is assumed to be isotropic, i.e., $\xi = 0$. Thus,

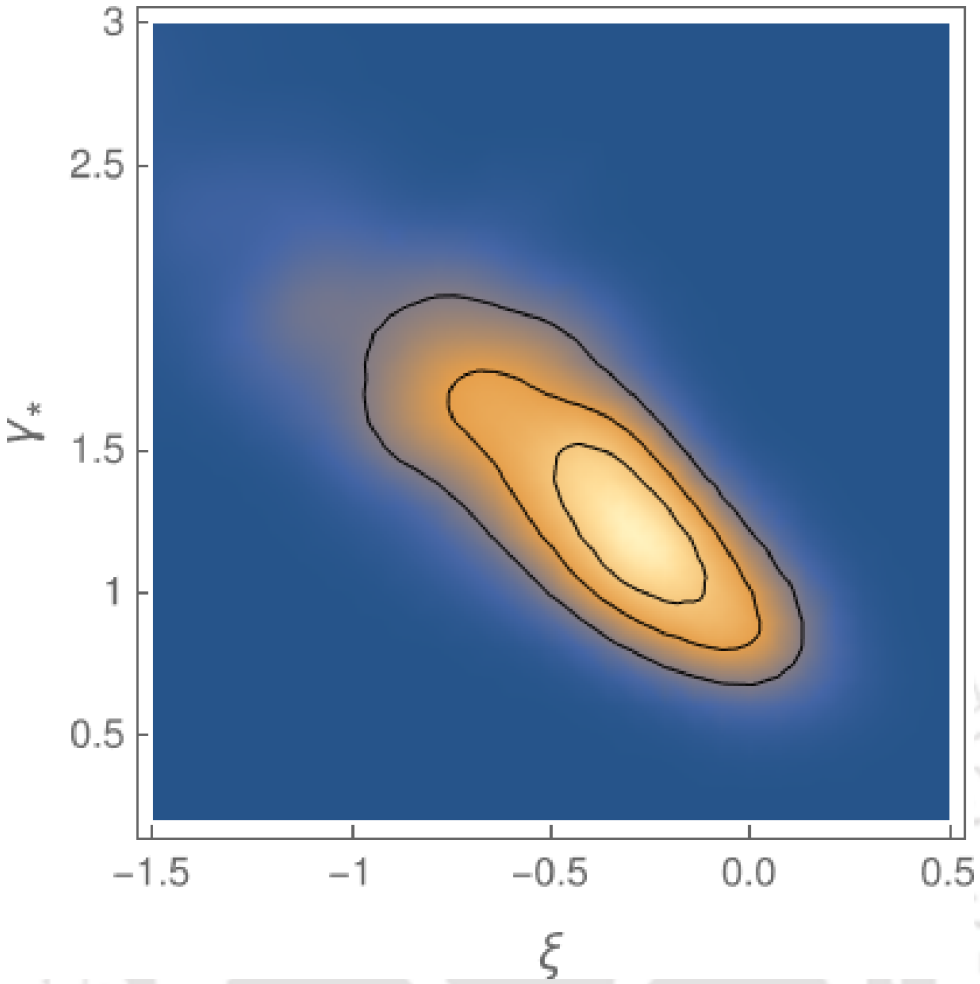

Figure 2.3: The posterior distribution for the MOND model. The parameters corresponding to the model involve only the mass-to-light ratio γ_* and ξ.

the model has a single free parameter γ_* that is constrained from the data. For the particular scenario, the best-fit value obtained for γ_* is 1.02. Substituting the best-fit value, a dashed blue line in the left panel of Fig 2.2 shows the radial variation of VD in the MOND framework. The red dots with the error bar constitute the observational dataset for DF44 [96]. Similarly, the second case assumes ξ as a constant with no radial dependence. Thus, depending on the signature of ξ, the dynamics of the galaxy can be radial ($\xi > 0$) or tangential ($\xi < 0$) in nature. Constraining the two free parameters $\{\gamma_*, \xi\}$, we obtain mass-to-light ratio $\gamma_* = 1.45$ and $\xi = -0.51$. The negative value of ξ highlights the tangential nature of the anisotropy profile. The variation of VD for the second case obtained by substituting the best-fit value is plotted via a dashed blue line in the middle panel of Fig 2.2. Here, we also show the posterior distribution of the parameter pair $(\gamma_* - \xi)$ in Fig. The contour clearly indicates a well-defined regions of maximum likelihood. The third case for the radially dependent anisotropic profile introduces

ξ	γ_*	χ^2_{red}	BIC
$\xi = 0$	1.02	0.64	9.49
$\xi = const = -0.51$	1.45	0.41	11.68
$\xi(r)(r_a = 5.67)$	1.00	3.96	36.54

Table 2.2: The constrained best-fit model parameters in MOND. The three scenarios in the table represent the different choices for the anisotropy parameter with $\xi = 0$, ξ=const, and $\xi(r)$ as the isotropic, constant, and Osikpov-Merritt profile. The acceleration scale for the MOND model (a_0) is fixed from the observations. The χ^2_{red} measures the goodness of fit for each case.

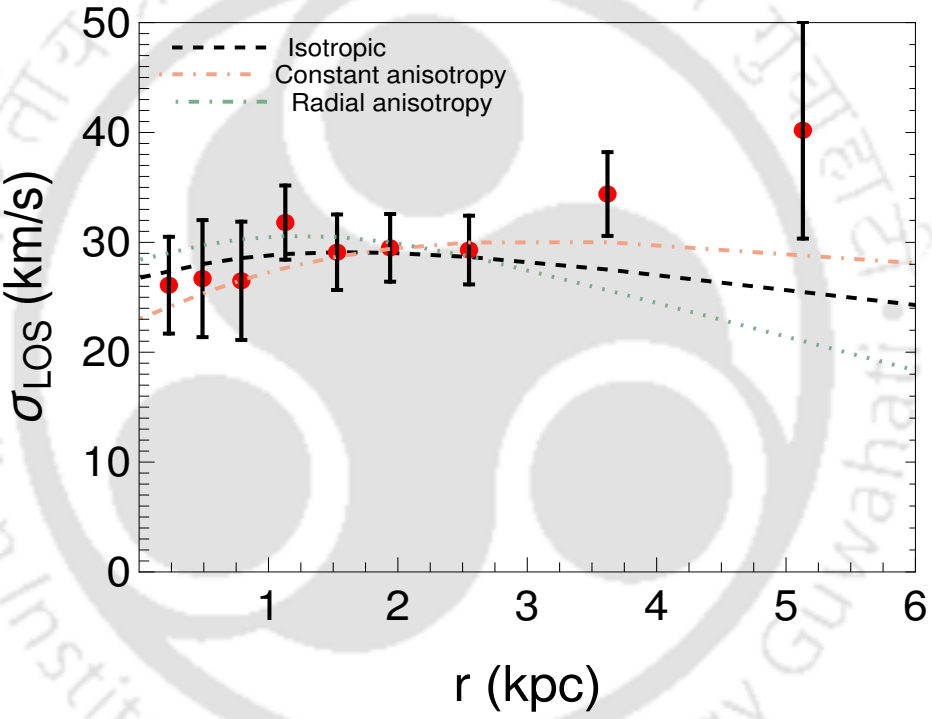

Figure 2.4: The radial VD variation for DF44 galaxy under the assumption that the underlying gravity is $f(R)$. The three different anisotropy profiles studied, i.e., $\xi = 0$, $\xi = const$, and $\xi(r)$, are shown via black-dashed, orange dotted-dashed, and green dotted lines, respectively. The red dots with the error bar correspond to the observational VD data points for the DF44 [111].

the free parameter (r_a), determining the scale radius of the anisotropy profile. For this case, the radial VD is shown in the last panel of Fig 2.2 with the obtained best-fit values are $\gamma_* = 1.02$ and $r_a = 5.73$ kpc. The summarized constrained parameters obtained for all different choices of anisotropy are also compiled in Table.2.2.

Table.2.2 also contains the measured $\chi^2_{\rm red}$ inferred from the best-fit MOND parameter for

the three choices of the anisotropy model, together with the BIC values. From Table.2.2, we observe that the γ_* obtained in all three scenarios are similar and are consistent with the previous analysis done in [112]. The difference in BIC between the radial and constant anisotropy case ($\Delta BIC = 25.03$) points towards the preference of the latter choice. However, a comparison of the isotropic and best fit constant anisotropy case yielding a small $\Delta BIC = 2.1$ hints that the preference of one model over the other is inconclusive.

$f(R)$ gravity

The $f(R)$ model we study assumes a general Taylor expansion of the functional form about $R = 0$ background. The weak-field potential obtained for the model is characterized by two parameters, i.e., the coupling parameter δ and the scale radius λ. In addition to these gravity model parameters, we have the usual mass-to-light ratio (γ_*) and anisotropy parameter $\xi(r)$ and are also constrained statistically. The suggested variation of the coupling parameter δ lies within the range $(-1,0)$ and λ is scaled within the size of the galaxy. Additional priors on the parameters δ and λ remain the same as discussed in Sec.2.4.

ξ	γ_*	δ	$\lambda(kpc)$	χ^2_{red}	BIC
$\xi = 0$	1.56	-0.89	0.81	1.09	19.47
$\xi = const = -0.15$	1.66	-0.92	2.85	0.62	20.67
$\xi(r)(r_a = 4.39)$	2.49	-0.81	3.49	2.13	28.25

Table 2.3: The model parameters constrained for the f(R) model in case of DF44. In addition to the model parameters, the table contains χ^2_{red} for the individual case. We additionally measure the BIC to compare the favorability among the different anisotropy models.

Similar to the case of MOND, the $f(R)$ model is also treated for three different assumptions of the anisotropy parameters ξ. For the first isotropic case i.e., $\xi = 0$, the analysis depends on three free parameters. The best-fit value obtained for the model parameters i.e., $\{\gamma_*, \delta, \lambda\}$ evaluates to $\{1.56, -0.89, 0.81$ kpc$\}$. For an alternative case where ξ is treated as a constant, the model parameters, i.e., $\{\xi, \gamma_*, \delta, \lambda\}$ obtained are $\{-0.15, 1.66, -0.92, 2.85\}$. The corresponding posterior distribution of the parameter space is shown in Fig.2.5. The negative value for the anisotropy profile suggests a preference towards a tangential profile. The third scenario,

assuming a generalized radial anisotropy profile, adds the scale-dependent parameter r_a. The best-fit values obtained for these parameters $\{r_a, \gamma_*, \lambda, \delta\}$ result in $\{4.39, 2.49, -0.81, 3.49\}$. The parameters corresponding to the three different cases discussed above are also tabulated in Ta

. ch

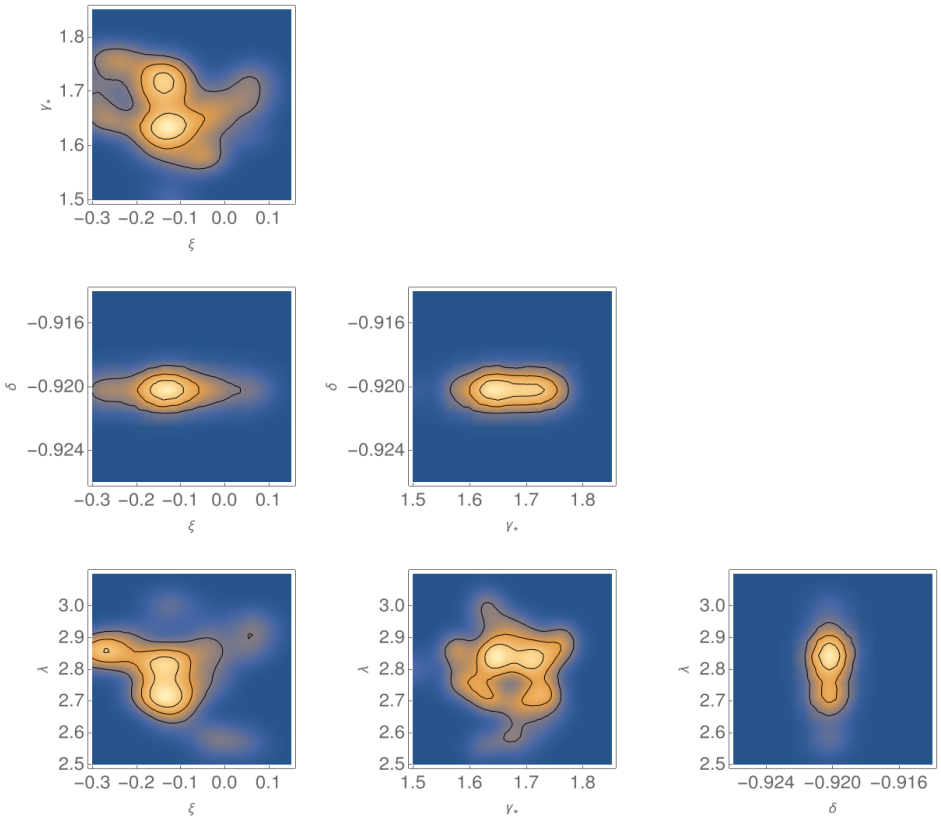

Figure 2.5: The posterior distribution for the choice of Yukawa gravity model.

anisotropy $f(R)$ gravity model is shown in Fig.(2.4). The three panels show the radial variation of VD in $f(R)$ model with different assumptions for the anisotropy parameter, i.e., $\xi = 0$ (left), $\xi = const$ (middle) and $\xi(r)$ (right). The dashed blue line in each plot shows the VD modeling for the $f(R)$ gravity obtained by substituting the best-fit values corresponding to the choice of the anisotropy profile. As can be seen from Table.2.3, the $\chi^2_{\rm red}$ is smaller for the case where anisotropy is treated to have no radial dependence. Note that although the second and third scenarios have a similar number of free parameters, the change in BIC suggests an inclination toward a constant anisotropic case. Additionally, the isotropic and tangential anisotropy modeling behave equally well with the observation that can be quantified from the difference in

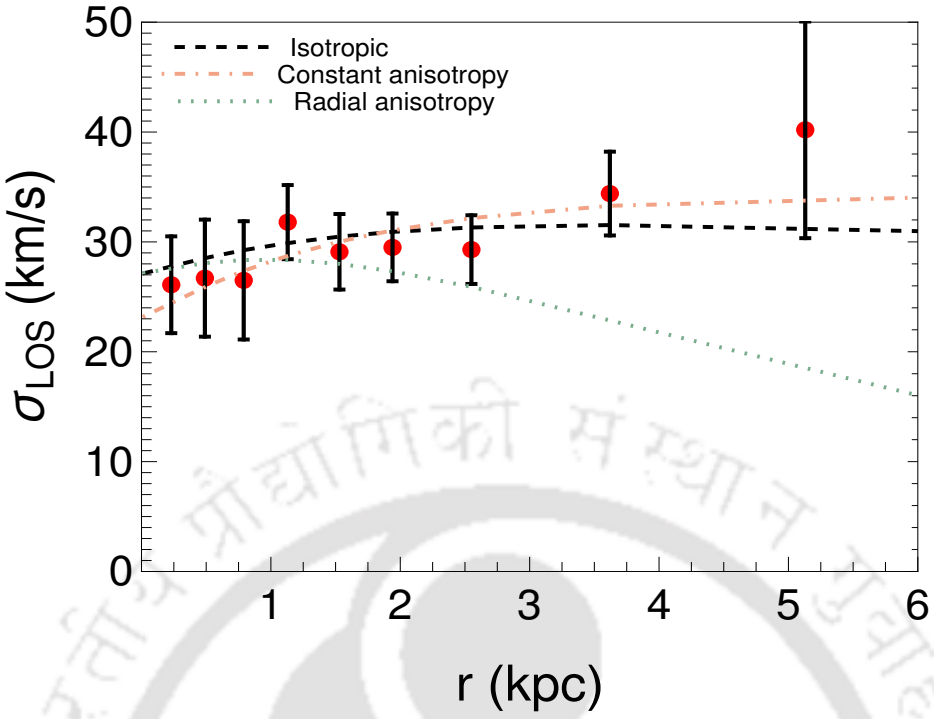

Figure 2.6: The radial VD obtained for DF44 when the underlying gravity is RGGR. The red dots with the error bar correspond to the observational VD data points for the DF44 [111]. The plot shows the VD modeling for three assumptions of anisotropy. The black dashed line represents the isotropic case; the orange dotted-dashed line is for the constant anisotropy, and the green dotted line represents the radial anisotropy case.

BIC ($\Delta BIC \sim 2$).

RGGR gravity

The solution to the weak-field limit potential in RGGR introduces a mass-dependent phenomenological parameter $\bar{\nu}$. The previous studies for the RGGR model suggest $\bar{\nu}$ to be in the order of 10^{-7} for spiral and elliptical galaxy RC data [89, 190] and 10^{-8} for UDG VDs [194]. Based on these results, for our study, we assume flat priors on the RGGR parameter ranging from [10^{-8}-10^{-6}]. Additionally, priors on the VD parameters such as (γ_*, ξ) remain similar to those discussed in the previous two alternative gravity models. For our analysis of the DF44 galaxy, we probe the kinematics for two RGGR frameworks, i.e., an isolated scenario and under the influence of external effects, as discussed below. For the standard RGGR scenario,

ξ	γ_*	$\bar{\nu}\times10^{-8}$	χ^2_{red}	*BIC*
$\xi = 0$	1.45	2.46	0.43	11.82
$\xi = const. = -0.27$	1.51	2.57	0.37	15.77
$\xi(r)(r_a = 5.56)$	1.44	1.79	1.53	22.36

Table 2.4: The best-fit model parameters for the RGGR gravity model. The table contains the constrained values obtained for gravity ($\bar{\nu}$) and mass-model (ξ, γ_*) parameters.

the potential energy contribution is comprised of the matter density of the DF44 galaxy alone. Similar to the previous models, we study three different assumptions of the anisotropy parameter. The first case with $\xi = 0$ involves two model parameters, i.e., $\bar{\nu}$ and mass-to-light ratio (γ_*), to be constrained from the observations. The best fit parameters evaluated from our study give $\gamma_* = 1.45$ and $\bar{\nu}$ as 2.46×10^{-8}. For the second scenario, where the anisotropy parameter ξ is treated as a constant, the estimated values of the three free parameters, i.e., (ξ, γ_*, $\bar{\nu}$) come out as (-0.27, 1.51, 2.57×10^{-8}). The corresponding posterior distribution of the free parameters belonging to the constant anisotropy scenario are depicted in Fig.2.7. For the third choice of radial anisotropy (Eq.2.2), the best-fit values for $\{\gamma_*, \bar{\nu}, r_a\}$ are 1.44, 1.79×10^{-8}, and 5.56 kpc respectively. Indeed, the constrained $\bar{\nu}$ is an order lesser than obtained from the study of spiral and elliptical galaxies but is consistent with the study of other UDGs [194]. The best-fit model parameters obtained using the sampler are also listed in Table 2.4.

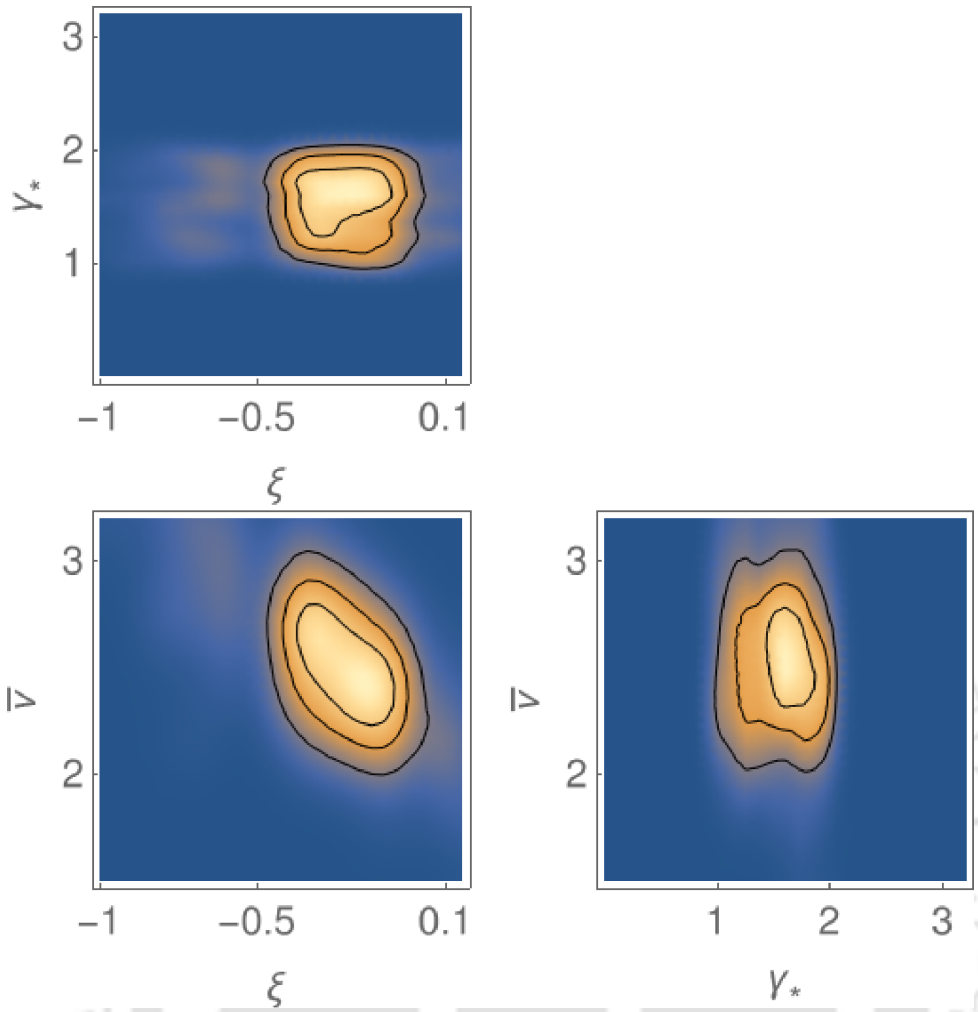

Figure 2.7: The posterior distribution relating the parameters belonging to the RGGR model.

A comparison of the radial VD profile obtained for standard RGGR scenario from statistical analysis with the observational data is shown in Fig.2.6. The three assumptions for the anisotropy profile are plotted independently with the left-most panel corresponding to $\xi = 0$, the middle panel for $\xi = const$ case, and the right-most panel studying the radial behavior $\xi(r)$ of the anisotropy parameter. Like the other MOG models studied previously, the constant anisotropic case favors a tangential profile. We also report the BIC using the best-fit parameters obtained for the three choices of the anisotropy model. The measured ΔBIC clearly shows that the radial anisotropic choice is the least favored among the three models. Additionally, between the isotropic and the tangential model, ΔBIC hints towards a slight favorability of the $\xi = 0$ choice rather than the constant anisotropic model.

To summarize, the study of the kinematics of DF44 in light of three gravity models, i.e., MOND,

$f(R)$, and RGGR, shows many important features. While comparing all three models, ΔBIC points towards the fact that the radial dependence choice of $\xi(r)$ is the least favorable. Using the best-fit r_a obtained for all three models, the radial variation for the Osikpov-Merritt profile within the size of the galaxy is shown in Fig2.8. It is also to be noted that when the anisotropy parameter is constant for all three models, the best-fit value points towards a negative value, i.e., the tangential behavior.

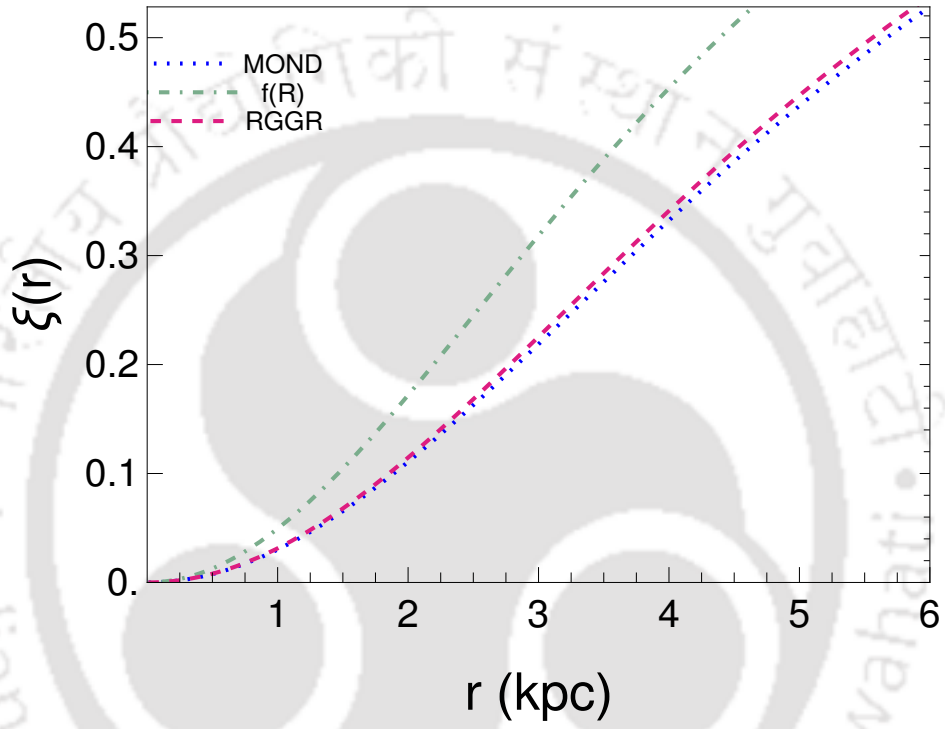

Figure 2.8: The radial Osikpov-Merritt profile for three modified gravity models. The blue dotted line depicts the anisotropy variation for the MOND model. Similarly, the green dotted-dashed and pink dashed line represents the $f(R)$ and RGGR model, respectively.

DM scenario

To check the favorability of the alternative gravity models, we compare them with the alternative NFW scenario. As the constant anisotropy case for all three gravity models shows a consistent fit with the DF44 observations, we compare the MOG analysis with a similar DM scenario to study the favorability of the models.

Model	χ^2_{red}	*BIC*
MOND	0.39	11.51
$f(R)$	0.89	22.05
RGGR	0.45	15.88
NFW	0.75	17.69

Table 2.5: The table summarizes the goodness of fit and BIC for the DM and the alternative gravity models for a constant anisotropic parameter.

For the DM halo, we found the best-fit value of the anisotropy parameter to be -0.8 and $3.98 \times 10^{10} M_{\odot}$ for M_{200}, with $\chi^2_{red} = 0.75$. The BIC evaluated using these best-fit DM parameters gives 17.69. The details of the goodness of fit and BIC measured for the three gravity models and the NFW scenarios are also compiled in Table. 2.5. The three MOG models, along with the NFW scenarios for the tangential anisotropy case, are shown in Fig.2.9. The gray dashed line in the plot represents the case of the NFW DM halo. Similarly, the blue, pink, and green dashed line represents the MOND, RGGR, and $f(R)$ models, respectively. All the MOG models shown in Fig.2.9 for a constant anisotropic choice highlight that the three MOG models are competing choices for the kinematics of DF44 when compared with the DM scenario. A comparison of ΔBIC between the MOND scenario having a constant anisotropy with the DM model shows that the former is a preferred choice to explain the VD kinematics for DF44. Alternatively, the measured ΔBIC with RGGR suggests that both models perform equally well. However, a comparison with the $f(R)$ model shows a slight preference for the NFW DM halo.

2.6 Summary

The large VD measurements for the DF44 galaxy, when compared with Newtonian kinematics, suggest a significant content of DM to explain the observed discrepancy. In this work, we explain the observed VD by assuming a modified gravity scenario in the context of three alternative gravity models, i.e., MOND, $f(R)$, and RGGR. Our analysis aims to constrain the model parameters corresponding to each gravity model. Furthermore, we require certain parameters (γ_*, ξ) to model the VD, which are additionally constrained from the observations. The con-

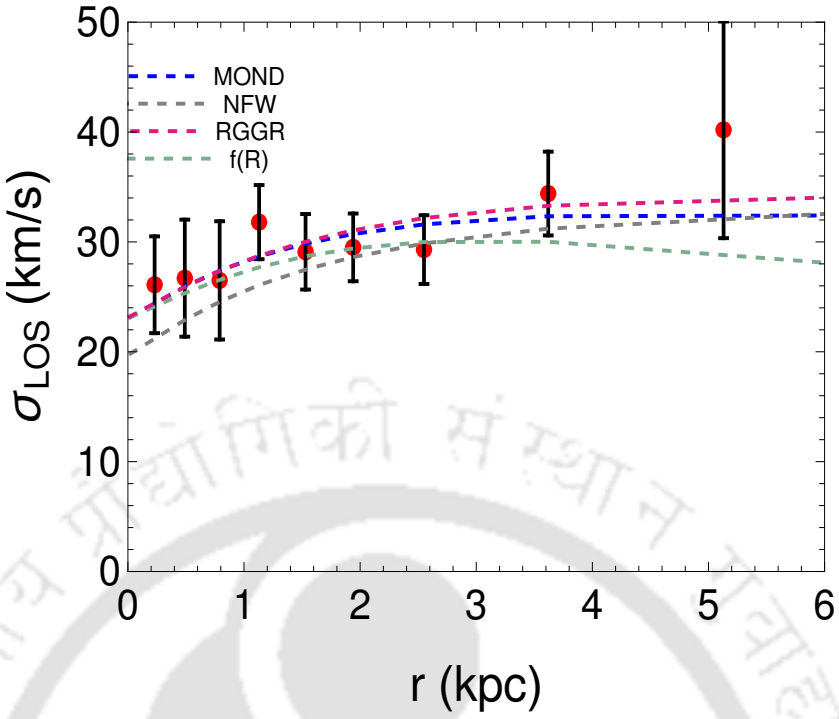

Figure 2.9: The plot compares the three alternative gravity and NFW DM models for the constant anisotropic case. The blue, pink, and green dashed lines correspond to MOND, RGGR, and Yukawa models, respectively. The gray dashed line in the plot represents the alternative DM scenario.

sistency of a gravity model is quantified by a factor of $\chi^2_{\rm red}$. Additionally, we evaluate BIC to check the favorability of one anisotropy scenario with another.

In the case of three MOGs, a comparison of $\chi^2_{\rm red}$ for the anisotropy cases (isotropic, constant, radial) shows that a choice of radial profile fits poorly with the observations. This can also be observed from the difference in BIC between the scenarios. It is also noted that for all three gravity models, the $\chi^2_{\rm red}$ is slightly improved or remains similar as one moves from isotropic to a constant anisotropy case. However, the difference in BIC between the two cases ($\xi = 0$ and $\xi = const$) shows that the results are inconclusive to favor one model over the other for the MOND and $f(R)$. Similarly, for the RGGR model, the isotropic model has a slight edge over the tangential choice of the anisotropy parameter. For the case of $f(R)$ model, the $\chi^2_{\rm red}$ for isotropic versus $\xi = const$ case shows that both the models fit equally well with the observations of DF44. A small difference of ΔBIC between the two scenarios shows that the result is inconclusive to favor a certain model. An additional point to be noted is that for the constant

anisotropy case for all three MOG models, our analysis shows that the tangential profile is preferred over the radial choice.

The RGGR model has a single mass-dependent parameter $\bar{\nu}$. For the isolated RGGR case, the best-fit value obtained for the parameter is an order less than constrained by the spiral or elliptical galaxies. However, the claim is consistent for the ultra-diffuse as they are comparatively smaller. Also, similar to the other two gravity models, the ΔBIC measured suggests that the radial anisotropy profile is the least favorable among the three choices for the anisotropy. Finally, in this analysis, we compare our choice of gravity models with an NFW DM halo model. The comparison of BIC evaluated for each case suggests MOND as a preferred choice. However, the DM model has a slight edge over the $f(R)$ model, whereas RGGR performs equally well.

Thus, the present chapter explains the observed VD for a DM-dominant DF44 in the context of three alternative gravity models. However, some UDGs are observed to show no DM contained within them. The observed VD for such galaxies is similar to the measured Newtonian one. This suggests that the dynamical mass contained within the galaxy is equivalent to the baryonic matter. Thus, the consistency of such systems, when probed in the context of MOG, provides a test for alternative gravity models.

Chapter 3

Velocity dispersion of DM deficit ultra-diffuse galaxies

3.1 Introduction

The structure formation for a cosmological ΛCDM model suggests that a galaxy is enclosed within a DM halo whose size is much greater than the disk scale within [223, 224]. Therefore, the observation of the DM-deficit nature of two UDGs, i.e., NGC1052-DF2 (hereafter DF2) [105] and NGC1052-DF4 (hereafter DF4) [98], with the Dragonfly Telescope (DTA) [97, 209] made an exciting place to explore modified gravity models. The two UDGs are dominated by globular clusters, with DF2 and DF4 containing 10 and 8 respectively [98, 105]. However, comparing the measured dynamical and stellar mass probed using VD shows that such galaxies do not require the additional DM component to explain the kinematics. Thus, such systems become an attractive avenue for studying the behavior of the alternative gravity models and looking into the constraints on the model parameters of the theory. The study of MOND [225] for DF2 and DF4, incorporating the external effects of the host galaxy, shows that the model can

consistently explain the kinematics of UDGs [106, 226, 227]. Similar VD analysis of gravity theories such as Scalar Tensor Vector Gravity (STVG), Emergent, and Weyl Conformal shows that the dynamics are consistent and lie within the 1σ range of the observational data for both the UDGs [119, 228, 229, 230]. The gravity models, such as DHOST, also show potential for explaining the gravity models [107, 108].

Our analysis aims to study and constrain the model parameters of two well-known gravity models viz $f(R)$ and Renormalization Group correction to General Relativity (RGGR). The $f(R)$ gravity model replaces the Ricci scalar (R) in the action of gravity with a functional form of R [26, 54, 55, 231]. The stability of the model and the presence of unwanted ghosts put a specific constraint on the choice of the $f(R)$ form [80, 232]. Keeping this in mind, we study the kinematics of both the UDGs for two choices of the functional form of $f(R)$. The first choice assumes a generic expansion of $f(R)$ about the Minkowskian background ($R = 0$) [173, 175]. The weak-field potential for the model adds a Yukawa-like term to the Newtonian contribution and is dependent on the coupling and scale parameters. Alternatively, we also look into the weak-field limit of the gravity model with $f(R) \propto R^n$ where $n > 1$ is the lower limit for the slope of the functional form [68, 176, 177]. The weak-field limit of the model introduces a slope-dependent radial term to the Newtonian potential. The solution for both gravity models introduces free parameters, which are constrained by comparing the modified VD kinematics with the observational data. The third alternative model that is looked into studies the renormalization correction of the coupling parameter of gravity, namely RGGR. The model probes the variation of the gravitational constant (G) with the scale of the Universe [61, 89]. The weak-field solution for the G running introduces a free parameter, i.e., $\bar{\nu}$, that scales linearly with the mass of the galaxy [190]. The variation in $\bar{\nu}$ within the range of 10^{-7} is shown to explain the kinematics of spiral and elliptical galaxies [89, 190, 191]. Thus, in this analysis, we look into the consistency of UDGs (DF2 and DF4), whose size is much smaller than a typical spiral and elliptical galaxy, and study the behavior of the mass-dependent $\bar{\nu}$ parameter.

The structure of the chapter is as follows. Sec.3.2 discusses the analytical VD formalism for the UDGs. Here, we also summarize the observational data and the mass modeling of DF2 and DF4. The following Sec.3.3 looks into the alternative gravity models studied. Lastly, we discuss the methodology and summarize the results of our analysis of DF2 and DF4 in Sec.3.4.

A brief discussion about the summary of the chapter is written in Sec.3.5. ‘

3.2 VD formalism and mass modeling for DF2 & DF4

The VD ($\sigma(r)$) for a spherically symmetric system is defined using Jean's equation Eq.2.1 as discussed in Sec.2.2. To probe the kinematics for UDGs (DF2 & DF4) in an alternative gravity framework, we assume an isotropic system ($\xi = 0$), implying equal radial and tangential components. For the assumption that the system is isotropic, the expression Eq.2.1 for VD reduces to,

$$\sigma^2(r) = \frac{1}{\rho(r)} \int_r^\infty \rho(r')a(r')dr'.$$

However, as discussed in Sec.2.2, the physically relevant quantity measured in astrophysical observation is the projection of the above-mentioned radial VD on the line joining the observer and the center of the system, termed the line of sight (LOS) velocity dispersion. Thus, σ_{LOS} for an isotropic system expressed in terms of the radial VD and the density profile of the system is written as

$$\sigma^2_{LOS}(r) = \frac{\int_r^\infty \frac{r\sigma^2(r)\rho(r)}{\sqrt{r^2-r^2}}dr}{\int_r^\infty \frac{r\rho(r)}{\sqrt{r^2-r^2}}dr}. \tag{3.1}$$

The LOS VD is a function of r, which is the projected distance from the center of the galaxy. Therefore, given the weak-field limit potential for a gravity model, one can compute the radial acceleration, which evaluates VD ($\sigma(r)$) for a given mass density of the galaxy. For a given modified gravity, the LOS VD is compared with the observational data, which helps to constrain the free parameters of the model. For the first part of the study, we analyze the dynamics of DF2 and DF4 in light of two gravity models, i.e., $f(R)$ gravity (with two different choices for the functional form) and the RGGR gravity model. The LOS VD modeling for both UDGs requires an estimate of the radial mass density profile. The density profiles for DF2 and DF4 are found

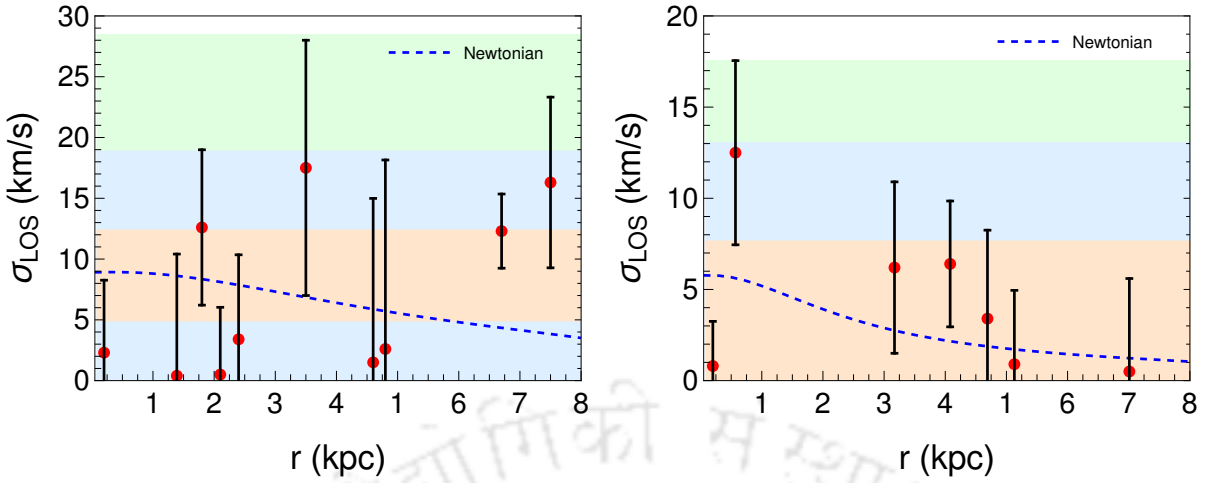

Figure 3.1: Radial variation of LOS VD for DF2 (left) and DF4 (right) shown using a blue dashed line, assuming the underlying gravity to be Newtonian with no DM component. The red dots with the error bars are the observational VD measurements for individual globular clusters present within both the galaxies [98, 105]. Additionally, we show the 1σ (orange), 2σ (blue), and 3σ (green) deviations of VD [226] from observations.

to be similar and can be approximated as [119]

$$\rho(r) \sim \frac{40\rho_0}{63 r_s} exp\left(-\left[\frac{11r}{10r_s}\right]^{4/3}\right), \tag{3.2}$$

where ρ_0 is the characteristic surface mass density and r_s is the effective radius. Both the ultra-diffuse galaxies are at a distance of about 20 Mpc [98, 105], resulting in the density parameters (ρ_0, r_s) for DF2 to be (1.25×10^7 $M_\odot$/kpc^2, 2 kpc) and (1.15×10^7 $M_\odot$/kpc^2, 1kpc) for DF4. Given the density profiles, for a gravity model, one may estimate the VD for the system.

To begin with, we probe the standard gravity paradigm described by Newtonian gravity from the observational data for the two UDGs. The acceleration for a spherically symmetric system in Newtonian gravity is written as $\left(a(r) = -\frac{G}{r^2}\int_0^r 4\pi\rho(r')r'^2dr'\right)$. Here, G is the gravitational constant, and $\rho(r)$ is the approximate density distribution of UDG as given in Eq.(3.2). The LOS VDs evaluated for both the galaxies are shown in Fig.3.1. The left panel is for DF2, and the right one shows the case for DF4. The blue dashed lines in both panels show the estimated radial variation of LOS VD. Additionally, the orange, blue, and green shaded regions are the 1σ and 2σ and 3σ regions on the predicted VD measurements [226]. The red dots with error

bars are the observations of the individual globular objects present within the galaxy, i.e., 10 such objects for DF2 [105], and 7 objects for DF4 [98].

The UDGs mentioned above, due to the lack of DM, are the best candidates to probe the parameter space for different alternative gravity models, resulting in LOS VDs different than the Newtonian curves shown in Fig.3.1. In particular, $a(r)$ will have an additional term for the modified gravity in the weak-field limit compared to the Newtonian scenario. We use this modified expression for acceleration to estimate the velocity dispersion and constrain the gravity model parameters from the UDG observations.

3.3 Gravity models

The DM-deficit nature of both the UDGs leaves scope to check the consistency of gravity models. In this chapter, we study the kinematics of the two UDGs by choosing two types of gravity models viz., $f(R)$ gravity and Renormalization Group corrected General Relativity (RGGR). The validity of these gravity models is probed by scanning the free model parameter space against the UDG velocity dispersion observations.

$f(R)$ gravity

In an alternative approach to ΛCDM, we can assume E-H action to have a general $f(R)$ form instead of Ricci scalar R [54, 162]. To look into the kinematics of DF2 and DF4, we study two cases of $f(R)$, also discussed in Sec.1.2.3. The first model assumes a generalized functional form that is Taylor expanded about a flat background. Similarly, a specific form of $f(R)$ that is $\propto R^n$ is chosen and analyzed for the second model.

$f(R)$ gravity (model A) : For the first choice, following [165, 175], we consider a model with a general Taylor expansion of the functional $f(R)$ form about the Minkowskian background. The solution for the potential in the weak-field limit, as discussed in Sec.1.2.3.1 is $\phi(r) = -\left(\frac{GM}{1+\delta}\right)\frac{1+\delta e^{-r/\lambda}}{r}$, where δ is the coupling constant, determining the nature of the additional

force arising from the exponential term, and λ is the scale length, which is the characteristic of the size of the galaxy. Both the model parameters can be statistically constrained for DF2 and DF4. The parameter δ is considered to be negative and within the range $-1 < \delta < 0$ [174], implying the repulsive nature of Yukawa force. The previous study suggests that the phenomenological parameter δ is constrained within the range $(-0.7, -0.9)$ [175]. The scale parameter λ is dependent on the size of the systems and, hence, varies with the galaxies that are probed.

$f(R)$ gravity (model B): The second $f(R)$ model 1.2.3.2 that is looked into replaces the Ricci scalar (R) in the action by a power-law form given as $f_0 R^n$ [68]. Solving the equation of motion in the weak-field limit for the spherically symmetric system yields the potential, $\phi(r) = -\frac{Gm}{2r}\left[1 + \left(\frac{r}{r_c}\right)^{\beta}\right]$, where G is the Newtonian gravitational constant, r_c is the scale radius and β is related to the power (n) of the model as described in Eq.1.23. Under the conditions that the gravity is Newtonian on the Solar system scales and the potential converges even at large distances, β is constrained in the range $0 < \beta < 1$ [68]. Additionally, r_c is the scale radius at which the modified gravity takes effect. Thus, the scale radius varies independently with the galactic system studied.

RGGR

Following [89], Renormalization Group corrections to General Relativity (RGGR) incorporate the effect of running G with the energy scale of the Universe. Similar to the discussion in Sec.1.2.4 and for the study of DF44 in Chapter2, for the logarithmically varying G, with the energy scale μ the solution for the modified potential in the weak field limit is $\phi'_{RGGR}(r) \approx \phi'_N(r)\left(1 - \frac{c^2\bar{\nu}}{\phi_N(r)}\right)$, where ν and α are coupled into a single free parameter $\bar{\nu}$. Also, $\phi'_{RGGR}(r)$ and $\phi'_N(r)$ are the RGGR and Newtonian acceleration due to gravity, respectively. For the spherically symmetric galaxy such as UDGs, Newtonian potential,

$$\phi_N(r) = -\left(\frac{GM(r)}{r} + 4\pi G\int_r^{\infty}\rho(r')r'dr'\right).$$

The chapter aims to probe the dynamics of both UDGs in the context of the alternative gravity models discussed above. For a MOG model, the galaxy's kinematics are modified, adding to the Newtonian term. Such additional components depend on some free parameters that are constrained by comparing the model with the observational VD data.

3.4 Methodology and Results

Methodology : The analysis aims to verify the consistency and constrain the parameters of alternative gravity models to explain the kinematics of the galaxies DF2 and DF4. The parameters of the gravity model are constrained by defining a likelihood function for each galaxy under the assumption that errors follow a Gaussian distribution similar to the definition expressed in Eq.2.9. For the analysis of both UDGs, $\sigma_{LOS}(r_i, \boldsymbol{\theta}, \boldsymbol{p})$ is the analytical LOS VD calculated at every radius for the choice of gravity model as defined in Eq.3.1. In this definition, the parameters $\boldsymbol{\theta}$ represent the global ones, while $\boldsymbol{p}$ is solely dependent on the individual galaxy property and are the local parameters of the gravity model. The kinematics for both the UDGs are looked into for two different alternative gravity models viz. $f(R)$ (model A and B) and RGGR. For the $f(R)$ gravity the global parameters are $\boldsymbol{\theta}$=$\{\delta\}$ and $\boldsymbol{\theta}$=$\{\beta\}$ for model A and B respectively. The local parameters for model A and B are $\{\boldsymbol{p}\}$=$\{\lambda\}$ and $\{\boldsymbol{p}\}$=$\{r_s\}$, respectively. Both of these parameters depend on the size of a galaxy. Contrary to the $f(R)$ model, RGGR gravity has a single mass-dependent free parameter, i.e., $\boldsymbol{\theta}$=$\{\bar{\nu}\}$. However, the mass being similar for both the UDGs, one may treat the $\bar{\nu}$ as a global parameter in this study. To compute the global parameters, we now define the total likelihood function. The observations for both the galaxies being independent of each other allow the total likelihood function to be defined as the product of the likelihood function for each galaxy

$$\mathscr{L}(\boldsymbol{\theta}, \boldsymbol{p}) = \prod_{j=1}^{2} \mathscr{L}_j(\boldsymbol{\theta}, \boldsymbol{p}), \tag{3.3}$$

The free parameters of the gravity models vary in the range discussed in Sec.2.3. The best-fit value for the parameter $\boldsymbol{\theta}$ and $\boldsymbol{p}$ are found by minimizing the log-likelihood function for the model parameters.

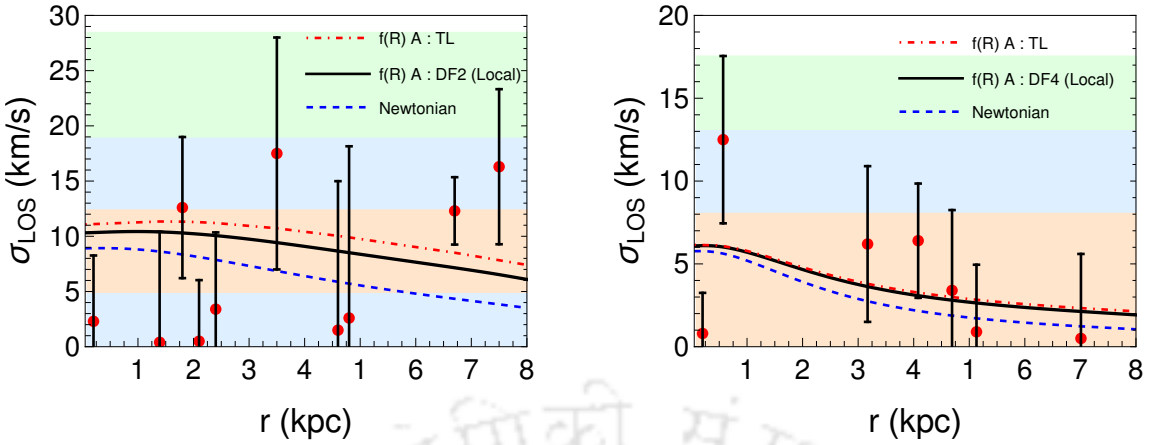

Figure 3.2: Comparison of the Newtonian radial variation of VD (blue dashed curve) for both the UDGs with the $f(R)$ gravity model A. The black solid line is the velocity dispersion for $f(R)$ gravity model A from individual likelihood analysis of the DF2 (left) and DF4 (right). The red dot-dashed lines depict the best fit LOS VD from the total likelihood (TL) analysis. Other details of the plots remain the same as given in Fig.3.1

.

Results : To study the dynamical behavior and constrain the model parameters of the two DM-deficit UDGs in the context of alternative gravity models, we compare the estimated LOS VD with the observational data. We perform the statistical analysis in two different ways. The first scenario independently constrains all the model parameters for both galaxies, which we interpret as the local estimate. For the other scenario, the global parameters for a model are fitted from both the UDG analyzed together. Meanwhile, the local parameters, like the scale parameters, are fitted individually for each UDG.

$f(R)$ gravity

$f(R)$ (model A) : The parameter δ for the $f(R)$ model A is interpreted as coupling the baryonic matter with the Yukawa term and signifies the deviation from Newtonian gravity. For our analysis, the free parameter varies in the range $(-1, 0)$. The other parameter λ is the scale radius and is assumed to lie within the size range of the UDGs. The optimized model parameter values are estimated using likelihood minimization. The best fit (δ, λ) obtained for individual analysis of DF2 and DF4 are $(-0.82,$ 6.16 kpc) and $(-0.83,$ 5.39 kpc), respectively. Table 3.1 shows

these results as the local fit parameters. As both UDGs (DF2 and DF4) have almost similar

Gravity model	**Model parameters**	**NGC1052-DF2**		**NGC1052-DF4**	
		Local	Global	Local	Global
$f(R)$ **model A**	δ	-0.82	-0.89	-0.83	-0.89
	λ (kpc)	6.16	6.80	5.39	6.50
$f(R)$ **model B**	β	0.65	0.60	0.50	0.60
	r_c (kpc)	0.30	0.40	0.25	0.35
RGGR	$\bar{\nu} \times 10^{-8}$	0.30	0.16	0.10	0.16

Table 3.1: The model parameters for different alternative gravity models fitted for DF2 and DF4 are shown above. The local columns in the table contain best-fit values for the analysis with the individual galaxy likelihood. The global column fit values are for the total likelihood. For the global analysis, the parameters δ, β, and $\bar{\nu}$ in their respective models are considered as global, and the parameters λ and r_c remained local to individual galaxies.

mass and size, the coupling and scale parameters, as seen in Table 3.1, are also similar. For the global analysis that incorporates both UDGs, δ is treated as the global parameter while the scale dependence parameters (λ_{DF2}, λ_{DF4}) vary independently for each galaxy. The global fit value for the coupling parameter δ turns out to be -0.89 and $\lambda_{DF2} = 6.8$ kpc and $\lambda_{DF4} = 6.5$ kpc. Table 3.1 shows these fit parameters as global. Comparing our result for the global parameter from UDGs with the study of elliptical galaxies [175], it is observed that δ lies within the expected range, i.e., $(-0.7, -0.9)$ from the previous phenomenological study. Also, since different galaxies have varying sizes, λ is different, but the order of the parameters does not change drastically. This signifies that the study of DF2 and DF4 is consistent with the previous analysis done on the gravity model.

Using the best-fit parameters obtained from our statistical analysis, we plot the line-of-sight VDs in Fig. 3.2. The DF2 results are shown in the left panel, and the DF4 results are in the right panel. The solid black curves in Fig.3.2 show the local LOS VD results. The red dashed lines in the plots represent the global scenario with the fit parameters optimized from the total likelihood. The solid blue line shows the Newtonian VD contribution. The 1σ and 2σ and 3σ regions on the predicted VD measurements [226] are also demonstrated by the orange, blue,

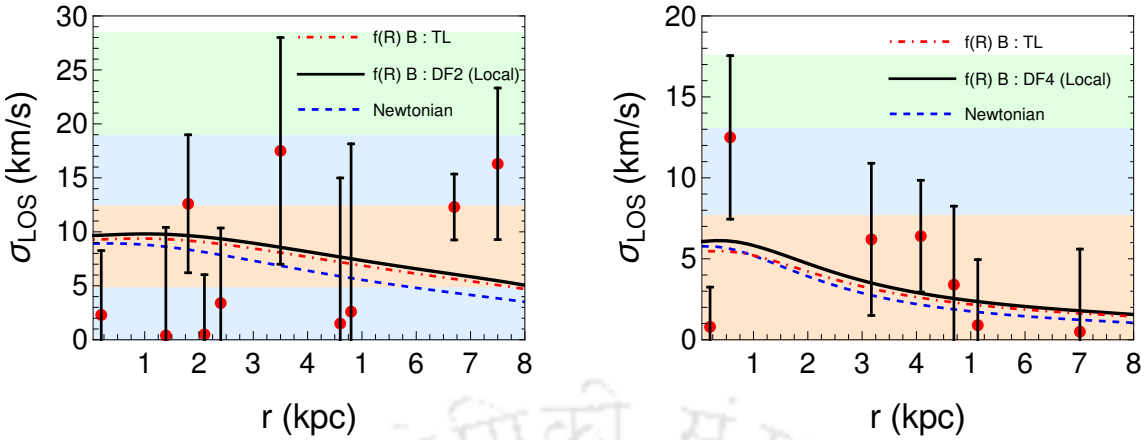

Figure 3.3: Comparison of the Newtonian radial variation of VD (blue dashed curve) for both the UDGs with the $f(R)$ gravity model B. Radial VDs for the $f(R)$ model are shown by solid black lines when both galaxies, i.e., DF2 (left) and DF4 (right), are treated independently. The VDs from the global analysis using total likelihood (TL) with both the UDGs are shown using the red dot-dashed lines. Other information about the Newtonian contribution and observations in the plots remains the same as in Fig.3.1

.

and green shaded regions, respectively. The red dots with error bars are the observations of the individual globular objects in the galaxy. Our estimated VDs for all the different fit scenarios come within the 1σ region. Comparing the LOS VDs in both galaxies, we observe that the difference between the alternative model and Newtonian gravity is smaller than in the DF4 galaxy. In general, the VD plot shows that $f(R)$ gravity is a feasible choice and can explain the kinematics for both the DM deficit UDGs. The agreement of our results with the observations is valid for the individual and global likelihood analysis of the $f(R)$ model.

$f(R)$ **(model B) :** This $f(R)$ model is also described by two free parameters (β, r_c). The dimensionless parameter β varied in the range $(0, 1)$ and has a quadratic relation with the power n as given in Eq.1.23. The parameter r_c can be interpreted as the local scale parameter varying within the size of the galaxy. The fitting parameters (β, r_c) obtained from the likelihood analysis (local & global) are summarized in Table 3.1.

For DF2 and DF4, the fit values (β, r_c) for the individual likelihood analysis obtained are $(0.65, 0.30$ kpc) and $(0.50, 0.25$ kpc), respectively. Correspondingly, the value of n evaluated

for DF2 and DF4 from Eq.1.23 is 1.92 and 1.46, respectively. For the global analysis of the combined UDGs, the β obtained is 0.60 ($n = 1.72$). In addition, the scale parameters varied locally for DF2 and DF4 are 0.40 kpc and 0.35 kpc, respectively. Comparison of the global parameter β from our study and analysis of LSB ($\beta = 0.8$) [68] shows that the difference between the two is not large. Also, the scale parameter r_c dependent on the mass of the galaxy is within the same range as obtained from the study of other LSBs. Thus, the kinematics of the UDGs are consistent with the earlier work on the choice of gravity model $f(R) \propto R^n$.

From the obtained best-fit parameters, the radial variation of LOS VD is shown in Fig.3.3. The black solid and red dashed lines in Fig.3.3 are the local and global VD contributions for the R^n gravity model for DF2 (left) and DF4 (right). The blue dashed lines in both plots are the VD contribution when underlying gravity is taken to be Newtonian. For both UDGs, the black and red dashed lines lie within the 1σ region of the LOS VD observation. Thus, a model with a specific R^n functional form for $f(R)$ can also be accommodated to explain the dynamics of our chosen UDGs. The global and local fits for the second choice of the $f(R)$ model agree with the observed kinematics of the two UDGs.

RGGR

In the case of RGGR gravity, potential in the weak-field limit is a function of a single free parameter $\bar{\nu}$. The $\bar{\nu}$ parameter is found to have a nearly linear dependence on the mass of the galaxy. DF2 and DF4, having similar baryonic mass, are expected to have similar values of $\bar{\nu}$. Therefore, for the global analysis, we treat $\bar{\nu}$ as a single parameter optimized for both galaxies. The individual likelihood analysis for both DF2 and DF4 evaluates $\bar{\nu}$ to be 0.30×10^{-8} and 0.10×10^{-8} as can be referred from Table 3.1. Additionally, $\bar{\nu}$ is also constrained from the global likelihood for both UDGs and is found to be 0.16×10^{-8}. As both the UDGs have low mass in comparison to typical galaxies, the estimated $\bar{\nu}$ is at least one order smaller than the previous analysis of spiral galaxies where $\bar{\nu}$ lies in the range $10^{-6} - 10^{-8}$ [193]. This small value of $\bar{\nu}$ parameter is correlated with the UDG mass, which is much smaller than a typical spiral or elliptical galaxy [190, 193].

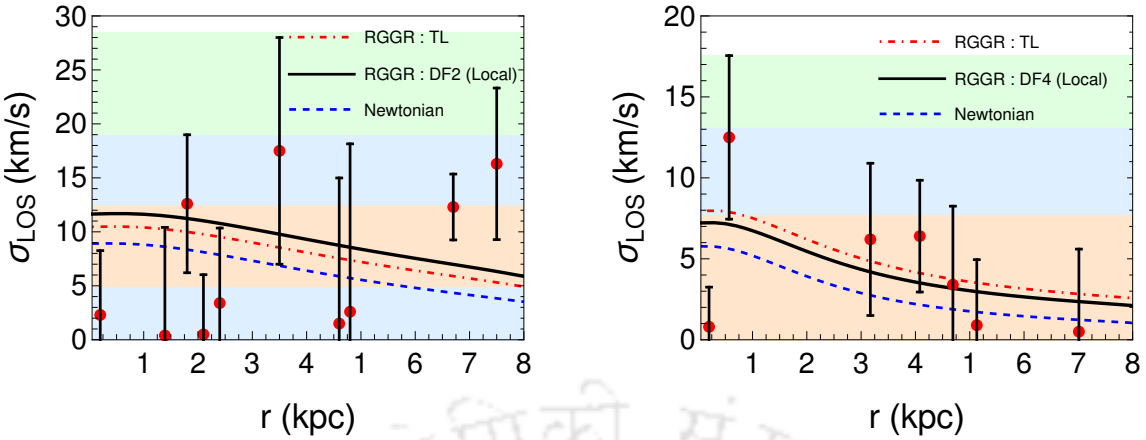

Figure 3.4: Comparison of the Newtonian radial variation of VD (blue dashed curve) for both the UDGs with the RGGR gravity. Radial VDs for the RGGR model are shown by solid black lines when both galaxies, i.e., DF2 (left) and DF4 (right), are treated independently. The VDs for the global analysis from total likelihood (TL) for both the UDGs are shown using the red dot-dashed lines. Other information about the Newtonian contribution and observations in the plots remain the same as in Fig.3.1

The line of sight VDs for the likelihood fitting is also represented in Fig.3.4. Similar to the previous figures, the DF2 and DF4 cases are shown in the left and right panels, respectively. In both panels, the VDs for the local individual likelihood results are shown by solid black lines. Similarly, the red dot-dashed line shows the LOS velocity dispersion curves for the global scenario. The solid blue lines represent the LOS VD contribution from Newtonian gravity.

As seen from Fig.3.4, the RGGR gravity contributions from both analyses lie within the 1σ region of the observations (orange area). The fact that the underlying alternative gravity model of RGGR can explain the dynamical behavior of the UDGs remains true for both the global and local analysis.

3.5 Summary

The DM-deficit nature of UDGs such as DF2 and DF4 paves the path to probe the kinematics for modified gravity models. The kinematics of these UDGs can be explained with normal stel-

lar matter without invoking the need for DM. In this chapter, we probe the line of sight VD for such galaxies for two alternative gravity models, i.e., $f(R)$ gravity (a chosen $f(R)$ form and a general case) and RGGR gravity. The likelihood analysis has estimated the free parameters of the gravity models. While constraining the model parameters from both UDGs, we treat certain parameters as global ones and find the fit from both galaxies. The case of $f(R)$ gravity is studied from two perspectives. The first model chooses a functional form $f(R)$ and adds a Yukawa-like term to the Newtonian potential. The second choice takes an effective power law form for the $f(R)$, resulting in a radius-dependent power term ($\propto r^{\beta}$) to the Newtonian potential. Studying the DF2 and DF4 galaxies for the two $f(R)$ scenarios shows that the best fit VD curve lies within the 1σ region of the observation. Similarly, for the RGGR model, a potential-dependent term is added to the Newtonian gravity. The free parameter of this model increases in a nearly linear manner with the mass of the galaxy. Hence, the free parameter ($\bar{v}$) for the two UDGs having almost similar mass is in the same order. The optimized VD fitted with the free parameters also lies within the 1σ range of observations. Thus, all the alternative gravity models in this discussion are found to be reasonable while explaining the VD data.

In summary, the observed luminous content within both UDGs is sufficient to understand the kinematics. Thus, GR without DM is consistent with the observed VD for the two galaxies. However, when the UDGs are examined in light of the chosen alternative gravity models, the observed VD is consistent with the alternative gravity choices. The two versatile UDGs i.e., DM-dominant (DF44) and DM-deficit (DF2 & DF4) provides one galactic regime to test MOGs. However, the test of an alternative model must be consistent with different galactic regimes. Therefore, in the next two chapters, we study a rather large collection of rotationally supported galaxies. Such an analysis not only helps to test the gravity model for a large sample size but also helps determine the behavior of the model parameters with different kinds of morphologies present in the Universe.

Chapter 4

Probing RGGR with SPARC galaxies

4.1 Introduction

The present chapter discusses the phenomenology of RGGR based on the RC of the SPARC galaxies. RGGR is another choice of alternative gravity model that proposes RG running of the gravitational constant (G) with the energy scale [60, 61, 185] to explain the galactic kinematics. The logarithmic running formalism considered here, in the weak-field limit, introduces an extra $\bar{\nu}$ dependent component to the Newtonian potential (see Sec.4 for more detail). Studies on the kinematics of spiral and elliptical galaxies show that the $\bar{\nu}$ is of the order of 10^{-7} [190, 193, 233]. The parameter $\bar{\nu}$, which determines the strength of the running, is found to have an almost linear relation with the baryonic mass of the galaxy and has been studied for a number of galaxies [193]. In the following, we analyze the RGGR model with an even larger selection of galactic rotation curve (RC) from the SPARC [120] datasets. In this regard, we, based on the galaxy morphological types, investigate the dynamics of a diverse collection of galaxies.

The selection criteria on the SPARC data related to the quality of observational data and the inclination of the galaxies are discussed in Sec.1.1.2 of Chapter1. Additionally, we impose a χ^2 cutoff to ensure that our analysis of the RGGR model shows a consistent fit with the observations, which further reduces the number of relevant galaxies. For each galaxy, we constrain the RGGR parameter $\bar{\nu}$ from the observed RC data. The linear dependence of the parameter $\bar{\nu}$ for a wide range of masses in SPARC galaxies $(10^8 - 10^{11}\ M_\odot)$ is also determined in our analysis. The model parameters of the individual galaxies are statistically constrained using an Markov Chain Monte Carlo (MCMC) algorithm based on the Bayesian technique [200]. The consistency of RGGR is also reported by measuring the χ^2 of individual galaxies.

We extend the phenomenology of the RGGR model further to the well-known empirical relations, the RAR, and the BTFR (see Sec.1.1.2 for a detailed discussion). As both the relations were evaluated from the observational data, having no model dependence, such relations became a consistency check for the gravity model used. RAR [94] hints towards modified kinematics that govern the motion on galactic scales. The other relation, BTFR [143, 234] signifies that the baryonic mass contained within all the galaxies present in the SPARC catalog has a power-law dependence on the flat part of the circular velocity (V_f) far from the galactic center. Using the best-fit values obtained from the RC analysis with the emcee sampler, we verify the above two relations of the SPARC catalog for RGGR.

Similar to the RGGR analysis, we also look into the SPARC galaxies with an alternative DM scenario. In the DM paradigm, the net matter density of a galaxy, in addition to baryonic matter, has a contribution from DM [235]. In particular, we consider the NFW density profile [36] for the DM modeling. Here, similar to the RGGR analysis, we constrain the DM model parameter (M_{200}) using the Bayesian MCMC algorithm [200]. Furthermore, we compare the fit of the RC for the two profiles, i.e., RGGR and DM, by evaluating the Bayesian Inference Criteria (BIC) [201] and check which model id favored compared to the other. It is important to stress that in order to treat the two different models, viz. the RGGR and NFW, on the same footing, we place the same reduced χ^2 cutoff that was chosen for RGGR. This same cutoff criteria for both models, in turn, provides us with 93 galaxies out of 153 in the SPARC catalog to work with. Such an elaborate analysis aims to check the consistency and credibility of the RGGR model for a rather large selection of rotationally supported galaxies to date in comparison to an alternative

DM (NFW) scenario.

The layout of the chapter is as follows. Section 4.2 gives a brief account of the RGGR model. The next Section 4.3 discusses the galaxy catalog SPARC adopted for studying the alternative gravity model. The methodology and the computational packages used to sample the parameter space of the model are discussed in Section 4.4. The following Section 4.5 mentions the results obtained for our study.

4.2 Models: RGGR and NFW

RGGR

RGGR is a quantum gravity model based on the concept of variation of the gravitational coupling parameter (G) with the energy scale of the Universe [61, 89, 192]. As discussed in detail in Sec.1.2.4, our analysis looks into the logarithmic variation of the G with the energy scale of the Universe $\left(G(\mu) = \frac{G_0}{1+\nu \ln\left(\frac{\mu^2}{\mu_0^2}\right)} \right)$. Additionally, to formulate a consistent theory with an observational basis, it is required to correlate the energy scale with some observable parameter (see Sec.1.2.4 for more details). The solution for the circular velocity and acceleration in the weak-field limit gives [89, 190]

$$v^2_{\rm RGGR}(r) = v^2_{\rm bar}(r)\left(1 - \frac{c^2\bar{\nu}}{\phi_{\rm N}(r)}\right),$$

$$a_{\rm RGGR}(r) \approx a_{\rm bar}(r)\left(1 - \frac{c^2\bar{\nu}}{\phi_{\rm N}(r)}\right), \tag{4.1}$$

where $v_{\rm bar}(r)$ and $a_{\rm bar}(r)$ are the Newtonian contribution to the velocity and acceleration, respectively, and c is the speed of light. The analysis of galactic dynamics with RGGR [190, 193] suggests that the parameter $\nu\alpha \equiv \bar{\nu}$ follows a close to linear relation with the baryonic mass

of the galaxy. For the galactic scales, the net circular velocity and acceleration of an object, in addition to the Newtonian (baryonic) part, have the extra contribution due to the modified gravity. This extra contribution depends on the model parameter $\bar{\nu}$ and the potential $\phi_{\rm N}(r)$. The potential $\phi_{\rm N}(r)$ arises from all the baryonic contents of the galaxy and is crucial to evaluate the effect of RGGR gravity. This requires mass modeling, i.e., modeling the radial dependence of the baryonic mass of the galaxy. In general, the baryonic structure of the galaxy is composed of three components, i.e., disk, gas, and bulge. We assume a radial exponential profile [133] for the disk and gas component. For the galaxies having bulge, the mass modeling assumes a spheroidal Hernquist profile [134]. Thus, one may estimate or constrain the phenomenological parameter $\bar{\nu}$ from observations for the given mass profiles.

In what follows, we analyze the consistency of the RGGR model for a large selection of galaxies from the SPARC catalog. These galaxies belong to different morphologies with different characteristics, which gives a measure of the model parameter's variation over the nature of the galaxies.

NFW model

We also compare the RGGR model with an alternative scenario where we assume that the presence of DM can resolve the missing mass problem on the astrophysical scales. For this, we look into a known DM profile, i.e., Navarro-Frenk-White (NFW) [36] (see Sec.1.2.2 for details). It has already been shown [193] that a comparison of the RGGR model with the alternative gravity model MOND [74] or NFW DM model [36] shows a better or an equally consistent fit for the observed circular velocity of the spiral galaxies. Along the same line, in this work, we compare the RGGR model with an NFW DM profile for the SPARC galaxies and check their favourability. Our analysis for RGGR versus DM looks into a scenario where the number of free parameters of the model is similar. Thus, in contrast to the two-parameter fit for the DM profile [193], we fit a single DM model parameter (M_{200}) by using a stellar-halo relation ($c - M_{200}$) [196] (see Sec.1.2.4 for a detail discussion). The velocity contribution from

the assumed NFW profile is [36]

$$v^2_{\rm NFW}(r) = \frac{4\pi G r_s^3 \rho_s}{r}\left[-\frac{r}{r+r_s} + \log\left(1+\frac{r}{r_s}\right)\right].$$

Here, ρ_s and r_s are the characteristic density and radius, respectively. Both the density parameters can be expressed in terms of concentration (c) parameter and virial mass (M_{200}) as explained in detail in Sec.1.2.2. For the DM halo scenario, the contribution to the net circular velocity for a galaxy comes from the sum of the baryonic component (v_N), which for SPARC is expressed as the sum of stellar and gaseous component and NFW profile (v_{NFW}), i.e.,

$$v^2_{\rm tot}(r) = v^2_{\rm bar}(r) + v^2_{\rm NFW}(r), \tag{4.2}$$

The free parameter for NFW (M_{200}), in addition to mass model parameters ($\gamma_{\rm d}$ $\gamma_{\rm b}$), are constrained from the observational circular velocity. Thus, our analysis aims to draw a comparison of the RGGR model with an NFW DM halo that helps to determine the favorability of the gravity model over a DM scenario.

4.3 SPARC catalog

To test the gravity model against the observational data, we look into a collection of galaxies from the SPARC catalog, also discussed in Sec.1.1.2. In addition to the net circular velocity for a galaxy, the catalog compiles the radial velocity for the baryonic (disk, gas, and bulge). Given the velocity for individual baryonic components of a galaxy, the total Newtonian contribution can be written as

$$v^2_{\rm bar}(r) = \gamma_{\rm d}\, v^2_{\rm disk}(r) + \gamma_{\rm b} v^2_{\rm bulge}(r) + |v_{\rm gas}(r)|\, v_{\rm gas}(r);$$

where $v_{\rm disk}(r)$, $v_{\rm bulge}(r)$ and $v_{\rm gas}(r)$ represent the disk, bulge, and gas velocity components for a particular galaxy in the SPARC catalog. The two baryonic components are scaled by a factor $\gamma_{\rm d}$ and $\gamma_{\rm b}$, which measure the mass-to-light ratio for the disk and bulge part, respectively. Un-

der the assumption that the gravity on the galactic scale is RGGR, the modified kinematics of objects within the galaxy have an additional contribution dependent on the potential energy and a mass-dependent parameter.

Therefore, comparing the total observed circular velocity $v_{\rm obs}$ from the SPARC catalog with the RGGR velocity form (v_{RGGR}) helps to check the consistency of the gravity model. This requires the variation of the model parameter of the theory within the allowed parameter space. This analysis aims to look for the parameters that consistently fit the observed RC of the galaxy sample. The best-fit values obtained in the analysis are also used to construct the empirical relation RAR and BTFR.

RAR compares the baryonic (a_{bar}) and observational (a_{obs}) acceleration of the 153 eligible SPARC galaxies, showing a trend in the data that follows the relation

$$a_{\rm obs}(R) = \frac{a_{\rm bar}(R)}{1-\exp(-\sqrt{a_{\rm bar}(R)/a_*})},$$

where a_* is the acceleration scale parameter and has best-fit value $a_* = 1.2\times10^{-10}$ ms^{-2}. The consistency of the RGGR net acceleration ($a_{\rm RGGR}$) with respect to the $a_{\rm obs}(R)$ can be probed by the RAR. In particular, the analytical expression for the net acceleration (Eq.4.1) in RGGR includes a $\bar{\nu}$ dependent extra component to the Newtonian part. The best-fit value of the $\bar{\nu}$ parameter for each galaxy can be estimated from the circular velocity fitting with the SPARC data. In the following, we compare the observed RAR with the empirical relation in the context of the RGGR model for each data point of the qualifying SPARC galaxies.

Another alternative empirical relation shown by SPARC data is BTFR. The relation states that the baryonic mass has a relation with the velocity measured at the flat part of the RC. BTFR states that $M_{bar} = A\ V_{\rm f}^x$ with $A,\ x$ to be constrained as 50 M$_\odot$km^{-4}s^4 and 4, respectively [95]. For the RGGR model, the total circular velocity is estimated by $v_{\rm RGGR}$ and is dependent on the free parameters ($\gamma_{\rm d}$, $\gamma_{\rm b}$, $\bar{\nu}$) which are constrained using the observed RC of the galaxy. Thus, the $V_{\rm f}$ for the RGGR will also get modified. The relation between the $M_{\rm bar}$ and the RGGR predicted flat velocity for each qualifying SPARC galaxy should follow observed BTFR. This additional check for RGGR is crucial for the gravity model to remain phenomenologically consistent.

4.4 Methodology

For the RGGR model, we constrain the model parameters by comparing the modified velocity with the observed circular velocity of the chosen SPARC galaxies. The free parameters for the model are constrained using the publicly available *emcee* package [200] in PYTHON. This package works on the Markov Chain Monte Carlo (MCMC) principle and samples the posterior distribution of the free model parameters (see Sec.1.3 for a detailed explanation).

Assuming that the errors on the observed circular velocity follow a Gaussian distribution, the likelihood for each galaxy is defined as in Eq.1.3. To define the likelihood, we require $v_{obs}(r)$ and $\sigma_{err}(r)$, which represent the total circular velocity and error as compiled within the SPARC catalog. The analytical velocity $v_{tot}(r, \vec{\theta})$, which represents the total circular velocity for an alternative gravity scenario computed at a certain radius for a given set of free parameters, is model-dependent. We fit both the RGGR and the NFW DM models. The net circular velocities for RGGR (v_{RGGR}) and NFW (v_{NFW}) are expressed in terms of their respective free parameters. These free parameters in velocity $v_{\rm tot}(r, \vec{\theta})$ are phenomenologically constrained by comparing with the observational circular velocity. For both the models, i.e., RGGR and NFW, the normalization mass-to-light factors (γ) introduced for the baryonic components, i.e., the disk ($\gamma_{\rm d}$) and the bulge ($\gamma_{\rm b}$) of the galaxy, are common. Additionally, the RGGR model has a mass-dependent phenomenological parameter $\bar{\nu}$. Similarly, the NFW model has a singular free parameter M_{200}. Thus, in the alternative gravity scenario $\vec{\theta}$ is composed of $\{\gamma_{\rm d}, \gamma_{\rm b}, \bar{\nu}\}$ which are to be estimated independently for each galaxy. For the case of NFW $\vec{\theta}$ is made up of $\{\gamma_{\rm d}, \gamma_{\rm b}, M_{200}\}$ and are again constrained for each galaxy.

Regarding the priors $\pi(\vec{\theta})$, we assume both flat and Gaussian priors for the model parameters. In the case of the flat priors, the mass-to-light ratio for both disk ($\gamma_{\rm d}$) and bulge ($\gamma_{\rm b}$) are assumed to have no radial dependence on the galaxy and are varied in the range [0.3, 0.8] [83, 198, 199]. In the case of RGGR, for the mass-dependent parameter $\bar{\nu}$, a wide range of parameter space is looked into and is varied within $10^{-9} \leq \bar{\nu} \leq 10^{-6}$. This range is motivated by the previous analysis of spiral and elliptical galaxies where $\bar{\nu}$ is found to vary in order of 10^{-7} [193]. For the DM scenario, the NFW parameter M_{200} is bound to lie within the range $10^9 < M_{200}/M_{\odot} < 10^{14}$

[83]. For the Gaussian priors, the parameters γ_d and γ_b are considered to have a mean value of 0.5 and a standard deviation of 0.1. The mean and standard deviation for $\log(\bar{\nu}/10^{-7})$ and $\log(M_{200}/M_{\odot})$ are taken to be $(-0.3,\ 0.1)$ and $(10.69,\ 0.1)$, respectively. To ensure the convergence of the chain, we run the sampler for a sufficient number of steps such that the acceptance fraction lies within the range $0.2-0.5$ [200]. Additionally, by estimating the autocorrelation time (τ) for each galaxy, we discard τ number of steps as burn-in before performing posterior analysis. To achieve convergence, we run a sufficient number of steps, i.e., 50 τ as specified in *emcee* [200].

Additionally, to quantify the preference of one model over the other, we consider the Bayesian Information Criteria (BIC) [201]. Here, the number of parameters for a model is same, i.e., we have 3 parameters, for both the RGGR and NFW models considered here. To compare the two models, i.e., RGGR and NFW, we evaluate,

$$\Delta BIC = BIC_{NFW} - BIC_{RGGR}. \tag{4.3}$$

The measure of ΔBIC, if less than 2, implies inconclusive preference between the two models. Similarly, the value of ΔBIC that is between $2-6$ implies a positive inclination towards RGGR. Values of ΔBIC greater than 6 are considered to have a strong inclination toward the RGGR model.

In addition to the selection criteria discussed in Sec.1.1.2 ($Q > 2$ & $i < 30^{\circ}$), which leaves 153 SPARC galaxies, we assume galaxies with data points greater than 4 for a well-defined $\chi^2_{\rm red}$. Additionally, to ensure that we have a consistent RC fit with the RGGR as well as with NFW, we reject galaxies whose goodness of fit with the gravity model, i.e., $\chi^2_{\rm red} \geq 6$. The cut-off for the goodness of fit keeps the galaxies with various numerical issues fitting out of the analysis for both models. Two notable issues are difficulty in modeling the gas contribution due to extreme radial variation and poor quality of data, such as a discontinuity in data points in certain radii. This selection criteria for the cutoff makes sure that we are liberal enough to accommodate a larger set of SPARC galaxies in our analysis. Thus, after imposing the above criteria on the 153 galaxies, we are left with 93 eligible ones.

4.5 Results

In the following, we analyze the consistency of the RGGR framework with the observational circular velocity for our selection of SPARC galaxies. We also compare the RGGR model with the NFW DM scenario. The RC analysis is done for galaxies belonging to different morphological types. The free model parameters are constrained using the emcee sampler, which scans the parameter space to evaluate the best-fit values. For this, we look into the rotation curves of individual galaxies present within SPARC. We also study the mass-dependent nature of the phenomenological parameter $\bar{\nu}$. These best-fit values must also satisfy the fundamental relationships between RAR and BTFR. Hence, we compare our results for the RGGR model with both these relationships. For galaxies consistent with the RGGR model, we alternatively look into their kinematics in a DM-dominated case. We employ a similar Bayesian technique to constrain the model parameter M_{200} for the NFW profile. To measure the favorability of the RGGR model over the DM NFW profile, we also report the ΔBIC value evaluated for each galaxy.

4.5.1 RC analysis

Fitting the RC of each SPARC galaxy with the RGGR gravity model helps to constrain the free parameters. It includes two mass modeling parameters defined for the baryonic component of a galaxy, i.e., γ_d and γ_b. The additional model parameter, i.e., $\bar{\nu}$, comes from the choice of RGGR gravity and has been found to have an almost linear dependence on the luminous mass of the galaxy. We analyze the behavior of the phenomenological parameter $\bar{\nu}$ with the baryonic mass for the large sample of SPARC galaxies. In particular, we study the consistency of the RGGR-governed model for all four morphological types of the galaxies present in SPARC. This compares the phenomenological consistency of the RGGR gravity for all the different galaxy types. A similar RC analysis where galaxies are assumed to be DM-dominated instead of modified gravity with the radial density profile having the NFW form is also looked into. For this scenario, in addition to the mass model parameters γ_d and γ_b, we fit M_{200}, which comes from the choice of NFW halo.

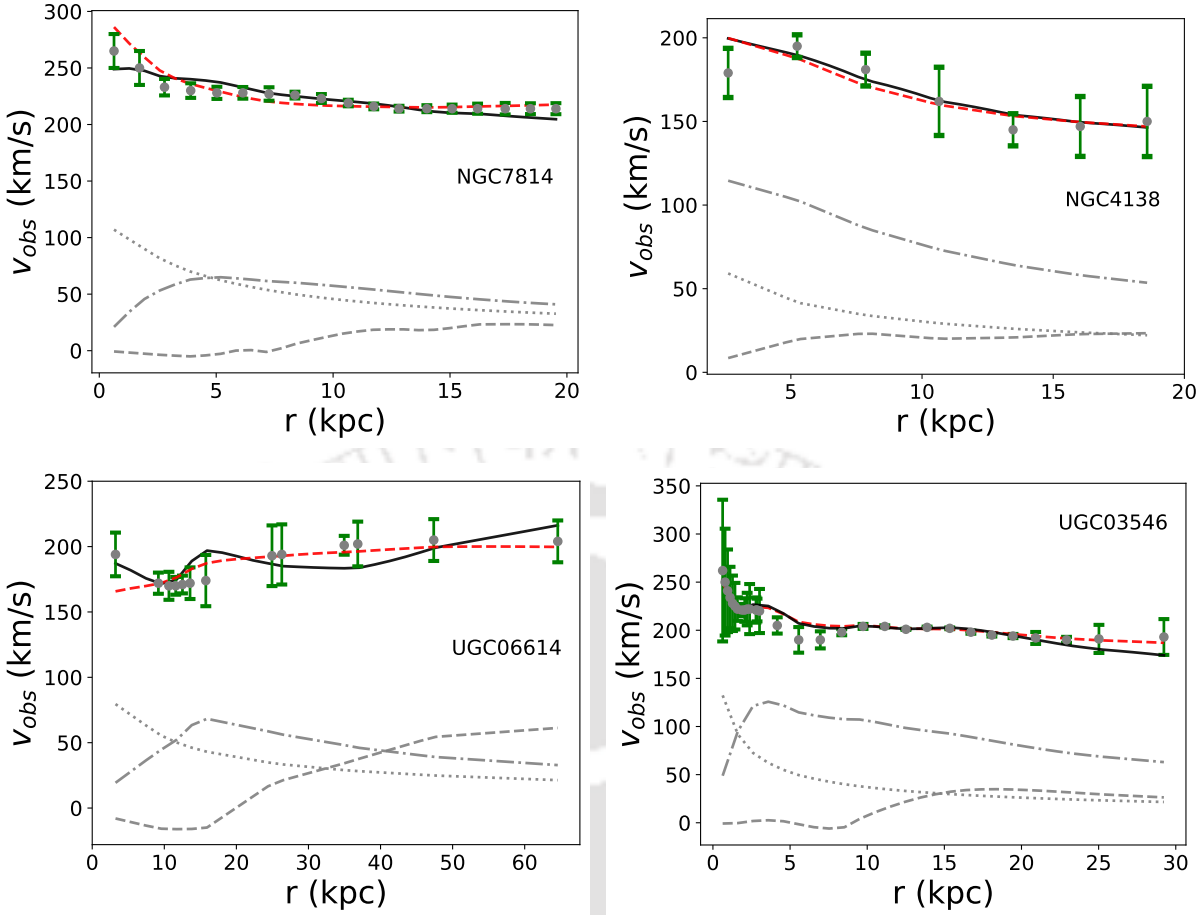

Figure 4.1: For Early-type galaxies, the RC for 4 specimen galaxies are shown in the four panels above. The black solid line is the circular velocity when RGGR gravity contributes in addition to the baryonic part. The black dots with green error bars are the circular velocity data obtained from SPARC [120]. The red dashed line is where the net velocity contribution is evaluated in an NFW paradigm. The dashed grey line represents the gaseous component of the galaxy. The dot-dashed line shows the variation of disk velocity within the galaxy, and the bulge part is plotted via the dotted line.

Early-type galaxies

The first category belongs to the early-type galaxies, which can be identified from a bulge at the center and tight, indistinguishable spiral arms in the outer parts of the disk. From the whole set of early-type, we analyze 8 galaxies that satisfy the selection criteria. Out of these 8 galaxies, we illustrate the RC fitting for 4 of them in Fig.4.1. This includes NGC7814 shown in the upper left panel, NGC4138 in the upper right, UGC06614 in the lower left, and UGC03546 in the lower right panel of Fig.4.1. For each galaxy shown, the grey dots with green error bars repre-

sent the observational total circular velocity traced by the *HI* component within the galaxy. We also plot the individual baryonic components, i.e., disk, bulge, and gas, for each galaxy using the gray lines. The dashed gray line represents the radial variation of the gas velocity. The disk and bulge components of the galaxy scaled by their respective mass-to-light ratio are shown via. the dashed-dotted and dotted lines, respectively.

In particular, the first panel at the top left shows the RC for NGC7814. Under the assumption of flat priors, the constraints on the free parameters (γ_d, γ_b and $\bar{\nu} \times 10^7$) obtained from our analysis give 0.53, 0.31 and 7.23, respectively. However, when the priors are considered Gaussian, we see almost no change in the best-fit value. As an example, for the case of NGC7814, when priors are assumed to be Gaussian (γ_d, γ_b and $\bar{\nu} \times 10^7$) are found to be 0.53, 0.28 and 7.53 respectively. The radial variation of the circular velocity (Eq.1.27) in the RGGR model with these best-fit parameters is plotted using a solid black line. The obtained value of $\chi^2_{\rm red}$ for the galaxy is 1.18, indicating a good fit to the observational data of NGC7814.

A similar RC analysis of the 8 early-type galaxies in the presence of DM with the NFW profile is also looked into. The statistical analysis to constrain the model parameters of the DM halo gives the best-fit values evaluated in the case of flat-priors for γ_d, γ_b, and $M_{200} \times 10^{11} M_\odot$ as 0.79, 0.66 and 24.13, respectively. However, contrary to the case of RGGR, we observe that the constrained values of the model parameters differ between the flat and Gaussian prior cases. In particular, for the Gaussian prior case, the γ_d is not rigorously contained in the preferred range of $0.3 - 0.8$ as the Gaussian distribution allows values outside this range. Hence, we consider the flat prior results over the Gaussian ones. In Fig.4.1 for each galaxy, the radial variation of the circular velocity in the DM model obtained by substituting the best-fit value is shown via the red dashed line. Similarly, the obtained parameters and goodness of fit for the other early-type galaxies in the panel for both RGGR and NFW model can be found in Table.4.1. The measured goodness of fit for the early-type galaxies is compiled in Table.4.1 points to a positive inclination towards the RGGR scenario.

Spiral-type galaxies

The second class of galaxies mentioned in SPARC belongs to the Spiral type. Such galaxies are characterized by the presence of distinct spiral structures at the outer parts of the disk. Addition-

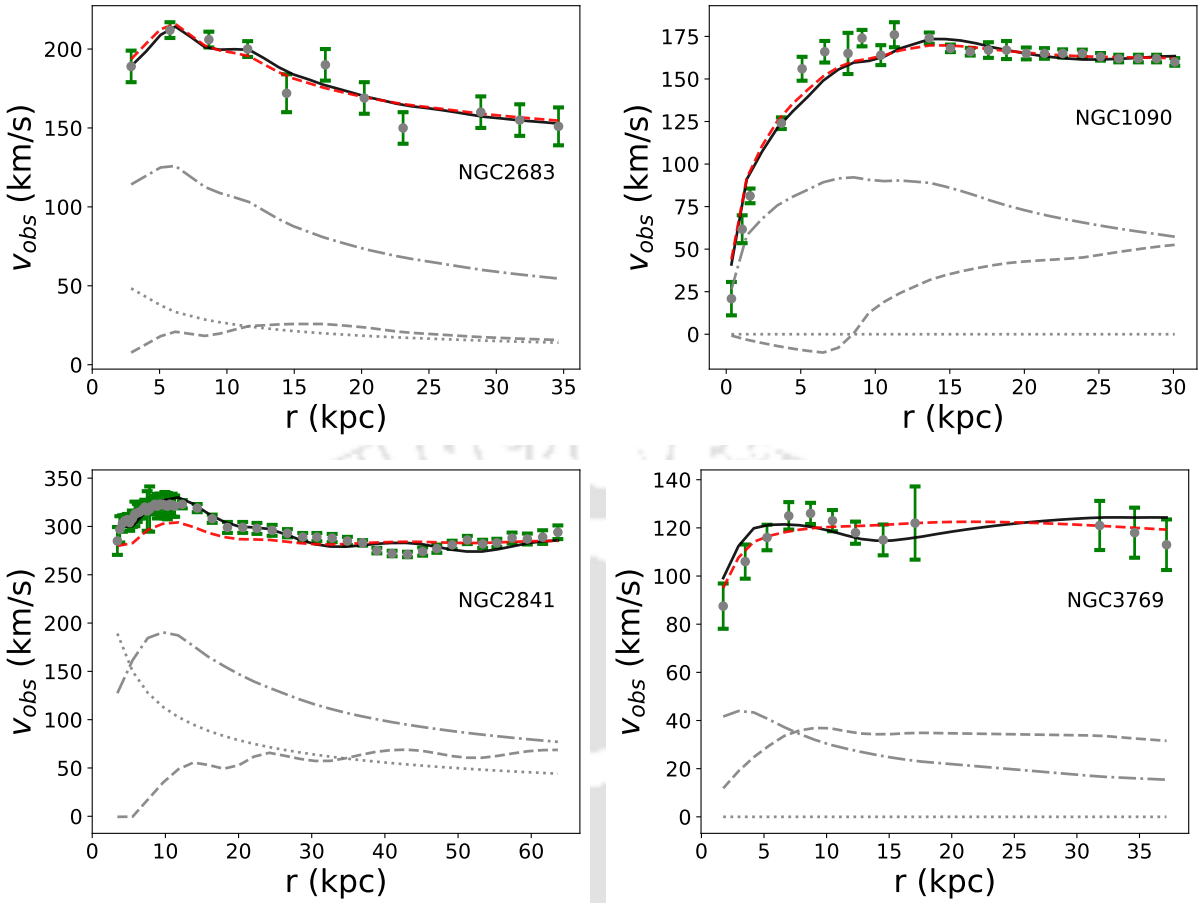

Figure 4.2: For Spiral-type galaxies, the RC for 4 specimen galaxies are shown in the panel. The black solid line is the circular velocity when RGGR gravity contributes in addition to the baryonic part. The red dashed line is the case where the net velocity contribution is evaluated in an NFW paradigm. The black dots with green error bars are the circular velocity data obtained from SPARC [120]. The dashed grey line represents the gaseous component of the galaxy. The dot-dashed line shows the variation of disk velocity within the galaxy, and the bulge part is plotted via the dotted line.

ally, the bulge at the center is of comparatively smaller size. SPARC has a large collection of spiral galaxies, and our selection criteria give us 41 such galaxies. Similar to Fig.4.1 we show 4 representative galaxies i.e., NGC2683, NGC1090, NGC2841 and NGC3769 in Fig.4.2. Out of the 4 galaxies shown, only two have a visible bulge component present and are represented by a dotted gray line in the plot. The gray points with error bars represent the total circular velocity observed in SPARC. Similarly, the gray lines represent the individual baryonic components in a galaxy.

The best-fit parameters for the first subplot for NGC2683 are shown at the top left panel in Fig.4.2. For the RGGR model, when priors are assumed to be flat, the best values come out to be $\gamma_d = 0.56$, $\gamma_b = 0.54$ and $\bar{\nu} \times 10^7 = 1.88$ with χ^2_{red} equal to 0.69. Similar to the case of early-type galaxies, the choice of priors yields little difference in the best-fit values evaluated. In the case of NGC2683, Gaussian priors results in $\gamma_d = 0.58$, $\gamma_b = 0.50$, $\bar{\nu} \times 10^7 = 1.82$ with χ^2_{red} equal to 0.71. For the obtained parameters, the net contribution to the total circular velocity, which is the sum of baryonic and RGGR components, is shown by a solid black line. The goodness of fits evaluated for each galaxy as given in the Table.4.1 show that the RGGR model is a consistent choice in explaining the observed circular velocity of the spiral SPARC galaxies. Similar to early-type, RC analysis of the 41 spiral galaxies in the presence of DM with the NFW profile is also looked into. The best-fit value for γ_d, γ_b, and $M_{200} \times 10^{11} M_\odot$ evaluated in the case of flat-priors for circular velocity with NFW halo results in $(0.7, 0.36, 4.18)$ with χ^2_{red} equals 0.84. However, similar to the case of early-type, we consider the flat prior results out of the two choices of priors. The radial variation of circular velocity in the NFW DM model obtained by substituting the best-fit value is shown via a red dashed line for all the 4 galaxies in Fig.4.2.

Late-type dwarf

The third category of galaxies belongs to late-type dwarf, where the bulge is too faint to be observed. Thus, the baryonic component of the galaxy mostly constitutes disk and gas only. From the total late-type dwarf galaxies in the catalog, 29 galaxies fulfill the selection criteria. Similar to the above two categories, we plot four late-type dwarf galaxies in Fig.4.3. The galaxies that are illustrated include NGC4010 (top-left), NGC0300 (top-right), UGC04278 (bottom-left), and UGC05721 (bottom-right). The details on the plot corresponding to the observed circular velocity of a galaxy and its baryonic components follow the same convention as mentioned in the discussion of the previous two types of galaxies.

The circular velocity in the RGGR framework can be obtained by substituting the best-fit values of the model parameters, i.e., (γ_d, γ_b, $\bar{\nu} \times 10^7$) as given in Table.4.1 in Eq.1.27. This radial variation is shown using the solid black line in Fig.4.2. Similar to the above two morphological types, we observe a little variation in the choice of priors. In Table.4.1, we report the result for the flat priors. Similarly, we also analyze the 34 late-type galaxies in the NFW framework. The

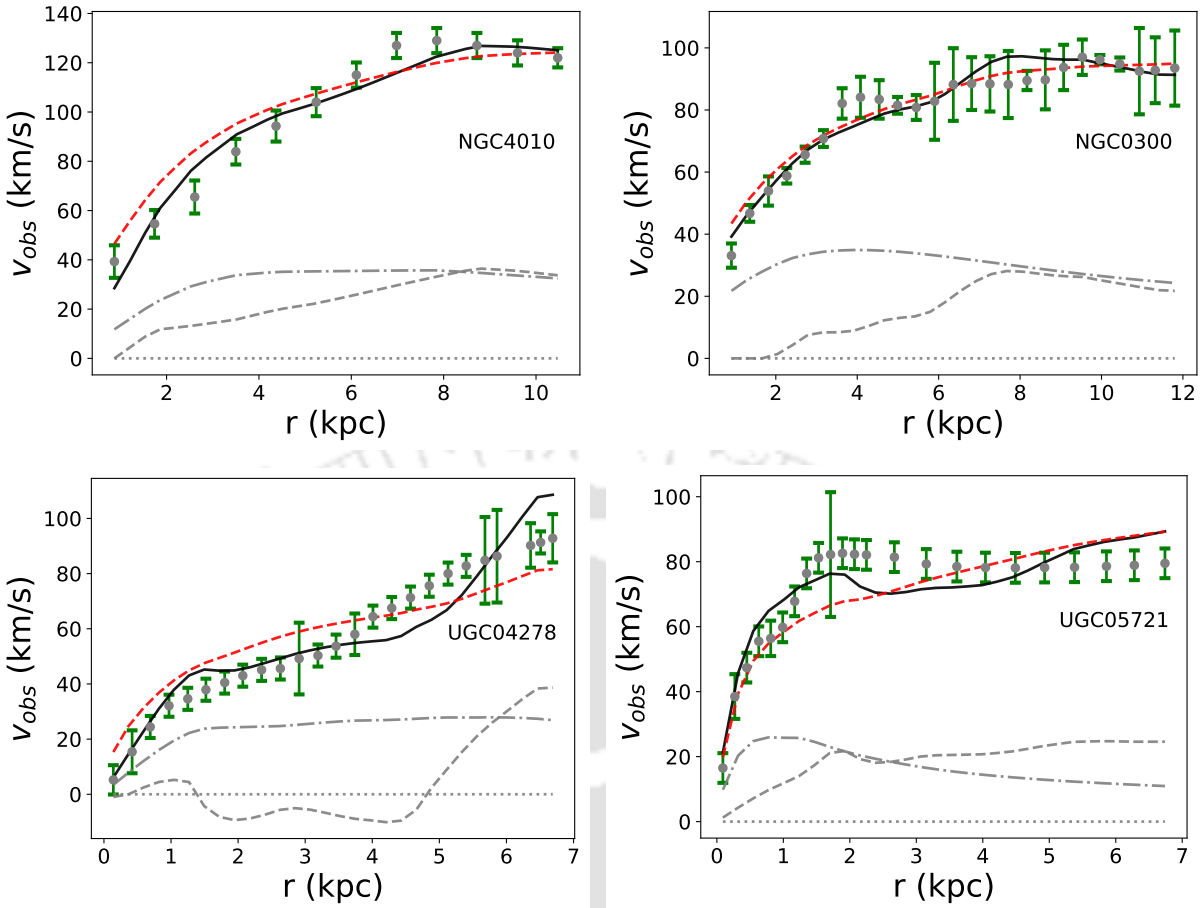

Figure 4.3: For Late-type galaxies, the RC for 4 specimen galaxies are shown in the panel. The black solid line is the circular velocity when RGGR gravity contributes in addition to the baryonic part. The red dashed line is where the net velocity contribution is evaluated in an NFW paradigm. The black dots with green error bars are the circular velocity data obtained from SPARC [120]. The dashed grey line represents the gaseous component of the galaxy. The dot-dashed line shows the variation of disk velocity within the galaxy, and the bulge part is plotted via the dotted line.

best-fit parameters obtained show preference towards the flat choice of priors and are reported along with the RGGR model in Table.4.1. The $\chi^2_{\rm red}$ computed in Table.4.1 for all the galaxies shows that the late-type dwarfs fit well with the RGGR model. This consistent behavior can also be visualized from the four sample plots shown in Fig.4.3.

Starburst galaxy

The fourth morphological type belongs to starburst galaxies, which are relatively young and

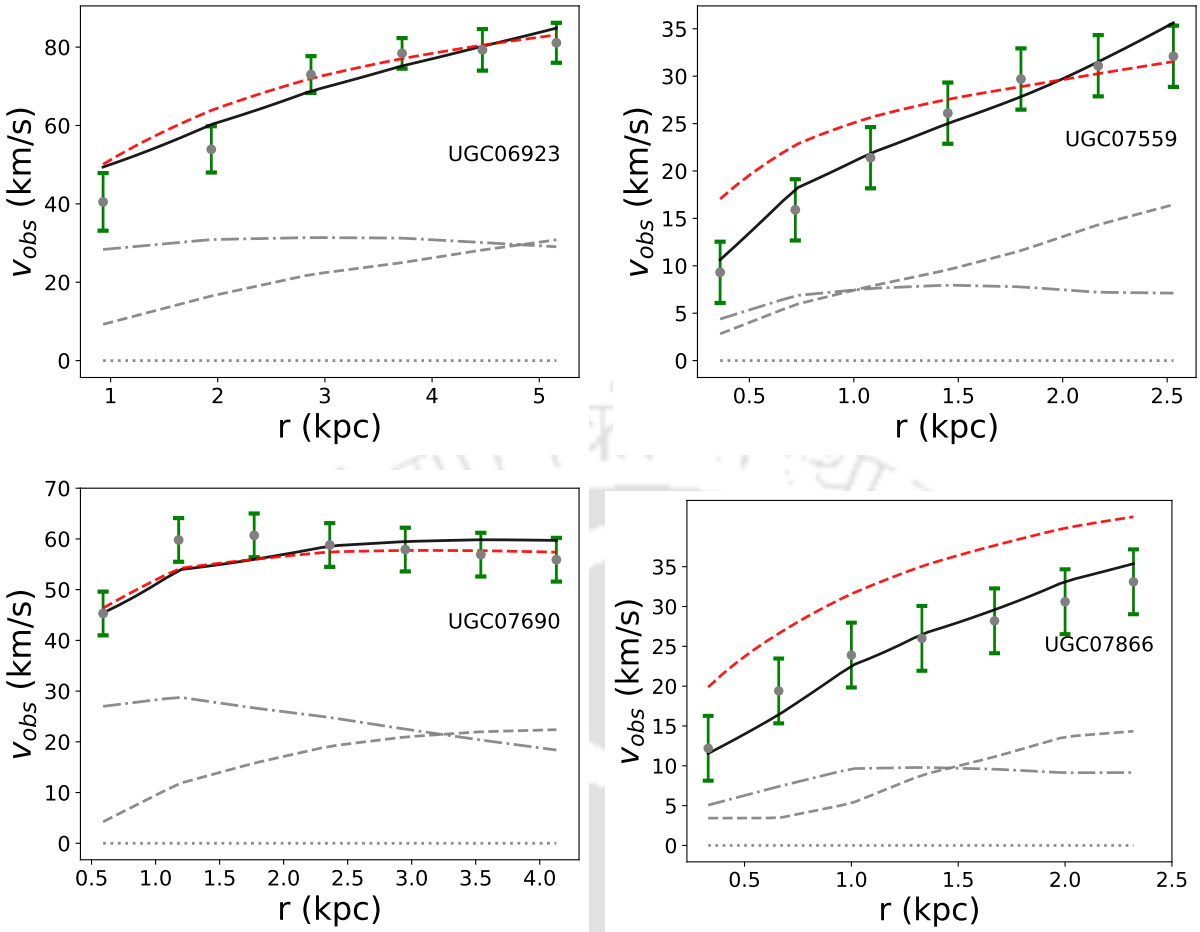

Figure 4.4: For Starburst galaxies, the RC for 4 specimen galaxies are shown in the panel. The black solid line is the circular velocity when RGGR gravity contributes in addition to the baryonic part. The red dashed line is where the net velocity contribution is evaluated in an NFW paradigm. The black dots with green error bars are the circular velocity data obtained from SPARC [120]. The dashed grey line represents the gaseous component of the galaxy. The dot-dashed line shows the variation of disk velocity within the galaxy, and the bulge part is plotted via the dotted line.

have a high star formation rate. Such galaxies are dominated by gas and thus make a versatile region to look for the signature of the alternative gravity model. The morphology of such systems shows a diffused structure with no visible bulge and spiral arms. We studied 15 galaxies belonging to this particular morphological type and found that RGGR can give consistent fits with the observed circular velocities. As an illustration following the convention used in other morphological types, we plot 4 starburst galaxies, i.e., UGC06923, UGC07559, UGC07690, and UGC07866 in Fig.4.4. The baryonic contribution for these galaxies comes from the gas

and disk component only, as starbursts have no visible bulge within. This is represented in the above plot by gray lines following the same convention used in preceding cases. Also, the net observed circular velocity with error bars is shown using gray points.

As mentioned in the previous three morphological types, for the RGGR model, we see a

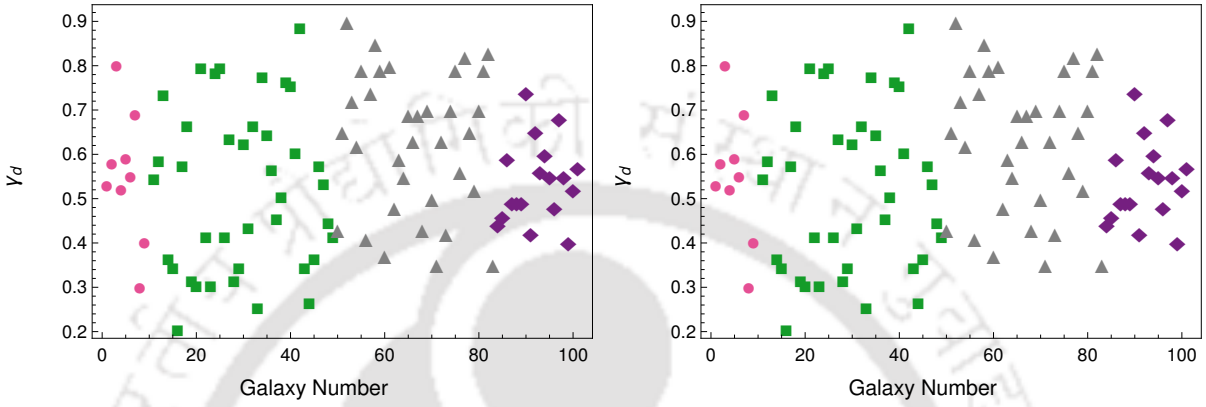

Figure 4.5: The plot shows the variation of γ_d. The left panel represents the γ_d obtained for the RGGR analysis, and the right panel belongs to the case of NFW. The varying morphological types are represented using different markers. The square markers represent the early type, and the circles are for the spiral galaxies. Additionally, γ_d for late-type and starburst are shown via triangle and diamond markers.

little variation in our two choices of priors, i.e., flat and Gaussian. The constrained free parameters (γ_d, γ_b, $\bar{\nu} \times 10^7$) obtained for the aforementioned galaxies in reference to the flat priors can be referred from Table.4.1. From the obtained values of parameters, the total circular velocity evaluated for each galaxy is shown by a solid black line in Fig.4.4. As can be seen from the plots, the observational circular velocity fits well with the analytical velocity in all 4 cases. Similarly, this consistent nature of the gravity model can also be quantified for all the starburst galaxies from the goodness of fit as mentioned in Table.4.1. We also studied the 18 starburst galaxies concerning the NFW model for both flat and Gaussian priors and considered the flat prior results in preference to the Gaussian ones. The best-fit values along with the χ^2_{red} for flat-priors are compiled in Table.4.1. For the four different morphological types of galaxies discussed above, we find that RGGR is a phenomenologically consistent theory of gravity. The best fit values for the $\bar{\nu}$ parameter lies in the range $10^{-6} - 10^{-8}$. The parameters γ_d and γ_b fall in the range $0.3 - 0.8$, consistent with the choices of our priors. We also observe from Table.4.1

that the values of $\bar{\nu}$ are larger (in the range close to 10^{-6}) for the early-type galaxies compared to the other types. Interestingly, the $\bar{\nu}$ values decrease as we go across the Hubble type towards the late-type galaxies with $\bar{\nu}$ around 10^{-8}. This relation between the parameter $\bar{\nu}$ and the galaxy type can be understood from the baryonic mass content of the galaxies and is discussed in the next subsection.

Note that, for many starburst galaxies, the rotation curves at the outer radius do not flatten but keep increasing. The starburst galaxies, in general, have a major baryonic component in the form of large amounts of gas. This gas is also dispersed throughout the galaxy and, hence, is not easy to model. The increase of the rotation curve at the outer radius could be due to the shortcomings of the gas modeling.

To summarise the comparison between the RGGR and the DM NFW scenario, we study 93 galaxies that satisfy our selection criteria, as discussed previously. To measure the evidence against or in favor of our choice of models (NFW or RGGR), we compute ΔBIC for each galaxy. The plot, which measures the number of galaxies belonging to different bin sizes of ΔBIC favoring either RGGR or NFW, is shown in Fig.4.6. It clearly shows that out of 93 galaxies, 38 favors the RGGR model, and the result is inconclusive for 16 galaxies. However, the remaining 39 galaxies prefer the choice of DM profile. This conclusion remains qualitatively the same with different cutoffs on $\chi^2_{\rm red}$, viz. $\chi^2_{\rm red} \leq 5$ and $\chi^2_{\rm red} \leq 7$ as our galaxy selection criterion. This indicates that the RGGR model remains competitive with NFW in explaining the kinematics of SPARC galaxies with different selection criteria, too. The mass modeling parameters constrained for each galaxy in our analysis include $\gamma_{\rm d}$ and $\gamma_{\rm b}$, which are assumed to be a constant having no radial dependence. The bulge component is prominent and can be majorly seen only in the early-type galaxies. Therefore, we utilize the disk normalization factor to show the variation of $\gamma_{\rm d}$ for the galaxies of different morphological types. The plot containing the values of $\gamma_{\rm d}$ for the 93 galaxies present in our analysis is shown in Fig.4.5. For RGGR (left panel), the behavior of $\gamma_{\rm d}$ represents that this parameter varies throughout the range of $[0.3, 0.8]$ for all galaxies. Also, in the NFW regime, we observe that $\gamma_{\rm d}$ varies throughout the range for spiral and late-type galaxies. However, for early-type galaxies, $\gamma_{\rm d}$ is concentrated towards the higher end of the prior range. Also, in the case of Starburst, we observe that $\gamma_{\rm d}$ is pointing

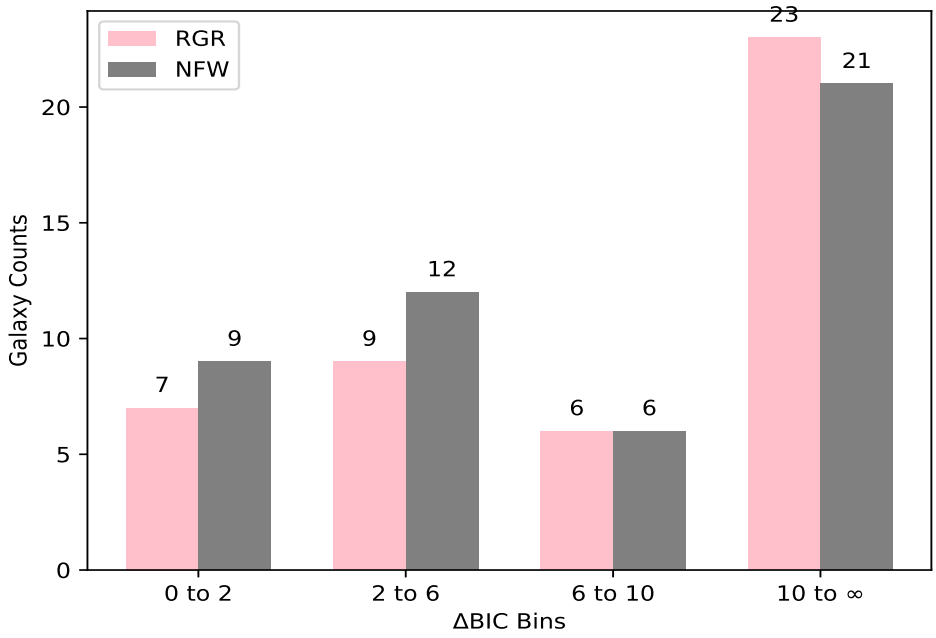

Figure 4.6: The plot represents the ΔBIC comparing RGGR with NFW. The pink histograms show the frequency of galaxies that favor RGGR over the DM model over different bin sizes. For ΔBIC range within $0-2$, the claim over a preference of a model is inconclusive. In total, we observe that RGGR is favored by the majority of galaxies when compared with NFW.

toward the lower end of the range. The different markers on the plot in Fig.4.5 belong to the different morphological types of galaxies in SPARC. The pink points give the value of γ_d for early-type galaxies. Similarly, green squares, grey triangles, and violet diamond shapes represent γ_d for the spiral, late-type, and starburst galaxies. Additionally, looking into the behavior of $\bar{\nu}$ in Table.4.1 shows that as we go from early type to starburst galaxies, the magnitude of the phenomenological parameter decreases. Such behavior of $\bar{\nu}$ with the stellar mass of galaxies is studied in detail in the next subsection.

4.5.2 Relation of $\bar{\nu}$ with baryonic matter

To investigate the RGGR model parameter dependence on the baryonic mass, we rely on the same galaxies from the SPARC catalog. The baryonic mass of a rotationally supported galaxy consists of the bulge, disk, and gas components, as mentioned earlier. Each component of the

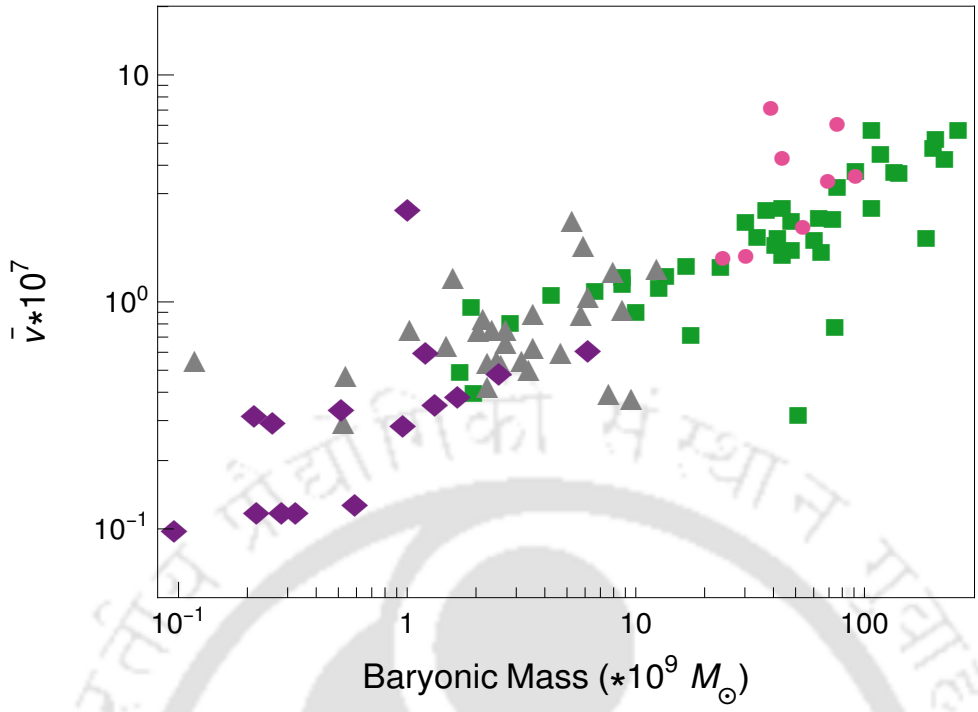

Figure 4.7: The plot relates the phenomenological parameter $\bar{\nu}$ with the baryonic mass of the galaxy. The individual points represent the $\bar{\nu}$ evaluated for each galaxy studied in SPARC. The almost linear relation shown in the plot affirms the previous mass dependence claim for the RGGR parameter. The different markers in the plot show the different morphological types of galaxies, with the circle representing early-type, a square belonging to spiral, a triangle showing late-type dwarfs, and a diamond for starburst galaxies.

galaxy (stellar+gas) is assumed to follow a distinct density distribution. The radial variation of matter distribution for disk and gas is assumed to vary exponentially [120, 133]. Similarly, for the galaxies having bulges, the density variation can be fitted with the Hernquist profile [134]. The total baryonic content for a galaxy is a linear mass sum of stellar and gas components. The galaxies in SPARC constitute a wide range of masses varying from $10^8 - 10^{11}\ M_\odot$ [120].

For the scenario where the underlying gravity is assumed to be RGGR, the velocity contribution is the sum of the Newtonian part plus an additional term dependent on a free parameter ($\bar{\nu}$). This phenomenological parameter varies independently for each galaxy and is constrained from the study of RC, as discussed in the previous section. A comparison of the constrained $\bar{\nu}$ obtained along with the stellar mass of the galaxy is represented via an individual datapoint in Fig.4.7. The figure shows that the magnitude of the phenomenological parameter $\bar{\nu}$ increases

almost linearly with the increasing mass of the galaxies. Our analysis is thus justified with the previous study [193] done for the same gravity model. Different representations are used in the plot to categorize galaxies belonging to various morphological types. The pink round pointers belong to the early type, and the green square shows the spiral, the gray triangle is for the late type, and the purple diamond represents the starburst galaxies. The figure shows that the baryonic mass decreases from early to late-type galaxies. Accordingly, the value of $\bar{\nu}$ reduces linearly: a feature which can also be seen from the data provided in Table.4.1, i.e. $\bar{\nu}$ is smaller for the relatively younger galaxies. Such a linear relation of the model parameter with the mass of the system points towards the non-fundamental behavior of the RGGR model. However, as can be seen from the analysis of RC, the gravity model is consistent with the observations on astrophysical scales.

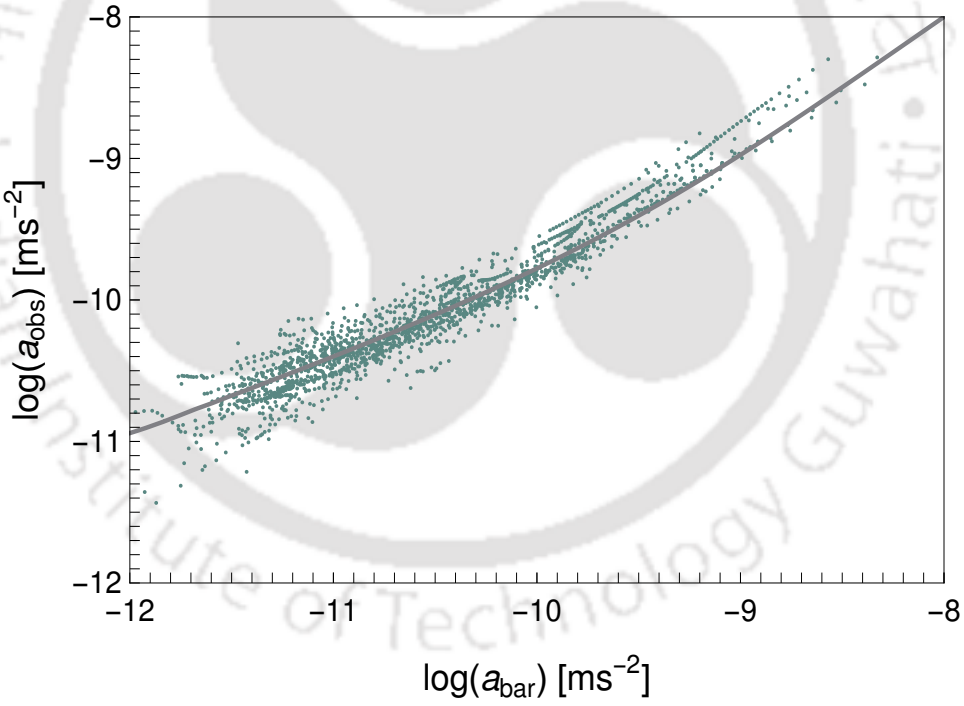

Figure 4.8: The plot compares the RAR relation where the total observed acceleration is evaluated in the RGGR framework. The black solid line shows the empirical relation Eq.(1.5) obtained from the SPARC observations. The green scatter points refer to the individual data points of all the galaxies analyzed where the net contribution to the acceleration gets modified.

4.5.3 Empirical relations for SPARC (RAR and BTFR)

Radial Acceleration Relation (RAR)

The data points of the SPARC galaxies projecting the relation between the observed Eq.1.6 and baryonic acceleration Eq.1.7 is shown to follow an empirical relation as mentioned in Eq.1.5. This shows that in weak-gravity regions, the observed and baryonic acceleration follows the relation $a_{obs} \propto \sqrt{a_{bar}}$ and depends linearly in high acceleration scales as is expressed by the empirical relation. Thus, if RGGR is a consistent gravity model, it must satisfy RAR for the SPARC galaxies. This relation has been looked into and verified for a large sample of galaxies present in the SPARC catalog without any prior assumptions for the DM or alternative gravity model. In the alternative gravity scenario, total circular velocity and acceleration are modified according to Eq.1.27 and Eq.4.1, respectively. The net acceleration is the sum of contribution coming from different baryonic components of a galaxy ($a_{bar}(r)$) with an additional part dependent on $\phi_N(r)$ and $\bar{\nu}$ as expressed in Eq.4.1. In our analysis, we compare the modified acceleration (a_{RGGR}) with a_{bar} to study the behavior of RAR in an alternative gravity framework.

The evaluation of the empirical relation requires the knowledge of free parameters, which is taken from the RC analysis in Sec.4.5.1. The RAR behavior determined for the individual datapoint of all the selected galaxies in the RGGR framework is shown in Fig.4.8. The gray solid line is the analytical relation fitted from the observational data and has the form as given in Eq.4.1. Also, for each galaxy in our analysis, we determine the baryonic acceleration ($a_{bar}(r)$) at every radial point specified in the SAPRC catalog. Similarly, we also compute the RGGR acceleration ($a_{RGGR}(r)$) at every radial point. Thus, each green dot on the plot refers to the RGGR and baryonic acceleration at a specific radius for a given galaxy. The collection of points in Fig.4.8 contains the contribution for all the 93 galaxies selected in our analysis.

Residual computed from comparing the relation with the 1817 data points, as illustrated in the figure, turns out to be 0.31 dex. Thus, based on the best-fit parameters from the RC analysis, RAR behaves satisfactorily in the context of the RGGR model.

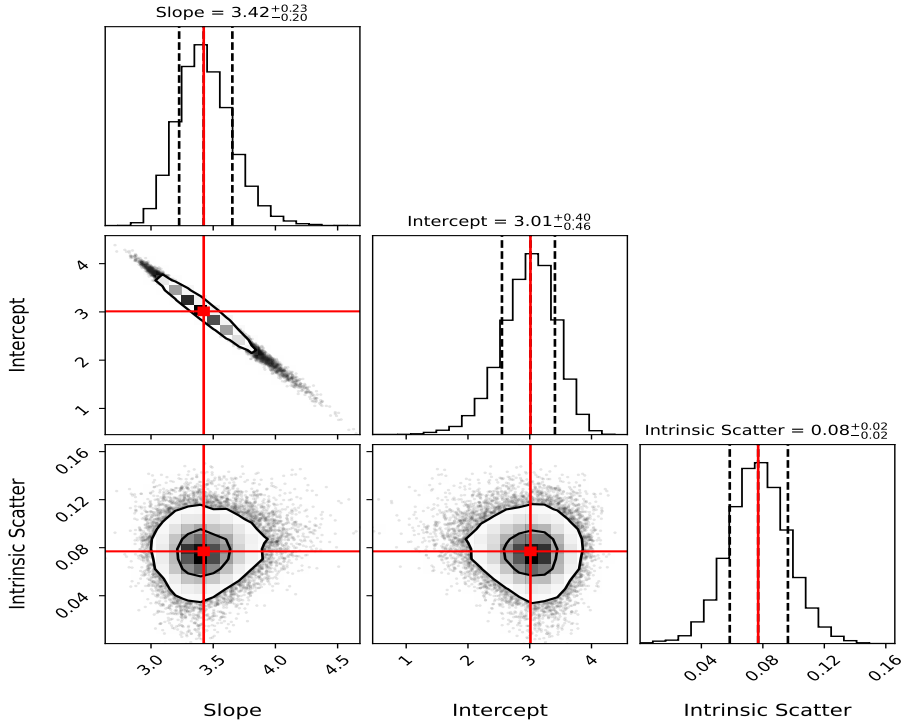

Figure 4.9: The posterior distribution of the parameter space in BTFR Eq.4.4 evaluated using BayesLineFit [143].

Baryonic Tully Fisher Relation (BTFR)

SPARC galaxies are also found to follow the BTFR (Eq.1.8), which provides a power law relation between the baryonic mass and the velocity measured at the flat part of the rotation curve. This relation holds irrespective of the gravity model. Therefore, for RGGR to be a consistent choice as an alternative gravity model, BTFR must be satisfied by the RGGR-predicted dynamics for the SPARC galaxies. To probe the BTFR,

$$\log(M_{bar}) = x\log(V_f) + \log A, \tag{4.4}$$

we consider the V_f corresponding to the RC fit with RGGR for each galaxy. The flat velocity (V_f) for each galaxy in the RGGR framework can be evaluated from the fit of the RC (Sec. 4.5.1) at a given radius. The baryonic mass M_{bar} for a galaxy is a sum of stellar and gas components. The velocities of these different components are connected to their respective mass profile. For a given mass profile, M_{bar} can be estimated, particularly for the SPARC galaxies, where the bulge and disk are assumed to have spheroidal and exponential distribution respectively [120].

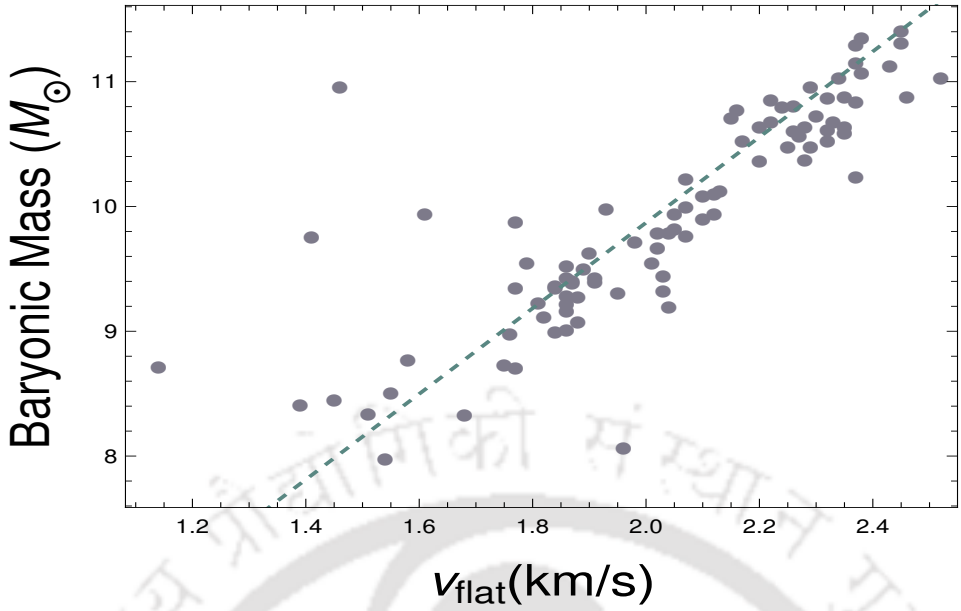

Figure 4.10: The BTFR with the flat circular velocity evaluated in the RGGR model. The above plot estimates V_f for the RGGR model at 3.2 R_d. The gray data points are the measure of flat velocity evaluated for individual galaxies. The green solid line shows the analytical best fit, consistent with the observed V_f in the RGGR framework.

BTFR has also been found to be sensitive on the radial choice [143] at which V_f is measured for SPARC galaxies. We evaluate the relation at 3.2 R_d, which has shown an optimal behavior to the relation. The choice of 3.2 R_d [143, 236] ensures that 80% of the stellar matter is encompassed within the radius. Almost for all the SPARC galaxies we select, the distance of 3.2 R_d from the center of the galaxy corresponds to the flat region of the RC. We use BayesLineFit package [143], which is based on *emcee* algorithm to find (x, log$A$). The best-fit value obtained for the parameters (x, log$A$) is found to be ($3.42^{+0.23}_{-0.20}$, $3.01^{0.40}_{-0.46}$) with an orthogonal scatter of $0.08^{0.02}_{-0.02}$ dex. We also report the vertical scatter given by [143]:

$$\sigma_0 = \sqrt{\frac{1}{n}\sum^{n}[\log(M_{bar}) - x\log(V_f) - \log A]^2}, \tag{4.5}$$

where n is the number of galaxies selected in our analysis, the observed σ_0 for the case of 3.2 R_d comes out to be 0.56. The posterior distribution for the fitting parameters, i.e., slope (x), intercept (log A), and intrinsic scatter, are shown in Fig.4.9. The solid red lines in the plot point towards the maximum likelihood values for the parameters. Given the best-fit parameters, BTFR for all the galaxies included in our analysis is illustrated in Fig.4.10. The solid gray

circles represent the flat velocity for each SPARC galaxy evaluated at $r = 3.2\ R_d$. Additionally, the green solid line fits the linear equation Eq.4.4 for the best-fit parameters obtained in our analysis. The BTFR plot in Fig.4.10 shows that the flat velocity evaluated at $3.2\ R_d$ consistently matches the observational results.

4.6 Summary

The chapter focuses on probing the kinematics of rotationally supported galaxies in the RGGR framework. Here, we study the dependence of the alternative gravity parameter on the galaxy morphology. We have looked into four different morphological types of galaxies, viz. early, spiral, late, and starburst. We have constrained the model parameter $\bar{\nu}$ for each galaxy taken from all four morphological types and have found that the RGGR consistently fits the observed net circular velocity. Our statistical analysis has probed this consistency for the individual galaxies using the goodness of fit. We have also checked the linear dependence of the model parameter $\bar{\nu}$ on the baryonic mass of the galaxy. The constrained values for the parameter $\bar{\nu}$ for our sample of the SPARC galaxies lie in the range $10^{-6} - 10^{-8}$ and are consistent with the variation of the masses of the galaxies under consideration. This implies that the older and heavier galaxies lead to a larger $\bar{\nu}$. Indeed, we have found that the parameter $\bar{\nu}$ decreases from the older galaxies to the younger ones. Note that the allowed range of $\bar{\nu}$ found in our analysis is consistent with the previous studies. For example, studies on spiral and elliptical galaxies found $\bar{\nu}$ in the range of 10^{-7}, consistent with the baryonic mass content of the galaxies studied in [190, 191, 193]. On the other hand, the solar system [192], and UDG constraints [194] are found to be much smaller ($\bar{\nu} \sim 10^{-17}$) than the standard galactic RC estimates due to considerably smaller baryonic mass contents in these two systems.

We have further verified our goodness of fit from the RC analysis in light of the well-known empirical relations: RAR and BTFR. In particular, the RAR compares the radial variation of the observed and the baryonic acceleration. An additional factor comes in the baryonic acceleration due to the RGGR model. Our analysis has found that the RAR in the RGGR framework aligns with the established analytical relation obtained from previous observations. On a similar note, BTFR compares the baryonic mass with the observed flat velocity ($V_{\rm f}$) of a galaxy,

suggesting a power-law dependence between them. The exact power-law index is sensitive to the choice of the flat velocity radius. Our analysis finds a tight correlation of the baryonic mass with flat velocity measured at $3.2R_d$ and has obtained a small orthogonal scatter of 0.08. Additionally, we compare the RGGR model with a DM scenario, where we assume the profile to be NFW. Our analysis clearly shows that leaving aside where both the models perform equally well ($\Delta BIC = 0-2$), NFW and RGGR models behave consistently for almost similar numbers of galaxies.

In summary, the objective of the current chapter is to explain the observed kinematics for a large set of galaxies using RGGR. Contrary to RGGR, where the model parameter varies for the choice of galaxy, there are models involving global parameters. These models are dependent on certain parameters that are expected to be global on the galactic scales. In particular, we probe one such model, i.e., YMOG, which involves a mixed scenario incorporating both DM and Yukawa-like corrections to understand the kinematics of SPARC galaxies.

Table 4.1: The best-fit parameters obtained from the emcee sampler. Corresponding to the RGGR gravity model, for every galaxy, 3 parameters (γ_d, γ_b, $\bar{\nu}$) are statistically constrained from the observed circular velocity. Column 2 of the table denotes the galaxy morphology types, abbreviated as E: Early, S: Spiral, L: Late-type, and SB: Starburst. In the table, the representation for the free parameter $\bar{\nu^*} = \bar{\nu} \times 10^{-7}$ and $M^*_{200} = M_{200} \times 10^{11} M_\odot$.

Galaxy	**Type**	γ_d		γ_b		$\bar{\nu}^*$	M^*_{200}	χ^2_{red}	
Name		γ_d (RGGR)	γ_d (NFW)	γ_b (RGGR)	γ_b (NFW)			χ^2_{red} (RGGR)	χ^2_{red} (NFW)
NGC7814	E	0.53	0.79	0.31	0.66	7.23	24.13	1.18	1.12
NGC4138	E	0.58	0.79	0.5	0.31	1.58	3.32	0.56	0.7
UGC06614	E	0.52	0.31	0.32	0.31	3.6	12.89	1	0.54
UGC03546	E	0.59	0.65	0.34	0.37	2.15	8.93	0.9	0.87
UGC03205	E	0.55	0.72	0.8	0.8	3.42	10.61	4.82	4.13
UGC08699	E	0.69	0.78	0.51	0.67	1.61	7.81	1.4	0.64
UGC11914	E	0.3	0.63	0.74	0.8	6.11	100	1.68	4.31
UGC06786	E	0.39	0.8	0.55	0.75	4.33	26.14	2.28	2.2
NGC1090	S	0.54	0.47	0.55	0.5	1.65	4.88	2.85	2.2
NGC2683	S	0.56	0.7	0.54	0.36	1.88	4.18	0.69	0.84
NGC2841	S	0.78	0.8	0.79	0.8	5.61	40.6	1.86	6.08
NGC3769	S	0.33	0.36	0.54	0.5	1.41	2.61	0.91	0.56
NGC2955	S	0.32	0.31	0.56	0.73	4.69	23.23	4.89	3.25
NGC4013	S	0.3	0.42	0.37	0.76	2.53	7.33	2.38	1.35
NGC3198	S	0.54	0.55	-	-	1.86	4.57	1.37	3.98
NGC5005	S	0.46	0.5	0.35	0.49	3.68	38.39	0.13	0.05
NGC6195	S	0.31	0.31	0.56	0.64	4.16	15.27	2.17	2.21
NGC7331	S	0.3	0.36	0.36	0.36	3.61	20.07	2	0.75
UGC12506	S	0.79	0.79	-	-	4.4	19.69	3.74	1.58
UGC11455	S	0.41	0.4	-	-	5.09	31.32	4.16	5.51
UGC09037	S	0.3	0.3	-	-	1.83	3.09	3.18	5.81
UGC07151	S	0.78	0.65	-	-	0.39	0.43	2.39	2.23
UGC06983	S	0.79	0.73	-	-	1.09	1.96	2.42	0.58
NGC4559	S	0.41	0.33	-	-	0.7	2.31	1.02	0.22
NGC4100	S	0.63	0.72	-	-	1.89	5.09	2.11	1.16
NGC4088	S	0.31	0.31	-	-	1.62	4.86	1.1	0.5
NGC4085	S	0.32	0.31	0.54	0.53	1.13	7.28	3.05	3.51
NGC3972	S	0.68	0.33	-	-	1.26	7.95	2.01	0.99
NGC3893	S	0.38	0.5	-	-	2.48	11.6	0.53	1
NGC2998	S	0.67	0.59	-	-	2.53	9.86	2.47	2.11
NGC0100	S	0.32	0.32	-	-	1.05	0.9	0.63	2.3

Continued from the previous page

Galaxy	Type	γ_d		γ_b		$\bar{\nu}^*$	M^*_{200}	χ^2_{red}	
Name		γ_d (RGGR)	γ_d (NFW)	γ_b (RGGR)	γ_b (NFW)			χ^2_{red} (RGGR)	χ^2_{red} (NFW)
ESO079*	S	0.77	0.32	-	-	2.21	14.22	3.85	4.46
NGC0289	S	0.65	0.54	-	-	2.27	6.46	1.89	1.78
NGC2976	S	0.54	0.76	-	-	0.93	0.02	0.5	1.68
NGC3521	S	0.44	0.51	-	-	2.22	17.03	0.76	0.29
NGC3949	S	0.39	0.39	-	-	1.39	14.01	0.52	0.19
NGC3953	S	0.75	0.69	-	-	0.76	2.11	0.55	0.34
NGC3992	S	0.76	0.78	-	-	3.65	14.08	1.87	0.63
NGC4051	S	0.64	0.48	-	-	0.31	1.67	1.3	0.62
NGC4183	S	0.79	0.68	-	-	0.88	1.39	1.61	0.16
NGC4157	S	0.33	0.39	0.5	0.42	2.29	7.93	0.57	0.44
NGC0891	S	0.3	0.35	0.33	0.5	3.13	25.01	5.67	5.33
UGC02885	S	0.56	0.45	0.77	0.79	5.59	38.97	0.93	1.54
F583-4	S	0.61	0.4	-	-	0.48	0.32	0.23	0.69
NGC6946	S	0.44	0.47	0.46	0.5	1.74	5.62	1.5	1.5
NGC6503	S	0.41	0.54	-	-	1.17	2.3	5.98	2.57
NGC3917	S	0.78	0.56	-	-	1.27	3.31	2.73	4.33
NGC3726	S	0.4	0.34	-	-	1.57	4.73	2.69	2.37
NGC0024	S	0.79	0.79	-	-	1.05	2.69	1.79	2.11
NGC4010	L	0.36	0.32	-	-	1.42	3.51	1.44	2.67
NGC0300	L	0.69	0.32	-	-	0.74	1.48	0.76	0.97
UGC04278	L	0.79	0.33	-	-	0.75	0.7	3.46	3.82
UGC05721	L	0.76	0.78	-	-	0.71	1.73	2.26	3.31
NGC7793	L	0.64	0.57	-	-	0.53	1.24	0.64	0.84
UGC06446	L	0.79	0.73	-	-	0.77	0.94	4.34	0.35
UGC07603	L	0.37	0.4	-	-	0.48	0.7	0.61	1.23
UGC06930	L	0.77	0.54	-	-	0.84	1.45	1.54	0.23
UGC08550	L	0.79	0.67	-	-	0.3	0.27	3.87	0.55
UGC12732	L	0.79	0.35	-	-	0.89	0.9	5.93	0.67
UGC11557	L	0.35	0.35	-	-	0.38	0.15	0.84	2.3
UGC08490	L	0.78	0.79	-	-	0.61	0.87	0.54	1.39
UGC07089	L	0.45	0.36	-	-	0.51	0.26	0.13	2.63
UGC07261	L	0.68	0.63	-	-	0.59	0.57	0.92	0.12
UGC07323	L	0.6	0.35	-	-	0.56	0.57	0.21	2.86
UGC07399	L	0.75	0.76	-	-	1.21	7.96	2.64	3.01

Continued from the previous page

Galaxy	Type	γ_d		γ_b		$\bar{\nu}^*$	M^*_{200}	χ^2_{red}	
Name		γ_d (RGGR)	γ_d (NFW)	γ_b (RGGR)	γ_b (NFW)			χ^2_{red} (RGGR)	χ^2_{red} (NFW)
UGC06399	L	0.73	0.38	-	-	0.71	1.12	0.51	0.94
UGC06917	L	0.75	0.35	-	-	0.94	2.51	1.63	0.61
UGC05986	L	0.39	0.54	-	-	1.79	4.8	1.02	5.1
UGC04499	L	0.76	0.34	-	-	0.39	0.44	1.89	1.39
ESO116*	L	0.66	0.42	-	-	0.9	3.26	1.88	2.21
F568-V1	L	0.75	0.65	-	-	1.18	6.02	1.98	0.57
F571-V1	L	0.77	0.53	-	-	2.12	0.61	2.39	0.86
F574-1	L	0.67	0.49	-	-	0.54	1.49	0.41	1.67
UGC05750	L	0.78	0.61	-	-	1.21	0.15	3.61	3.05
UGC10310	L	0.75	0.63	-	-	0.53	0.33	1.05	0.49
UGC07524	L	0.76	0.38	-	-	0.5	0.51	2.03	2.62
UGC07125	L	0.79	0.34	-	-	0.64	0.18	5.69	3.17
UGC06818	L	0.79	0.34	-	-	0.33	0.23	2.88	5.69
UGC06923	SB	0.48	0.38	-	-	0.49	0.97	0.77	0.82
UGC07559	SB	0.46	0.39	-	-	0.12	0.02	0.3	1.61
UGC07690	SB	0.71	0.71	-	-	0.25	0.17	0.38	0.46
UGC07866	SB	0.56	0.38	-	-	0.12	0.11	0.21	4.09
UGC05414	SB	0.5	0.37	-	-	0.36	0.19	0.08	4.45
UGC05829	SB	0.77	0.44	-	-	0.37	0.16	2.14	1.32
NGC4068	SB	0.41	0.39	-	-	0.12	0.02	0.23	3.41
NGC3741	SB	0.73	0.37	-	-	0.3	0.11	2.62	4.72
ESO444*	SB	0.66	0.44	-	-	0.32	0.75	1.08	0.68
UGC05918	SB	0.72	0.37	-	-	0.32	0.09	1.65	0.46
F565-V2	SB	0.66	0.44	-	-	0.61	0.68	0.9	1.23
UGC09992	SB	0.56	0.46	-	-	0.13	0.03	0.56	0.22
NGC2915	SB	0.74	0.37	-	-	2.96	1.36	2.03	1.09
UGC05005	SB	0.62	0.41	-	-	0.62	0.69	0.19	2.42
UGCA444	SB	0.7	0.44	-	-	0.1	0.03	0.81	0.77

Chapter 5

Probing modified gravity with Yukawa-like potential from SPARC galaxies

5.1 Introduction

In the present chapter, we look into a phenomenological model, namely, Yukawa Modified Gravity (YMOG). The motivation for the gravity model comes from the work done in [83, 154, 161], which suggests that a solution to the modified Poisson equation introduces a Yukawa-like correction to the Newtonian potential. Such a Yukawa-like nature is vastly found in many alternative gravity models, such as the $f(R)$ gravity model, STVG model, and Horndeski gravity model. The weak-field potential for the gravity model is dependent on the coupling (β) and scale (λ) parameter that is constrained from the observations.

Such a gravity model has been extensively studied in the literature with and without DM. For

the present analysis, we aim to probe the consistency of the YMOG model for a large collection of galaxies present in SPARC. For this, we constrain the model parameters β and λ globally for a group of galaxies selected based on their morphological type, i.e., early, spiral, and late-type. The motivation for such a division is to inspect the dependence of the model parameters (β, λ) with the acceleration (mass) scale of the galaxy, with the early type having a larger mass when compared with the late type. To constrain the model parameters belonging to the fifth force globally, we use a Bayesian technique, using a Python package *emcee*. Similar to the RGGR analysis, we impose criteria, i.e., $i > 30^{\circ}$ and $Q < 3$, for selecting the SPARC galaxies. To ensure the convergence of the *emcee* chain [200] and due to the computational limitation, we choose a maximum of 10 galaxies to analyze in a group. In addition to the global parameters, the gravity model also includes mass-to-light ratio and DM model free parameters that are constrained independently for each galaxy within the group.

Using the free parameters constrained by the RC analysis, we further analyze two empirical relations established from the SPARC catalog, i.e., RAR [94] and BTFR [143, 234]. RAR shows that the baryonic and observational acceleration for the SPARC galaxies follows a particular scale-dependent relation. Similarly, BTFR states a power law relation between the baryonic mass and velocity measured at the flat region of the RC. Both the empirical relations are constrained from the observational data irrespective of the underlying gravity model and are discussed in detail in Sec.1.1.3 in Chapter 1. Thus, comparing the RAR and BTFR in the MOG framework with the observational one helps to check the consistency of the model further. An additional test performed on the YMOG model includes a comparison with the observational normalized additional velocity (NAV). The methodology for NAV analysis as proposed in [99] studies the difference between the net circular velocity and the baryonic components of the galaxy. For the present analysis, the circular velocity will have a contribution from the YMOG model. We also compare the YMOG model with an alternative scenario where $\beta = 0$, i.e., a purely DM model. To claim the favorability of one model over another, we use Bayesian Inference Criteria (BIC) [201]. Furthermore, we also measure and compare the average goodness of fit for a group of galaxies.

The chapter is organized as follows. Sec.5.2 discusses the alternative gravity model that is looked into. Sec.5.3 mentions the galaxy catalog and the empirical relations along with NAV

that are studied to constrain the parameters and check the consistency of the gravity model. The next Sec.5.4 specifies the technique applied to constrain the global as well as local parameters of the model. In the following Sec.5.5, we discuss the results of our analysis with RC and the three SPARC relations (RAR, BTFR, & NAV).

5.2 Yukawa Modified gravity model (YMOG)

The phenomenological gravity model that is looked into introduces a Yukawa-like correction to the Newtonian potential that influences the kinematics on the galactic scale. In contrast to the RGGR model, where the presence of DM is completely neglected, our study is in line with work done by [83], where it was shown that an attractive coupling between the DM and the Yukawa potential consistently explains the kinematics of spiral galaxies. Thus, the net gravitational potential in this formalism becomes [237]

$$\Psi = \Phi_{\rm gas} + \Phi_{\rm disk} + \Phi_{\rm bulge} + \Phi_{\rm DM} + \Phi_{\rm mg}. \tag{5.1}$$

where $\Phi_{\rm gas}$, $\Phi_{\rm disk}$, $\Phi_{\rm bulge}$ is the potential from the baryonic components, i.e., gas, disk, and bulge parts of the galaxy, respectively. These three components together constitute the Newtonian contribution ($\Phi_{\rm N}$) from the baryonic matter. The $\Phi_{\rm DM}$ and $\Phi_{\rm mg}$ are the contributions from the DM and modified gravity, respectively. The Newtonian potential ($\phi_{\rm N}$) due to baryonic matter is expressed as,

$$\Phi_{\rm N}(\vec{r}) = -G \int \frac{\rho_{\rm bar}(r')}{|r - r'|} d^3 r', \tag{5.2}$$

here, $\rho_{\rm bar}(r')$ is the density, which incorporates the matter distribution of the baryonic components. A similar Newtonian contribution arises from the choice of DM profile,

$$\Phi_{\rm DM}(\vec{r}) = -G \int \frac{\rho_{\rm DM}(r')}{|r - r'|} d^3 r', \tag{5.3}$$

where $\rho_{\rm DM}$ is the density profile for the DM distribution. In addition to the Newtonian potential, there is a contribution due to the Yukawa-like fifth force expressed as

$$\phi_{\rm mg}(\vec{r}) = -G \int \frac{\rho_{\rm DM}(r')}{|r-r'|} \beta e^{-\frac{(|r-r'|)}{\lambda}} d^3r', \tag{5.4}$$

where β is the coupling constant for the fifth-force interaction with the DM component, which can be either attractive or repulsive depending on the positive or negative sign, and λ is the range of the fifth-force. Clearly, the fifth force is coupled only to the DM contribution. The motivation for such an assumption is the smallness of the coupling parameter between baryon-baryon interaction as determined from the local gravity experiments [153] as discussed in detail in Sec.1.2.2 in Chapter 1. In particular, these model parameters λ and β, associated with the fifth force, are constrained by comparing the predicted net velocity ($v_c = \sqrt{r\frac{d\Psi}{dr}}$) with the observational RC.

For the choice of the DM density profile, we select the well-known NFW profile as discussed in Sec.1.2.4. The NFW profile has the following form [36]

$$\rho_{\rm DM}(r) = \frac{\rho_{\rm s}}{r/r_s(1+r/r_{\rm s})^2}$$

where $\rho_{\rm s}$ and $r_{\rm s}$ are the characteristic density and scale radius for the NFW halo, respectively. For the galaxy-sized halos, we utilize the following assumption to relate the concentration parameter (c) with the virial mass M_{200} [83, 196]. Given the density profile for the DM, the velocity contributions from these additional components, i.e., dark matter ($v_{\rm DM}$) and modified gravity ($v_{\rm mg}$), becomes

$$v_{DM}^2 = \frac{4\pi G\rho_{\rm s} r_{\rm s}^3}{r}\left[-\frac{r}{r+r_{\rm s}} + ln\left(1+\frac{r}{r_{\rm s}}\right)\right]$$

$$v_{\rm mg}^2 = -\frac{2\pi G\beta\rho_{\rm s}r_{\rm s}^3}{r}\Big\{\frac{2r}{r+r_{\rm s}} + exp\left(\frac{r_{\rm s}+r}{\lambda}\right)\left(\frac{r}{r_{\rm s}}-1\right) Ei\left(-\frac{r_{\rm s}+r}{\lambda}\right) + exp\left(-\frac{r_{\rm s}+r}{\lambda}\right) + exp\left(-\frac{r_{\rm s}+r}{\lambda}\right)\left(1+\frac{r}{\lambda}\right) \left[exp\left(\frac{2r_{\rm s}}{\lambda}\right)Ei\left(-\frac{r_{\rm s}}{\lambda}\right) + Ei\left(\frac{r_{\rm s}}{\lambda}\right) - Ei\left(\frac{r+r_{\rm s}}{\lambda}\right)\right]\Big\}, \quad (5.5)$$

Due to the linearity of the total potential (Eq.5.1), the analytical expression for the total circular velocity (v_c) is expressed as [237],

$$v_{\rm c}^2(r) = |v_{\rm gas}(r)||v_{\rm gas}(r)| + \gamma_{\rm d}v_{\rm disk}^2(r) + \gamma_{\rm b}v_{\rm bulge}^2(r) + v_{\rm DM}^2(r) + v_{\rm mg}^2(r), \quad (5.6)$$

here, $v_{\rm disk}$, $v_{\rm bulge}$, and $v_{\rm gas}$ are the velocities for the stellar disk, bulge, and gas components of the galaxy for a given radius, respectively. Also, $\gamma_{\rm d}$ and $\gamma_{\rm b}$ are the stellar mass-to-light ratio of disk and bulge components, respectively. The parameter M_{200} corresponds to the virial mass for a NFW halo. Apart from these three local parameters ($\gamma_{\rm d}$,$\gamma_{\rm b}$, M_{200}) specific to the galaxy in question, $v_{\rm c}$ also depends on the global parameters related to the fifth force (β, λ) through $v_{\rm mg}$. The velocity corresponding to the baryonic components for a given galaxy is obtained from the SPARC catalog. Our analysis aims to constrain these model parameters using the Bayesian technique by comparing the model predictions with the observational data from the SPARC catalog.

5.3 Observational Data: SPARC

The consistency of the RC in the MOG framework is tested by comparing it with the observational data from the SPARC catalog. However, contrary to the individual study for the RGGR model (Sec.4.3), the YMOG aims to study a more general global analysis. The net velocity experienced by an object within the galaxy in the YMOG framework is expressed using Eq.5.6. The SPARC data contains the radial velocity contribution from the baryonic contribution, i.e., disk (v_{disk}), bulge (v_{bulge}), and gas (v_{gas}). The velocity for the two baryonic components, i.e., disk and bulge, is scaled by a constant mass to light parameter γ_d, γ_b, respectively. The sum of the first three terms in Eq.5.6 is the baryonic contribution represented as v_N^2 in our analysis.

Also, the parameters δ and λ corresponding to the fifth force are treated globally for a set of galaxies. Thus, in the YMOG analysis, we utilize the morphological division of the SPARC to categorize and group galaxies. Hence, the galaxies belonging to the 3 morphological divisions, i.e., early, spiral, and late-type, are grouped such that β and λ are global for each type. However, the remaining parameters ($\gamma_{\rm d}$, $\gamma_{\rm b}$, M_{200}) are constrained independently (locally) for each galaxy within the set.

We additionally probe two model-independent relations from the SPARC, i.e., RAR and BTFR, using the best-fit parameters (global and local) obtained from the RC analysis of the selected galaxies. RAR relates the observed and the baryonic acceleration for the SPARC galaxies as, $\left(a_{\rm obs}(R) = \frac{a_{\rm bar}(R)}{1-\exp(-\sqrt{a_{\rm bar}(R)/a_*})}\right)$, where a_* is the acceleration scale parameter and has best-fit value $a_* = 1.2 \times 10^{-10}$ ms^{-2}. For the YMOG scenario, the observed acceleration, in addition to the baryonic content, has a contribution from DM and DM-coupled fifth force. Thus, the net observed acceleration becomes

$$a_{mg}(R) = \frac{v_{\rm c}^2(R)}{R} = \frac{v_{\rm bar}^2(R)}{R} + \frac{v_{\rm NFW}^2(R)}{R} + \frac{v_{\rm mg}^2(R)}{R} \tag{5.7}$$

The best-fit value of the model parameters, present in the definition of velocity contribution, is constrained from the Bayesian RC analysis for a set of galaxies belonging to a given morphological type. To test the consistency of the model, we compare the net acceleration obtained in the MOG scenario (Eq.5.7) with the observed relation. Similar to the discussion in the previous chapter, the baryonic acceleration (a_{bar}) is the sum of the disk, bulge, and gas contribution.

A similar empirical relation determined from the observational data is BTFR, which compares the baryonic mass of a SPRAC galaxy with the velocity measured in the flat part of the RC. The relation $M_{bar} \propto V_f^x$ return the slope x as 4 for the 153 SPARC galaxies. In the alternative gravity model, such as RGGR discussed in the previous Chapter4, the slope (x) evaluated for the qualifying 93 galaxies is 3.42 and is consistent with the observational measurements. Similarly, in the present Chapter, we study the BTFR corresponding to the YMOG scenario such that the flat velocity on the galactic scales is measured at $r = 3.2r\ R_d$ using Eq.5.6. Also, M_{bar} is the baryonic mass (disk, bulge, and gas) for a galaxy as specified in the SPARC catalog.

NAV: To further validate the consistency of the MOG model, we examine the normalized additional velocity (NAV) for the RC fit parameters with the morphological division of the catalog. NAV focuses on the radial variation of the normalized additional component, which explains the missing mass of the galaxy and is defined as,

$$\delta v^2(r_n) = \frac{\Delta v^2(r_n r_{\rm max})}{\Delta v^2(r_{\rm max})}, \tag{5.8}$$

where $r_n = r/r_{\rm max}$ is the normalized radius with $r_{\rm max}$ being the maximum distance at which observational data is recorded. This ensures that the normalized radius r_n lies within $[0,1]$. For the observational data from SPARC, $\Delta v^2(r) = v^2_{\rm obs}(r) - v^2_{\rm bar}(r)$ measures the radial variation of the inadequacy of the baryonic components ($v_{\rm bar}(r)$) to explain the observed circular velocity ($v_{\rm obs}(r)$).

For the modified gravity model, Δv^2 is the difference between the squares of the net circular velocity from the model ($v_{\rm c}$) and the baryonic part ($v_{\rm bar}$). This results Δv having contributions from the DM ($v_{\rm DM}(r)$) and the modified gravity ($v_{\rm mg}(r)$) velocity components. Using the constrained model parameters, both the local and global ones, we aim to check the consistency of the observed NAV for the modified gravity model.

The above-mentioned empirical relations are derived purely from observational data having no dependence on the underlying gravity model. Thus, if the present mixed gravity model is consistent in explaining the RC of the galaxy, the phenomenological study must also be compatible with the relations mentioned above. This requires constraints on the model parameters computed from the RC fit for the sample of galaxies. In this chapter, we constrain the model parameters globally for a set of galaxies grouped based on their morphological type. Additionally, we also check the compatibility of a global parameter using the empirical relations that are fixed for all the selected galaxies from SPARC [83].

5.4 Methodology

To study the SPARC galaxies in the MOG framework, we aim to group galaxies based on their morphological types and constrain the model parameters, which include both the global (β, λ) and local (γ_d, γ_b, M_{200}). In a given set, the global parameters are assumed to be constant for all the galaxies, whereas the local parameters are varied independently for each galaxy selected for the analysis.

To sample the parameter space for our choice of MOG model, we use a Bayesian technique, i.e., Markov Chain Monte Carlo package in Python [200] also discussed in Chapter4. Similar to the RGGR analysis, assuming that the errors in the observed RC data follow the Gaussian distribution, the likelihood for each galaxy takes the following form

$$\mathscr{L}(\theta_j,\beta,\lambda) = (2\pi)^{(-N/2)} \left\{ \prod_{i=1}^{N} \sigma^{-1} \right\} \times exp \left\{ -\frac{1}{2} \sum_{i=1}^{N} \left(\frac{v_{obs,j}(r_i) - v_c(r_i,\theta_j,\beta,\lambda)}{\sigma(r_i)} \right)^2 \right\} \quad (5.9)$$

here $\boldsymbol{\theta_j} = \{\gamma_d, \gamma_b, M_{200}\}$ which varies with every galaxy, and β, λ are the global parameters for the given set of morphological type. Also, N is the number of observational data points for each galaxy, and $\sigma(r_i)$ is the error on the observational velocity. For a set of j galaxies, $v_{obs,j}(r_i)$ represents the observed velocity of the j-th galaxy at radius r_i. Also, $v_C(r_i, \boldsymbol{\theta_j}, \beta, \lambda)$ is the net velocity, which includes the contribution from both DM and its coupling to the Yukawa model as given by Eq.5.6. As the observational data measurements are independent for each galaxy, the total likelihood for a group of N_g galaxies can be defined as

$$\mathscr{L}(\boldsymbol{\theta_j},\beta,\lambda) = \prod_{j=1}^{N_g} \mathscr{L}_j(\boldsymbol{\theta_j},\beta,\lambda) \quad (5.10)$$

where $\boldsymbol{\theta_j} = \boldsymbol{\theta_1}, ..., \boldsymbol{\theta}_{N_g}$ is a set of local parameters constrained independently for each set of N_g galaxies.

The sampler also depends on priors set on each free parameter, i.e., $P(\theta)$. In our analysis, similar to [83], we assume uniform flat priors for the parameter space. The stellar mass-to-light

ratio for disk and bulge are assumed to vary in the range of $0.3 < \gamma_d < 0.8$ and $0.3 < \gamma_b < 0.8$ [198]. The additional local DM parameter is assumed to lie within $10^9 < M_{200}/M_\odot < 10^{13}$. Similarly, for the global parameters, $-2.0 < \beta < 2.0$, $\bar{\lambda} < \lambda/kpc < 100$, where $\bar{\lambda}$ is the average of the smallest radius for individual galaxies taken in a set.

Additionally, $\beta = 0$ in Eq.5.4 corresponds to a standard NFW scenario, where the net velocity for a galaxy has a contribution only from DM and baryons. Similar to the model comparison done for the RGGR, we measure the favorability of the chosen MOG with a ΛCDM model using Bayesian Information Criteria (BIC). As discussed, BIC for a given model is defined as [201]

$$BIC = -2\ln\mathscr{L}_{max} + 2k(\ln N), \tag{5.11}$$

here, k and N are the free parameters and the total number of data points for a set of galaxies, respectively. Under the assumption that the errors on the observational RC follow a Gaussian distribution, the first term in Eq.5.11 is $\chi^2_{\rm min}$. A relative comparison of the MOG model with the model constituting purely of DM (NFW profile) can be calculated using

$$\Delta BIC \equiv BIC|_{\beta\neq 0} - BIC|_{\beta=0}, \tag{5.12}$$

where $\beta = 0$ corresponds to the DM-only model and $\beta \neq 0$ represents the model inclusive of both DM and fifth force. The measure of favorability of the MOG model over NFW is determined by ΔBIC being positive. Also, the higher the magnitude, the stronger the preference for one model over another.

Additionally, measuring the convergence of the emcee chain for a global YMOG analysis remains similar, as discussed in Chapter 4. In addition to the hardware limitation, the convergence test constraints the number of galaxies that can be taken in a sample. Therefore, to ensure we can run sufficient chains, we sample galaxies based on their morphological types in a maximum set of 10 galaxies.

Table 5.1: The global parameters for the set of galaxies belonging to each morphological type in SPARC. The table compiles the best-fit value for the Yukawa parameters (β, λ) for each set of galaxies. $N_{\rm gal}$ is the number of galaxies studied collectively for a given set. Additionally, $N_{\rm par}$ and $N_{\rm data}$ are the number of parameters constrained and data points for the galaxies. The goodness of fit measured for two scenarios, i.e., MOG and NFW, is represented via χ^2_{red} in the table. The favorability of the MOG model in comparison to the NFW is quantified using the positive value of the ΔBIC. The global parameters for the set of galaxies belonging to each morphological type in SPARC. The table compiles the best-fit value for the Yukawa parameters (β, λ) for each set of galaxies. $N_{\rm gal}$ is the number of galaxies studied collectively for a given set. Additionally, $N_{\rm par}$ and $N_{\rm data}$ are the number of parameters constrained and data points for the galaxies. The goodness of fit measured for two scenarios, i.e., MOG and NFW, is represented via $\chi^2_{\rm red}$ in the table. The favorability of the MOG model in comparison to the NFW is quantified using the positive value of the ΔBIC.

	Yukawa parameters						
Morphology	β	λ (kpc)	$N_{\rm par}$	$N_{\rm data}$	$\chi^2_{\rm red}(MOG)$	$\chi^2_{\rm red}(NFW)$	ΔBIC
Early-type	$1.15^{0.11}_{-0.09}$	$29.55^{6.75}_{-4.75}$	32	292	0.66	3.55	426.17
Spiral	$0.45^{0.09}_{-0.09}$	$8.49^{2.27}_{-1.45}$	25	177	0.63	0.79	24.96
LD	$0.49^{0.09}_{-0.08}$	$3.66^{1.61}_{-0.92}$	22	163	0.66	1.03	45.72

5.5 Results

The phenomenological task of fitting the model parameters utilizes the SPARC RC data. The SPARC contains RC data for different kinds of galaxies. Using the morphological divisions, we fit the global parameters β and λ corresponding to the fifth force for a given type. Additional local parameters, i.e., $\gamma_{\rm d}$, $\gamma_{\rm b}$, and M_{200} are modeled independently for each galaxy in the sample. This study gives an estimate of the divergence of the global value for the Yukawa parameters [83] from the morphology-specific study. The consistency of the YMOG with the observational RC is measured using the goodness of fit. Additionally, the favorability of the gravity model is computed using ΔBIC, which measures the difference in BIC between two models, i.e., pure DM ($\beta = 0$) and DM with the fifth force ($\beta \neq 0$). We also analyze the empirical relations, such as RAR and BTFR, for the selected galaxies. Additionally, we study the NAV analysis

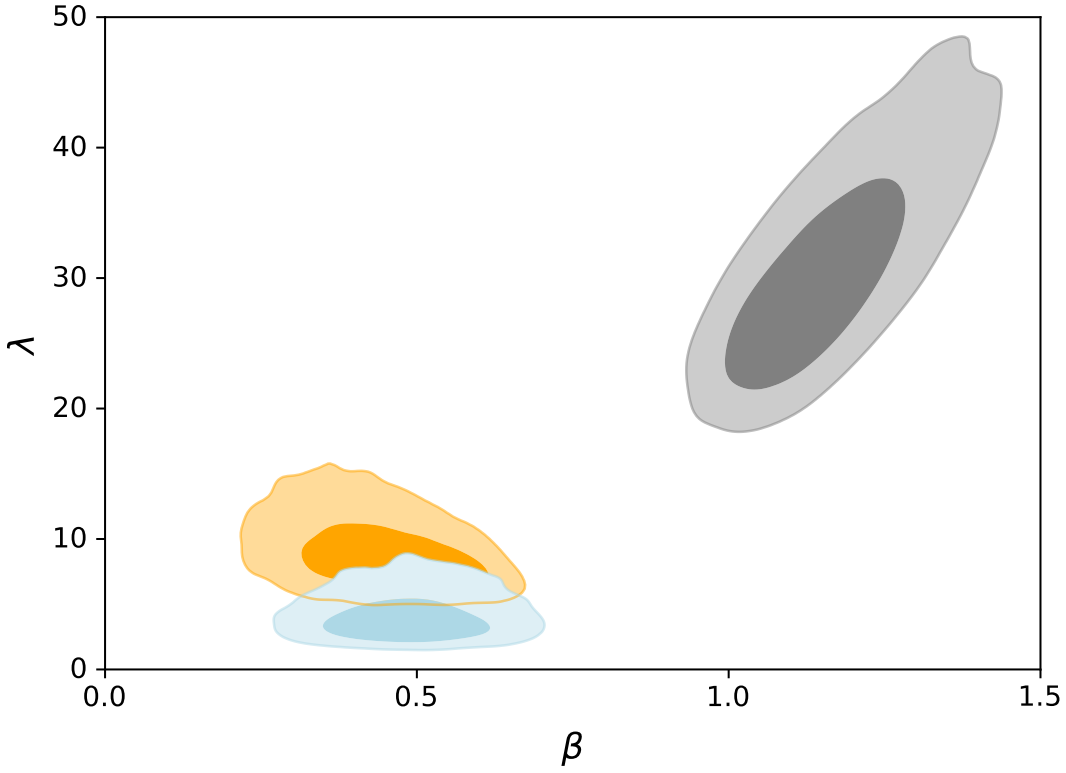

Figure 5.1: The plot shows the 2σ marginalised posterior of the global parameters β and λ for the set of galaxies belonging to 3 morphologies. The gray contour represents the collection of early-type galaxies. Similarly, the yellow and blue posterior distribution belongs to the set of spiral and late-type galaxies.

for the selected galaxies in the YMOG framework by comparing it with the observational NAV computed from the SPARC catalog.

RC analysis

To test the MOG model against the SPARC observations, we focus on 3 morphological types, i.e., early, spiral, and late-type. For each group, the galaxies are selected from the eligible 153 galaxies based on SPARC selection criteria [120]. Additionally, to ensure that the convergence of the emcee chain is achieved, we sample a maximum of 10 galaxies for the likelihood analysis.

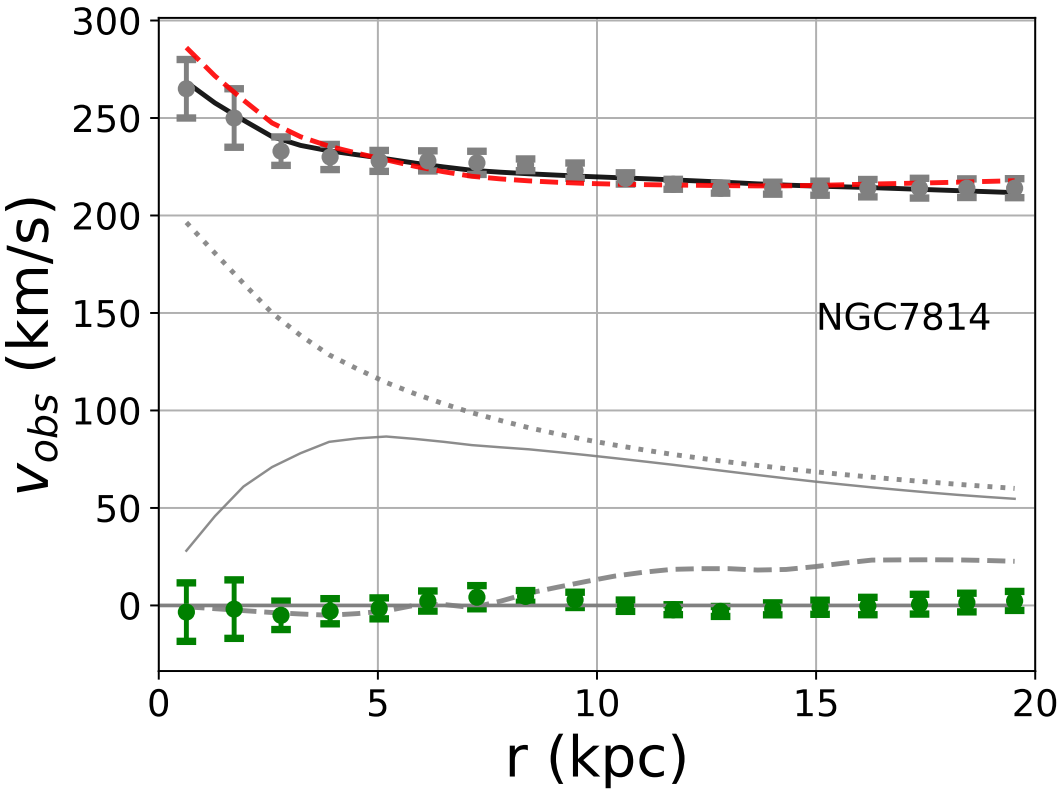

Figure 5.2: The net velocity contribution of NGC7814 in MOG framework. The gray points with error bars are the observational data points. The gray dotted line is the observed contribution from the gaseous component scaled by γ_d. Similarly, the dashed-dotted and dashed lines are the baryonic contributions from disk and gas, respectively. The green dots with error bars are the residuals with the best-fit value for the parameters.

Early-type galaxy

The early-type galaxies are characterized by a prominent bulge at the center with tightly woven spiral arms. Such galactic systems are known to have older stellar distributions with large densities and, thus, are known to lie at the higher end with respect to baryonic mass. We selected 9 early-type objects from the eligible SPARC galaxies. Our analysis constrains the model parameters, both local (γ_b, γ_b, M_{200}) and global (β, λ) ones. Using the sampler, the best-fit values for β and λ, along with the 1σ error estimates evaluated from the credible intervals, are found to be $1.15^{+0.11}_{-0.09}$ and $29.55^{+6.75}_{-4.75}$ kpc, respectively. The positive value for β shows that the coupling of Yukawa potential with the fifth force is attractive in nature. The large value of the scale parameter implies the large size of the early-type galaxies. Additionally, the parameters γ_d, γ_b and M_{200} are constrained independently for each galaxy. The goodness of fit evaluated for each

galaxy within the sample shows that the YMOG model is consistent with the observed RC. We compile the global parameters (β, λ) for the set of early-type galaxies in Table.5.1. The table also shows the mean $\chi^2_{\rm red}$ for the YMOG is 0.66 for this set of galaxies. Similarly, the mean goodness of fit for the set of 9 galaxies in the NFW model is 3.55. The table also mentions the number of galaxies ($N_{\rm gal}$), the number of model parameters ($N_{\rm par}$), and the total number of data points ($N_{\rm data}$) studied collectively for a given set. The last column mentions the relative ΔBIC computed for the two models. It is positive and large (426.17) for the early-type galaxies, hinting towards the favorability of the YMOG scenario compared to the pure DM model. The 1σ and 2σ marginalized distributions of the global parameters β and λ are represented in Fig.5.1 by the pink contours.

For reference, we show the plot for a single early-type galaxy, i.e., NGC7814, in Fig.5.2. The SPARC observed RC data with errors are shown by gray data points. The gray thin continuous line is the observed contribution from the disk component scaled by γ_d. Similarly, the dashed-dotted and dashed lines are the baryonic contributions from disk and gas, respectively. The YMOG best-fit values for the local parameters, i.e., $\gamma_{\rm d}$, $\gamma_{\rm b}$, and $M_{200} \times 10^{11} M_{\odot}$, are $0.71^{+0.06}_{-0.11}$, $0.57^{+0.04}_{-0.03}$, $5.20^{+0.75}_{-0.74}$, respectively. The β and λ are taken to be the ones from the Table.5.1. Substituting the global and local best-fit values in Eq.5.6, the net velocity contribution for the modified gravity framework is shown by a solid black line. The measured goodness of fit using the YMOG-constrained parameters is 0.41. The green dots with error bars are the residuals with the best-fit value for the YMOG parameters, indicating a satisfactory fit. The plot also shows the velocity for the pure DM contribution, i.e., $\beta = 0$ scenario. The best-fit parameters obtained are $\gamma_{\rm d}$, $\gamma_{\rm b}$, $M_{200} \times 10^{11}$ as $0.77^{+0.02}_{-0.04}$, $0.67^{+0.03}_{-0.03}$ and $24.54^{+1.07}_{-1.07}$, respectively. It is to be noted that as the contribution from YMOG is switched off, the required DM density to explain observed circular velocity increases. This is also reflected in the increase in the magnitude of M_{200}. The net contribution obtained for the NFW model is shown via the red dotted line in Fig.5.2. The measured $\chi^2_{\rm red}$ for the scenario is 1.17, which, although still consistent, is larger than the YMOG model.

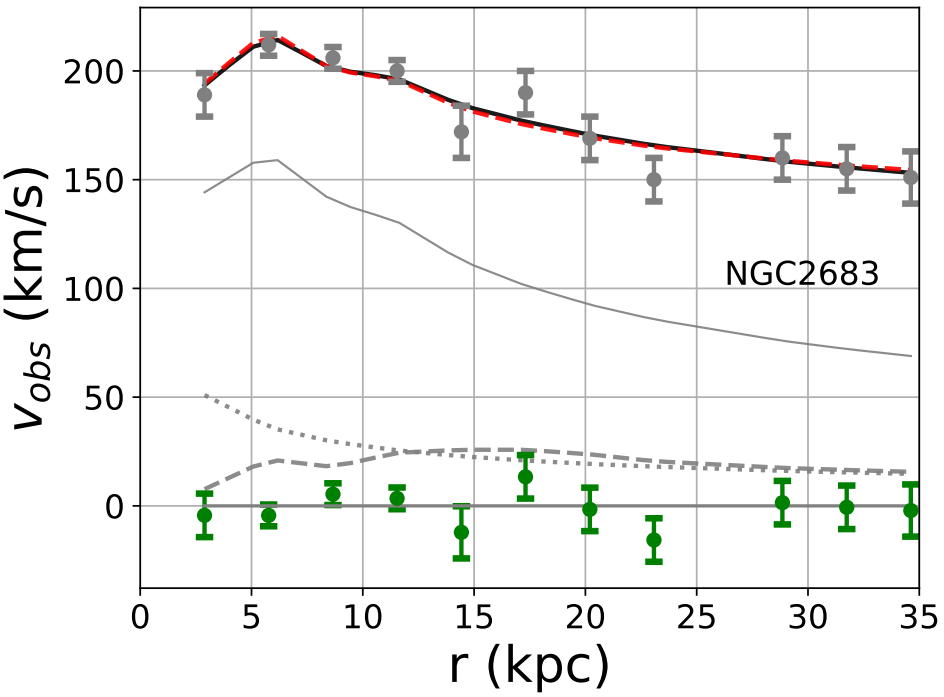

Figure 5.3: The RC for spiral galaxy NGC2683 in MOG framework. The gray dots with error bars represent the observational SPARC data [120]. The solid black line is the net contribution from the analytical MOG model obtained by substituting the best-fit parameter. The grey lines represent the baryonic components of the galaxy as discussed in Fig.5.2. The green dots are the measured residuals.

Spiral galaxy

Unlike the early type, spiral galaxies have smaller bulges and loosely wound spiral arms, containing a large amount of dust and gas. The collection in SPARC contains a large number of unbarred spiral galaxies. For our analysis, we selected random sets of about 10 galaxies to ensure the convergence of the sampler. For the set reported here, we consider 10 random galaxies and the best-fit value for the global parameters β and λ are found to be $0.45^{+0.09}_{-0.09}$ and $8.49^{+2.27}_{-1.45}$ kpc, respectively. Note the smaller scale parameter consistent with the size of the typical spiral galaxies compared to the early type ones. Similar analysis with the other sets also resulted in λ of the same order. Table.5.1 compiles the parameters for this typical set of spiral galaxies. The average $\chi^2_{\rm red}$ calculated for YMOG is 0.63, showing a slight preference for this modified gravity model compared to average NFW with $\chi^2_{\rm red} = 0.79$. The 1σ and 2σ marginalized distributions of the global parameters β and λ for this set are shown in Fig.5.1 by the

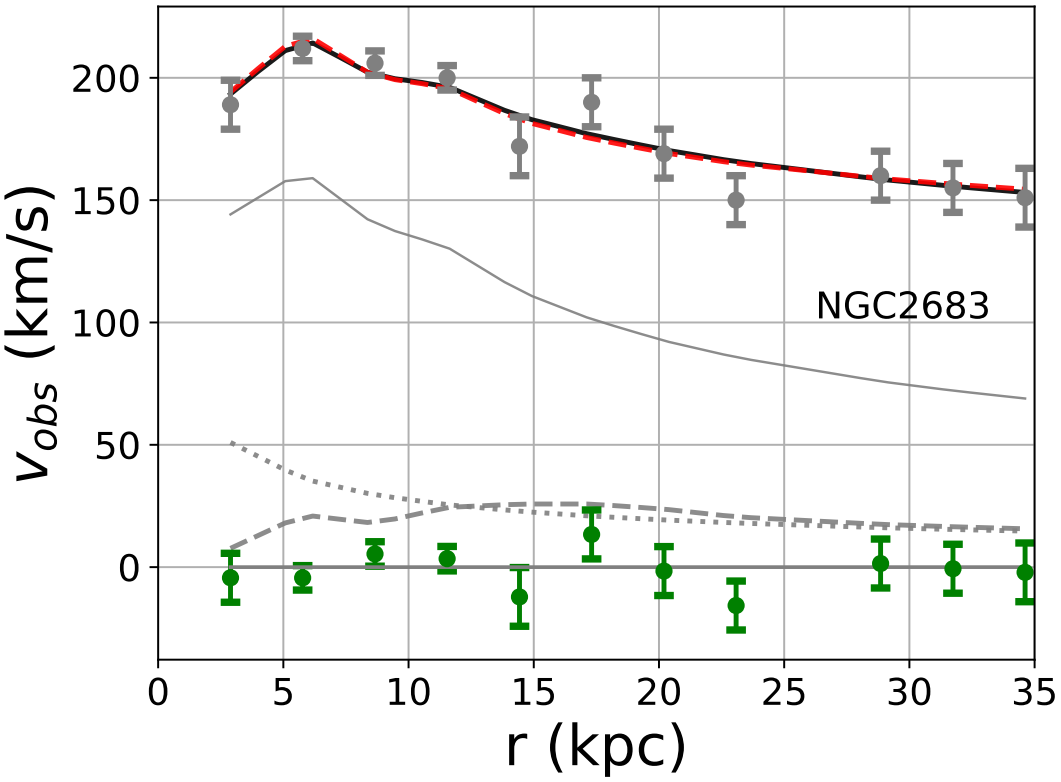

Figure 5.4: The RC for spiral galaxy NGC2683 in MOG framework. The gray dots with error bars represent the observational SPARC data [120]. The solid black line is the net contribution from the analytical MOG model obtained by substituting the best-fit parameter. The gray lines represent the baryonic components of the galaxy as discussed in Fig.5.2. The green dots are the measured residuals.

yellow contours Fig.5.1. Clearly, the early type and the spiral galaxies, with their morphology differences, prefer very different model parameters for the YMOG.

To illustrate the fitting of the model, we plot the RC (gray data points) for a single spiral galaxy viz. NGC2683 in Fig.5.4. The black solid line is the net contribution from the choice of the modified gravity model. The best-fit values for the local parameters are $\gamma_{\rm d} = 0.62^{+0.04}_{-0.04}$, $\gamma_{\rm b} = 0.52^{+0.18}_{-0.15}$ and $M_{200} \times 10^{11} M_{\odot} = 3.81^{+0.70}_{-0.61}$ with the λ, β taken from table 5.1 spiral set. The measured $\chi^2_{\rm red}$ for the scenario gives 0.72. The baryonic contribution of the galaxy is represented via the gray lines and follows a similar convention as Fig. 5.2. Additionally, the plot shows the residual measured for the galaxy using green data points. The figure compares the YMOG with the NFW model and is shown using a red dotted line in Fig.5.4. For the NFW model, the best-fit parameters ($\gamma_{\rm d}$, $\gamma_{\rm b}$, $M_{200} \times 10^{11}$ ($M_{\odot}$)) obtained are $0.69^{0.04}_{-0.03}$, $0.49^{0.19}_{-0.14}$ and $4.16^{1.17}_{-1.20}$ with $\chi^2_{\rm red}$ as 0.86. A comparison of the goodness of fit for the models shows that the

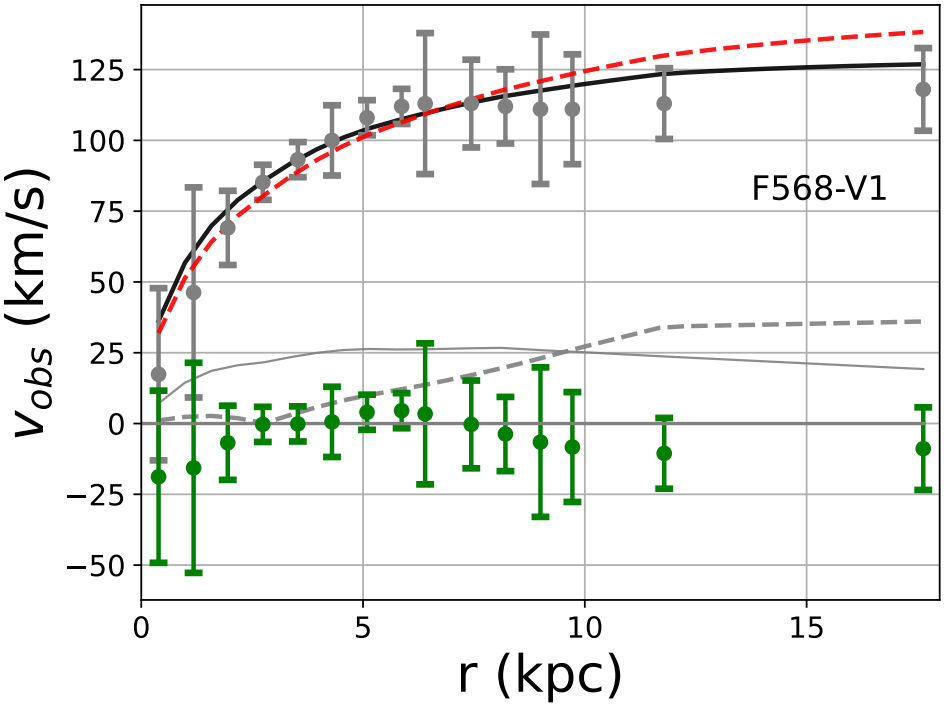

Figure 5.5: The plot shows the RC of Late-type dwarf galaxy F568-V1. The gray dots with error bars represent the observational SPARC data [120]. The black solid line shows the net velocity obtained with the constrained parameter in the MOG model. The gray lines represent the baryonic contribution of the galaxy, as discussed previously. The gray and green data points in the plot show the observational data and residual data, respectively.

Yukawa model fits the data slightly better than the DM model. To state the favorability quantitatively, we show the ΔBIC in Table.5.1. The ΔBIC measured for the spiral galaxy set has a positive magnitude, implying that the YMOG model is favored more than the NFW model.

Late-type dwarf galaxy

The late-type morphology includes galaxies with no visible bulge present and containing loosely wound spiral arms. Such galaxies have a comparatively large gas content dispersed and, thus, high star formation activity. Thus, similar to the other two morphological types, we discuss a set of 10 galaxies to study the YMOG model. Using the emcee sampler, we constrain the global and local model parameters. The best-fit value for β and λ is $3.66^{1.61}_{-0.92}$, $0.49^{0.09}_{-0.08}$ kpc, respectively and are mentioned in the Table.5.1. Similar to the early and spiral galaxies, the value for the coupling parameter (β) is positive, which shows the attractive nature of the Yukawa force. The

1σ and 2σ marginalized distribution of the free parameters β and λ are shown in Fig.5.1 by the green contours. The late-type ones show contours similar to those of the spirals. However, the model parameter difference from the early types remains significant. In Fig.5.5, we plot the RC for a single late-type dwarf galaxy F568-V1 from the set. The constrained local mass model parameters for baryonic (γ_d) and DM components ($M_{200} \times 10^{11}$ ($M_\odot$)) are $0.58^{0.15}_{-0.18}$ and $3.25^{0.86}_{-0.73}$, respectively. The β and λ values are the global values for the set from Tab.5.1. The evaluated $\chi^2_{\rm red}$ obtained for these best fit YMOG parameters is 0.21. The black solid line shows the net velocity contribution, including DM and the fifth force. The gray dots with error bars are the observational data points mentioned in SPARC. The gray lines show the baryonic contribution of the galaxy and follow a similar convention to other morphological types. The dotted red line is the net velocity contribution from the pure DM (NFW) model. The best-fit value obtained using the sampler for the NFW case gives ($\gamma_{\rm d}$, $\gamma_{\rm b}$,$M_{200} \times 10^{11}$ ($M_\odot$)) as $0.77^{0.02}_{-0.04}$, $0.67^{0.03}_{-0.03}$, $5.29^{1.07}_{-1.07}$ with $\chi^2_{\rm red}$ is 0.52. The plot also shows the residual evaluated from the observational and analytical velocity, represented by the green points. The measured relative *BIC* between the two models has a large positive magnitude, signifying that the YMOG model is preferred over the pure NFW DM scenario.

This morphology-based RC analysis for the YMOG is best summarized in Fig.5.1. Clearly, galaxies with similar scale values have overlapping contours. However, the larger early-type galaxies create tension due to vast size differences from the other two kinds. We found this tension resulting in non-convergence of best-fit analysis when samples are created with equal representation of each kind. As computational bounds did not let the sample size go beyond 10 objects in one set, a proper global analysis remains elusive. However, we also find that giving more significant weight to one kind, like sets consisting of spiral galaxies, yields convergence and results in best-fit values similar to the spiral ones [83].

Empirical relations and NAV

Using the best-fit parameters constrained from the RC analysis, we aim to check the consistency of the model-independent empirical relation, i.e., RAR and BTFR. We also verify the fit with an additional NAV analysis and compare it with the observational relation. Assuming that the

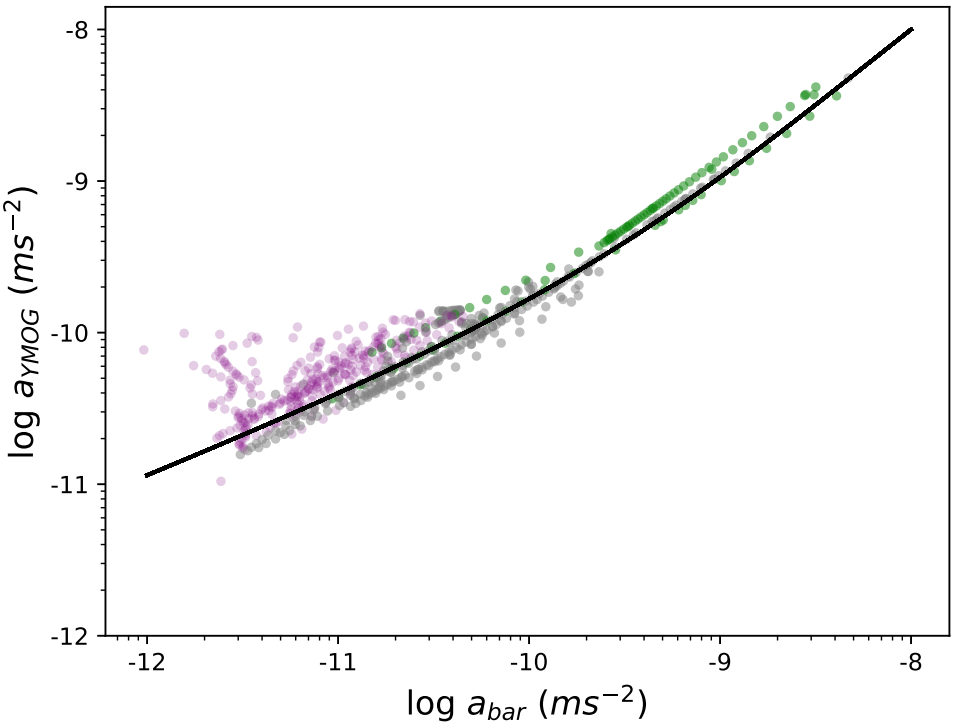

Figure 5.6: The plot shows the RAR measured for the selected SPARC galaxies in the MOG framework. The free parameters of the gravity model (global and local) are constrained using RC. The black solid line is the observational RAR evaluated from the observational data [120]. The galaxies belonging to different morphology are color-coded with green representing the RAR for early-type in the YMOG scenario. Similarly, gray and purple data points are the RAR shown for spiral and late-type galaxies, respectively.

modified gravity influences the galactic kinematics, we compare the YMOG-modified empirical relations with the observational RAR and BTFR.

RAR: The observational RAR for the 153 SPARC galaxies is shown by the solid black line in Fig.5.6. To evaluate the RAR in the YMOG framework, we estimate the net acceleration by the Eq.5.7 where the last term contains the contribution from the Yukawa model. For β and λ, we use the values from the morphological fits in Table 5.1. Additionally, the local parameters, i.e., $\gamma_{\rm d}$, $\gamma_{\rm b}$ and M_{200} are constrained individually for the galaxies. The mass-to-light ratio for disk and bulge is fixed to be 0.5 for all the galaxies analyzed. The $a_{\rm bar}$ is the sum of disk, bulge, and gas acceleration given by Eq.1.6 and is taken from the SPARC [120]. The individual data point in

Fig.5.6 represents the modified acceleration at a particular radius for all the selected galaxies in the MOG framework. A comparison of the observational RAR with the corresponding relation for MOG in Fig.5.6 shows that the model is consistent. The residual computed for the 1366 data points for galaxies belonging to different morphological types for MOG is 0.13, similar to the observational RAR [94]. In total, we use the data from 63 galaxies to construct the RAR plot in Fig.5.6. We have plotted the galaxies with different morphologies in different colors. The green, gray, and purple data points represent the early-type, spiral, and late-type galaxies, respectively. This study, for the first time looking into morphology dependency of the RAR, reveals that the early types and the spiral galaxies follow the RAR to a much larger degree than the late dwarfs. This behavior of the late-type galaxies might be linked to their smaller scale length and, hence, limited data points in these objects. This calls for a detailed analysis beyond the scope of this discussion.

BTFR: In the second empirical relation, BTFR, we compare the baryonic mass ($M_{\rm bar}$) with the observed flat velocity ($V_{\rm f}$), i.e., $M_{\rm bar} \propto V_{\rm f}^{x}(x)$. A similar relationship can be established for YMOG, where the flat velocity is measured at 3.2 R_d for the modified kinematics. As discussed earlier, the choice of 3.2 R_d ensures that 80% of the mass within the galaxy contributes to the net velocity evaluated for the MOG model. Substituting the best-fit value for the parameters in Eq.5.6 for at 3.2 R_d the $V_{\rm f}$ for the galaxy is estimated and the $M_{\rm bar}$ is referred from the catalog. This data for each galaxy is plotted in Fig.5.7. The individual data points compare the $M_{\rm bar}$ with the $V_{\rm f}$ measured for the YMOG model for each galaxy. To study the morphology dependence, the early-type, spiral, and late-type galaxies are plotted with green, gray, and purple data points, respectively. Clearly, the heavier and older galaxies of the early-type and spiral kinds point to larger baryonic masses and flat velocities. In contrast, the younger late-type galaxies remain on the lower end of the $M_{\rm bar} - V_{\rm f}$ scale.

To estimate the best-fit BTFR parameters (A, x), we constrain the relation,

$$\log(M_{\rm bar}) = x \log(V_{\rm f}) + \log\, A.$$

Using the BayesLineFit package, the parameters x and $\log A$ are estimated to be 4.72 and 0.38, respectively. The intrinsic scatter comes out to be 0.31. We also measure the vertical scatter

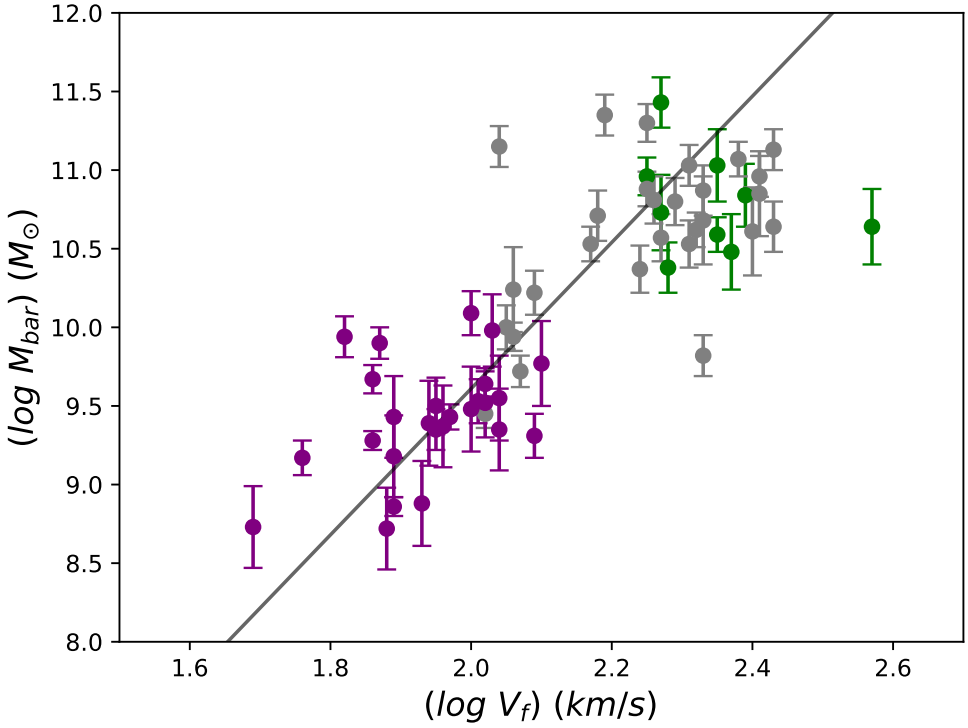

Figure 5.7: The BTFR evaluated for the MOG framework. The M_{bar} corresponds to the baryonic mass, and V_f is the flat velocity measured for the MOG model at 3.2 R_d. The dots correspond to the V_f measured for each qualifying galaxy, with green points corresponding to early-type galaxies. Similarly, gray and purple dots represent the spiral and late-tye galaxies. The black solid line fits the data using the best-fit values evaluated using BayesLinFit.

[143] for the BTFR,

$$\sigma_0 = \sqrt{\frac{1}{n}\sum^{n}[\log(M_{\rm bar}) - x\log(V_{\rm f}) - \log A]^2}, \tag{5.13}$$

where n is the number of galaxies. The σ_0 for our set of galaxies turns out to be 1.49. Substituting the best-fit value for the parameters, the BTFR obtained for the MOG model is shown via. a black solid line in Fig.5.7. The BTFR parameter x from all eligible SPARC galaxies is estimated to be [143] around 4. Though YMOG for our set of galaxies maintains a BTFR-like relation, the fit value is much larger ($x = 4.72$) than expected. This might be due to the limited dataset and the inefficiencies in the best-fit estimations. Analysis with a larger set of galaxies might reveal the true behavior. Overall, we do not claim a major breakdown of the BTFR relation for

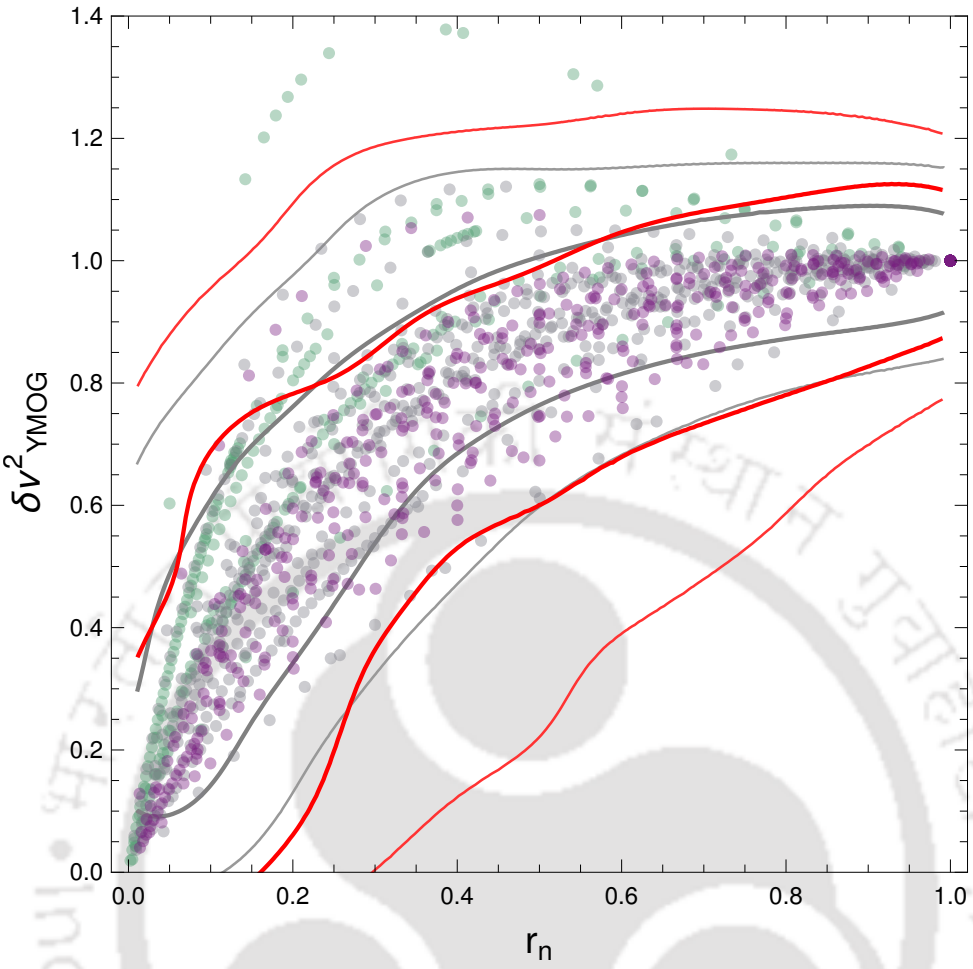

Figure 5.8: NAV analysis for the YMOG model. The blue dots represent the measured NAV for the best-fit parameters in the YMOG analysis. The gray and red lines are the HDR regions estimated for the YMOG and observational NAV [120], respectively.

the YMOG.

NAV: The expression for NAV in the MOG scenario takes the following form

$$\delta v^2_{YMOG}(r_{\rm n}) = \frac{v^2_{\rm NFW}(r_{\rm n}\, r_{\rm max}) + v^2_{\rm mg}(r_{\rm n}\, r_{\rm max})}{v^2_{\rm NFW}(r_{\rm max}) + v^2_{\rm mg}(r_{\rm max})} \tag{5.14}$$

where $r_{\rm n}$ ranges from $[0,1]$ and $r_{\rm max}$ is the maximum radius for a galaxy [99]. For the NAV analysis, we also look into the sets of galaxies divided based on their morphological types. To evaluate NAV in the YMOG scenario, we substitute the constrained parameters from the emcee analysis to evaluate a normalized difference in velocity that comprises the contribution from the DM and Yukawa models. In the Fig.5.8, the $\delta v^2_{YMOG}(r_{\rm n})$ and the corresponding $r_{\rm n}$ for each of

the data points for all the 63 galaxies in our sets are plotted. Again, the different morphology types are plotted with different colors, using the same convention of green, gray, and purple data points representing the early-type, spiral, and late-type galaxies, respectively.

We additionally fit the data to represent the high-density regions (HDR) analogous to the 1σ and 2σ distribution. The HDR regions obtained in the case of the YMOG model for our sets are shown via the gray solid lines. The thick and thin gray lines in the figure are analogous to the 1σ and 2σ HDR regions, respectively. A comparison of the HDR in YMOG with the observational NAV expresses the consistency. The plot Fig.5.8 shows the observational 1σ and 2σ distribution of NAV [99] obtained from the net circular velocity mentioned in SPARC via the red solid lines. The inner thick red lines are for the observed 1σ distribution from all eligible SPARC galaxies, and the outer thin red lines are for the observed 2σ distribution. The plot clearly shows that the HDR for YMOG covers the broad spectrum and slightly overlaps with the observational NAV. Thus, for the limited set of galaxies studied here, the NAV analysis suggests that YMOG cannot be ruled out, although there is a clear discrepancy in the global nature of the Yukawa parameters, as discussed above.

5.6 Summary

The present chapter looks into a phenomenological gravity model studying the scenario where the fifth force is coupled only with the DM component. Our analysis focuses on constraining the model parameters of the Yukawa potential globally for a set of SPARC galaxies. However, rather than looking into arbitrary galaxies, we systematically study the problem for groups of galaxies of the same kind. Our analysis shows that for a given morphological type, a constant value for β and λ is consistent with the observational RC. However, both the model parameters vary for galaxies belonging to different morphological types. In particular, for early and spiral-type galaxies, it is observed that the coupling parameter β, although different, follows a similar trend, i.e., the nature of the fifth force is attractive. The scale length λ of these galaxies are also found to be smaller in comparison to the early types. The larger early-type galaxies are expected to have longer scale lengths. We also see much larger β in comparison to the other two morphology kinds. This results in tension in the best-fit analysis when samples are created

with equal representation of each kind of galaxy, eventually leading to the non-convergence of the Monte Carlo chain. Thus, the phenomenological study of RC in this paper suggests that it is difficult to converge towards a global value for all the SPARC galaxies.

We additionally verify the claim for the non-global nature of the Yukawa parameters by probing into empirical relations such as RAR and BTFR. We perform these tests using the Yukawa parameters from the morphological study. The YMOG is found to maintain both the empirical relations broadly. We further extend the analysis by checking the NAV for the galaxies in question. The HDR from the SPARC observed NAV overlaps with the HDR from our selected set of galaxies. Thus, the YMOG model parameters extracted solely from the RC analysis satisfies the empirical relations. We also look into the distribution of the galaxy morphology in these empirical relations. These analyses show the different behavior of the different morphologies. Specific kinds of galaxies crowd in specific areas of the empirical relation parameter space. This nature is not yet well understood and needs more detailed analysis.

In summary, our analysis shows that a mixed scenario incorporating both DM and fifth force disfavors the kinematics study for an accurate global analysis. The model parameters, i.e., β and λ, fail to converge for a global nature for the SPARC galaxies. The discrepancy may arise from the choice of the DM coupling with the fifth force. The global nature of the couplings is the most important characteristic of the YMOG model. However, the tension between the different morphologies in the likelihood analysis makes realizing such a scenario difficult.

Chapter 6

Summary and Conclusions

Einstein's development of GR laid the foundation for our understanding of the Universe. A key strength of GR lies in its simplicity, as it has no free parameters that require tuning to fit the observational data. However, GR leaves certain gaps in the understanding of the Universe, many of which can be addressed through the ΛCDM or alternative gravity theories. The flexibility offered by such alternative gravity models has its advantages in explaining observational discrepancies by constraining the parameters. Yet, this very flexibility introduces certain challenges. The higher number of parameters may improve data fitting, but questions the fundamental predictive power and universality of the theory. Many alternative gravity models explored in the present thesis exhibit a scale dependence in the model parameters, which questions the fundamental nature of the gravity model. Nevertheless, it is important to note that the models demonstrate consistent behavior when tested against the observational data. Additionally, for any gravity model to be considered a viable alternative to GR, it must fulfill essential criteria such as being relativistic, self-consistent and free of any instability. It must also satisfy the gravitational dynamics both in strong and weak-field regimes [45, 215]. In this thesis, we focused on understanding the discrepancies in galactic scales by considering an alternative gravity framework. For this, we employed models that look into the modification from GR to understand the

observational data. We divided the analysis into two major studies. For the first half of the thesis, we probe different spectrums of UDGs, namely, DM-dominated and DM-deficit. In this, we looked into the kinematics of DM-dominated UDG, namely, DF44, in alternative gravity models assuming the absence of a DM component. Alternatively, the study also involved looking into DM-deficit galaxies, i.e., DF2 and DF4, to analyze the VD kinematics in accommodating alternative gravity models. For the second half of the thesis, we focused on the RC analysis of rotationally supported galaxies in SPARC by studying two modified gravity models, RGGR and MOG. Our analysis for both gravity models aimed to check the consistency by comparing the observational data and constraining the model parameters. Among the alternative gravity models that are studied, the free parameters of the model may be dependent on the scale of the system. Though this scale dependence of the phenomenological parameter may question the fundamental nature of these alternative gravity models, they remain a consistent theory of gravity. However, for any alternative gravity model to be considered viable, it must satisfy the consistency criteria, i.e., relativistic, self-consistent, and a complete theory free of ghosts and instabilities. The theory also requires the ability to explain the gravitational dynamics both in the strong and weak-field regimes as well, and it should regain a valid Newtonian limit on the Solar System scales [45, 215]. Thus, the focus of the present thesis was to probe one such regime, i.e., galactic scales, to understand the behavior of modified kinematics from the chosen gravity models.

The first part of the thesis looked into UDGs, which are galactic systems dominated by a large number of globular clusters but having low luminosity. Such galaxies are expected to contain a large amount of DM and thus become an interesting place to test the consistency of alternative gravity models. For this, we looked into a DM-dominated UDG (DF44) in the context of alternative gravity models, i.e., MOND, $f(R)$, and RGGR. Thus, by looking into such UDGs where the observational VD fits well with the DM scenario helped us to test the consistency of alternative gravity models. The phenomenology of the modified gravity models in the context of such UDGs draws a comparison with the DM-dominated scenario. To model the DF44 VD, we looked into three scenarios for the anisotropy parameter. MOND is considered the reference model to understand the influence of anisotropy on VD regarding these modified gravity models. MOND is parameterized by a single acceleration parameter, fixed globally from prior observations. In the case of $f(R)$, we assumed a general Taylor series expansion of the func-

tional form about the Minkowskian background. This assumption adds a Yukawa-like term to the Newtonian potential constrained by free parameters δ and λ. Additionally, we looked into the RGGR model, which studies the scale-dependent variation of the gravitational constant. The weak-field potential obtained for the model has a mass-dependent free parameter $\bar{\nu}$ that is constrained from the observations. These gravity models were also compared with the DM NFW scenario. The consistency of a gravity model was statistically quantified by χ^2_{red} analysis. Additionally, we have evaluated BIC to compare the favorability among different anisotropy scenarios.

In the case of MOND, a comparison of χ^2_{red} for the three anisotropy cases showed that a choice of radial profile fit poorly with the observations. This could also be observed from the difference in BIC measured between the scenarios. It was also noted that for all three gravity models, the χ^2_{red} was slightly improved or remained similar as one moved from isotropic to a constant anisotropy case. However, the difference in BIC between the two cases ($\xi = 0$ and $\xi = const$) showed that the results were inconclusive to favor one model over the other for MOND and $f(R)$. Similarly, for the RGGR model, the isotropic model had a slight edge over the tangential choice of the anisotropy parameter. For the case of the $f(R)$ model, the χ^2_{red} for isotropic versus $\xi = const$ case showed that both models fit equally well with the observations of DF44. A small difference of ΔBIC between the two scenarios showed that the result was inconclusive to favor a certain model. However, similar to MOND, the Osipkov-Merritt profile was the least favorable among the three choices of anisotropy profile. The RGGR model had a single mass-dependent parameter $\bar{\nu}$. For the isolated RGGR case, the best-fit value obtained for the parameter was an order less than constrained by the spiral or elliptical galaxies but was consistent with the mass-dependent claim of the model parameter. Also, similar to the other two gravity models, the ΔBIC measured suggested that the radial anisotropy profile was the least favorable among the three choices for the anisotropy. Finally, in this analysis, we compared our choice of gravity models with an NFW DM halo model. The comparison of BIC evaluated for each case suggested MOND as a preferred choice. However, the DM model had a slight edge over the $f(R)$ model, whereas RGGR performed equally well.

Unlike DF44, UDGs, such as DF2 and DF4, which lack DM, pave the path to study modified gravity models. The kinematics of these UDGs can be explained with normal stellar matter

without invoking the need for DM. Hence, the phenomenological study of the alternative gravity models is free from the DM properties. In this study, we have analyzed the line of sight VD for such galaxies for two alternative gravity models, i.e., $f(R)$ gravity (a chosen $f(R)$ form and a general case) and RGGR gravity. The free parameters of the gravity models were estimated using likelihood analysis. While constraining the model parameters from both UDGs, we looked into two scenarios, i.e., local and global analysis. For the former choice, to probe the phenomenology of alternative gravity models, both DF2 and DF4 were treated independently. Alternatively, as both galaxies have similar mass and size, certain parameters of the gravity model were assumed to have a global nature. The case of $f(R)$ gravity was studied from two perspectives. The first gravity model chooses a functional form $f(R)$, which adds a Yukawa-like term to the Newtonian potential similar to the case of DF44. The second choice takes an effective power law form for the $f(R)$, which resulted in a radius-dependent power term ($\propto r^{\beta}$) to the Newtonian potential. Studying the DF2 and DF4 galaxies for the two $f(R)$ local scenarios showed that the best fit VD curve lies within the 1σ region of the observation. Similarly, for the RGGR model, the free parameter of the model increases in a nearly linear manner with the mass of the galaxy. Hence, when constrained locally, the free parameter ($\bar{\nu}$) for the two UDGs was similar and was of the order 10^{-8} that is consistent with the UDG DF44. The optimized VD fitted with the free parameters also lay within the 1σ range of observations.

Similar to the local case, a phenomenological study was performed for both the UDGs, where certain parameters of the gravity model were treated globally. In the case of $f(R)$ choice, a generic model has a coupling parameter that can be global for both galaxies. Similarly, for a specific choice of $f(R) = R^n$, the power-law n was treated to be similar for DF2 and DF4. For RGGR, the model parameter $\bar{\nu}$ studied to vary with the mass linearly was considered a global parameter for galaxies such as DF2 and DF4. Using a similar technique employed in the local scenario, the phenomenology study of both gravity models showed a consistent behavior with the observational VD. Thus, all the alternative gravity models in this discussion were found to be reasonable while explaining the VD data. The analysis with the choices of alternative gravity theories suggested that these models cannot be ruled out with the present observational data precision.

In the following chapter, we studied the impact of running G on the kinematics of a collec-

tion of rotationally supported galaxies compiled in the SPARC catalog. For this, we looked into four different morphological types of galaxies, viz. early, spiral, late, and starburst contained within SPARC. We constrained the model parameter $\bar{\nu}$ for each galaxy taken from all four morphological types and found that the RGGR consistently fits the observed net circular velocity. Our statistical analysis probed this consistency for the individual galaxies using the goodness of fit. From our analysis, we concluded that the RGGR model consistently explained the RC observations for 93 galaxies. The constrained values for the parameter $\bar{\nu}$ for our sample of the SPARC galaxies lay in the range $10^{-6} - 10^{-8}$ and were consistent with the linear variation of the masses of the galaxies under consideration. This implies that the older and heavier galaxies lead to a larger $\bar{\nu}$. Indeed, we found that the parameter $\bar{\nu}$ decreases from the older galaxies to the younger ones.

Using the constrained values of free parameters, we verified the goodness of fit in light of empirical relations, RAR and BTFR, that are known to be valid for the observational data of SPARC. In particular, the RAR compared the radial variation of the observed and the baryonic acceleration. An additional factor comes in the baryonic acceleration due to the RGGR model. Our analysis found that the RAR in the RGGR framework aligns with the established analytical relation obtained from previous observations. On a similar note, BTFR compared the baryonic mass with the observed flat velocity ($V_{\rm f}$) of a galaxy, suggesting a power law dependence between them. The exact power law index was found to be sensitive to the choice of the flat velocity radius. We selected a radius of $3.2R_d$, which is known to show optimal behavior with the observations. Our analysis found a tight correlation of the baryonic mass with flat velocity measured at $3.2R_d$, which evaluates a small orthogonal scatter of 0.08. The consistent behavior of both the empirical relations in the context of the RGGR model further solidified the claim in favor of the gravity models.

Additionally, we compare the RGGR model with a DM scenario, where we assumed the profile to be NFW. Our analysis clearly showed that leaving aside where both the models perform equally well ($\Delta BIC = 0 - 2$), NFW and RGGR models behaved consistently for almost similar numbers of galaxies. An important aspect of the RGGR model was that the model parameter $\bar{\nu}$ is dependent on the mass of the gravitating system. Many other alternative gravity models exhibit dependence of the model parameters on the scale of the system. Though this scale de-

pendence of the phenomenological parameter may question the fundamental nature of these alternative gravity models, they remain a consistent theory of gravity.

Following the RGGR study, we looked into a rather global analysis for the SPARC galaxies under the assumption that YMOG governs the dynamics of the galaxies. In this study, we probed the phenomenological gravity model that introduced a Yukawa-like term to the Newtonian potential. The additional fifth force is coupled only to the DM contribution. Thus, the present model explored a mixed scenario to probe the galactic kinematics. The model introduced certain parameters that needed to be constrained from the observations. This includes local parameters such as mass-to-light ratio (γ_d, γ_b) and virial mass (M_{200}) to model DM halo. Also, the model additionally contained parameters such as β and λ that were expected to be global for a galactic system. For our analysis, we utilized the morphological divisions (early, spiral, and late-type) to randomly group the galaxies in a maximum set of 10 as allowed by the present computational capabilities. The model parameters (local and global) were constrained from the observational RC analysis. From our study, we concluded that there was a clear tension towards the global nature of the Yukawa parameters when galaxies are grouped morphologically. The early-type galaxies, having a comparatively larger size and baryonic mass, showed a large magnitude for the coupling (β) and scale parameter (λ) in contrast to late-type and starburst. It was also to be noted that the coupling parameter β being positive suggests an attractive nature to the fifth force.

Using the global values for the set of galaxies belonging to a given morphological kind, we further verified the consistency of the fit parameters using empirical relations such as RAR and BTFR. For this, we selected 63 SPARC galaxies of different morphological kinds with β and λ taken as constrained from the global RC study. Our analysis clearly showed that the RAR and BTFR, when looked into in the context of YMOG, were consistent in nature. The slope of the BTFR, although slightly larger (4.72 instead of 4), cannot rule out the model within the scope of the current analysis. As an additional test, we also compared the model using the NAV analysis that looked into the radial difference between the observations and the baryonic contribution. In the context of YMOG, this difference will constitute the contribution from the DM and the fifth-force term. Thus, a comparison of the observational NAV with the model-dependent NAV helps to verify the consistency of the model. From our analysis, we conclude that the NAV in the context of YMOG covered a broad region with a slight overlap with the observational

one. Thus, we concluded that a morphological analysis of the YMOG model, which was in sharp contrast to the global claim towards the model parameter, is consistent with the model-independent relations (i.e., RAR, BTFR, and NAV).

The thesis has investigated various choices of alternative gravity models to assess their ability to reproduce galactic dynamics. Our phenomenological analysis has revealed that the selected gravity models have provided a viable explanation of the galactic kinematics for both the large set of galaxies in SPARC and selected UDGs. Further support for these models has been established by comparing them with competing scenarios and by evaluating their consistency with empirical relations such as RAR and BTFR, particularly in the case of SPARC dataset.

References

[1] A. Einstein, The foundation of the general theory of relativity., Annalen Phys. 49 (7) (1916) 769–822. doi:10.1002/andp.19163540702.

[2] L. D. Landau, E. M. Lifschits, The Classical Theory of Fields, Vol. Volume 2 of Course of Theoretical Physics, Pergamon Press, Oxford, 1975.

[3] S. Weinberg, Gravitation and Cosmology: Principles and Applications of the General Theory of Relativity, John Wiley and Sons, New York, 1972.

[4] B. P. Abbott, et al., Observation of Gravitational Waves from a Binary Black Hole Merger, Phys. Rev. Lett. 116 (6) (2016) 061102. arXiv:1602.03837, doi:10.1103/PhysRevLett.116.061102.

[5] B. P. Abbott, et al., Tests of General Relativity with GW170817, Phys. Rev. Lett. 123 (1) (2019) 011102. arXiv:1811.00364, doi:10.1103/PhysRevLett.123.011102.

[6] K. Akiyama, et al., First M87 Event Horizon Telescope Results. I. The Shadow of the Supermassive Black Hole, Astrophys. J. Lett. 875 (2019) L1. arXiv:1906.11238, doi:10.3847/2041-8213/ab0ec7.

[7] A. G. Riess, The Expansion of the Universe is Faster than Expected, Nature Rev. Phys. 2 (1) (2019) 10–12. arXiv:2001.03624, doi:10.1038/s42254-019-0137-0.

[8] C. W. Misner, K. S. Thorne, J. A. Wheeler, Gravitation, W. H. Freeman, San Francisco, 1973.

[9] J. Earman, Bangs, crunches, whimpers, and shrieks: Singularities and acausalities in relativistic space-times, 1995.

[10] J. Berges, N. Tetradis, C. Wetterich, Nonperturbative renormalization flow in quantum field theory and statistical physics, Phys. Rept. 363 (2002) 223–386. arXiv:hep-ph/0005122, doi:10.1016/S0370-1573(01)00098-9.

[11] F. Zwicky, Die Rotverschiebung von extragalaktischen Nebeln, Helvetica Physica Acta 6 (1933) 110–127.

[12] H. W. Babcock, The rotation of the Andromeda Nebula, Lick Observatory Bulletin 498 (1939) 41–51. doi:10.5479/ADS/bib/1939LicOB.19.41B.

[13] V. C. Rubin, W. K. Ford, Rotation of the andromeda nebula from a spectroscopic survey of emission regions, The Astrophysical Journal 159 (1970) 379–403.
URL https://api.semanticscholar.org/CorpusID:122756867

[14] V. C. Rubin, N. Thonnard, W. K. Ford, Jr., Rotational properties of 21 SC galaxies with a large range of luminosities and radii, from NGC 4605 /R = 4kpc/ to UGC 2885 /R = 122 kpc/, Astrophys. J. 238 (1980) 471. doi:10.1086/158003.

[15] J. M. Shull, B. D. Smith, C. W. Danforth, The baryon census in a multiphase intergalactic medium: 30% of the baryons may still be missing, The Astrophysical Journal 759 (2011).
URL https://api.semanticscholar.org/CorpusID:119295243

[16] S. Giodini, et al., Stellar and total baryon mass fractions in groups and clusters since redshift 1, Astrophys. J. 703 (2009) 982–993. arXiv:0904.0448, doi:10.1088/0004-637X/703/1/982.

[17] P. Bull, et al., Beyond ΛCDM: Problems, solutions, and the road ahead, Phys. Dark Univ. 12 (2016) 56–99. arXiv:1512.05356, doi:10.1016/j.dark.2016.02.001.

[18] S. Weinberg, The Cosmological Constant Problem, Rev. Mod. Phys. 61 (1989) 1–23. doi:10.1103/RevModPhys.61.1.

[19] J. S. Bullock, M. Boylan-Kolchin, Small-Scale Challenges to the ΛCDM Paradigm, Ann. Rev. Astron. Astrophys. 55 (2017) 343–387. arXiv:1707.04256, doi:10.1146/annurev-astro-091916-055313.

[20] L. Perivolaropoulos, F. Skara, Challenges for ΛCDM: An update, New Astron. Rev. 95 (2022) 101659. arXiv:2105.05208, doi:10.1016/j.newar.2022.101659.

[21] P. J. E. Peebles, Status of the LambdaCDM theory: supporting evidence and anomalies, 2024. arXiv:2405.18307.

[22] W. Yin, Cosmic clues: DESI, dark energy, and the cosmological constant problem, JHEP 05 (2024) 327. arXiv:2404.06444, doi:10.1007/JHEP05(2024)327.

[23] D. H. Weinberg, J. S. Bullock, F. Governato, R. Kuzio de Naray, A. H. G. Peter, Cold dark matter: controversies on small scales, Proc. Nat. Acad. Sci. 112 (2015) 12249–12255. arXiv:1306.0913, doi:10.1073/pnas.1308716112.

[24] S. Nojiri, S. D. Odintsov, Modified gravity with negative and positive powers of the curvature: Unification of the inflation and of the cosmic acceleration, Phys. Rev. D 68 (2003) 123512. arXiv:hep-th/0307288, doi:10.1103/PhysRevD.68.123512.

[25] Y. Akrami, et al., Modified Gravity and Cosmology. An Update by the CANTATA Network, Springer, 2021. arXiv:2105.12582, doi:10.1007/978-3-030-83715-0.

[26] T. Clifton, P. G. Ferreira, A. Padilla, C. Skordis, Modified Gravity and Cosmology, Phys. Rept. 513 (2012) 1–189. arXiv:1106.2476, doi:10.1016/j.physrep.2012.01.001.

[27] W. J. G. de Blok, S. S. McGaugh, Dark matter in low surface brightness galaxies, ASP Conf. Ser. 117 (1997) 39. arXiv:astro-ph/9610216.

[28] M. Steinmetz, J. F. Navarro, The hierarchical origin of galaxy morphologies, New Astron. 7 (2002) 155–160, [Erratum: New Astron. 8, 557–564 (2003)]. arXiv:astro-ph/0202466, doi:10.1016/S1384-1076(02)00102-1.

[29] D. N. Spergel, et al., First year Wilkinson Microwave Anisotropy Probe (WMAP) observations: Determination of cosmological parameters, Astrophys. J. Suppl. 148 (2003) 175–194. arXiv:astro-ph/0302209, doi:10.1086/377226.

[30] C. Heller, I. Shlosman, L. Athanassoula, Structure Formation Inside Triaxial Dark Matter Halos: Galactic Disks, Bulges and Bars, Astrophys. J. 671 (2007) 226. arXiv:0706.3895, doi:10.1086/523260.

[31] L. E. Strigari, Galactic Searches for Dark Matter, Phys. Rept. 531 (2013) 1–88. arXiv:1211.7090, doi:10.1016/j.physrep.2013.05.004.

[32] P. Salucci, The distribution of dark matter in galaxies, Astron. Astrophys. Rev. 27 (1) (2019) 2. arXiv:1811.08843, doi:10.1007/s00159-018-0113-1.

[33] A. M. Green, Dark matter in astrophysics/cosmology, SciPost Phys. Lect. Notes 37 (2022) 1. arXiv:2109.05854, doi:10.21468/SciPostPhysLectNotes.37.

[34] M. Khelashvili, A. Rudakovskyi, S. Hossenfelder, Dark matter profiles of SPARC galaxies: a challenge to fuzzy dark matter, Mon. Not. Roy. Astron. Soc. 523 (3) (2023) 3393–3405. arXiv:2207.14165, doi:10.1093/mnras/stad1595.

[35] V. C. Rubin, W. K. Ford, Jr., N. Thonnard, Rotational properties of 21 SC galaxies with a large range of luminosities and radii, from NGC 4605 (R=4kpc) to UGC 2885 (R=122kpc)., 238 (1980) 471–487. doi:10.1086/158003.

[36] J. F. Navarro, C. S. Frenk, S. D. M. White, The Structure of cold dark matter halos, Astrophys. J. 462 (1996) 563–575. arXiv:astro-ph/9508025, doi:10.1086/177173.

[37] W. De Blok, et al., The core-cusp problem, Advances in Astronomy 2010 (2010).

[38] A. Di Cintio, C. B. Brook, A. A. Dutton, A. V. Macciò, G. S. Stinson, A. Knebe, A mass-dependent density profile for dark matter haloes including the influence of galaxy formation, Mon. Not. Roy. Astron. Soc. 441 (4) (2014) 2986–2995. arXiv:1404.5959, doi:10.1093/mnras/stu729.

[39] H. Katz, F. Lelli, S. S. McGaugh, A. D. Cintio, C. B. Brook, J. M. Schombert, Testing feedback-modified dark matter haloes with galaxy rotation curves: estimation of halo parameters and consistency with λcdm scaling relations, Monthly Notices of the Royal Astronomical Society 466 (2016) 1648–1668.
URL https://api.semanticscholar.org/CorpusID:51846356

[40] F. Allaert, G. Gentile, M. B. S. Observatorium, U. Gent, D. of Physics, Astrophysics, V. U. Brussel, Testing baryon-induced core formation in lambda cdm: A comparison of the dc14 and corenfw dark matter halo models on galaxy rotation curves, arXiv: Astrophysics of Galaxies (2017).
URL https://api.semanticscholar.org/CorpusID:59442386

[41] P. Li, F. Lelli, S. McGaugh, J. Schombert, A comprehensive catalog of dark matter halo models for SPARC galaxies, Astrophys. J. Suppl. 247 (1) (2020) 31. arXiv:2001.10538, doi:10.3847/1538-4365/ab700e.

[42] A. Burkert, The Structure of dark matter halos in dwarf galaxies, Astrophys. J. Lett. 447 (1995) L25. arXiv:astro-ph/9504041, doi:10.1086/309560.

[43] A. Burkert, The Structure and evolution of weakly selfinteracting cold dark matter halos, Astrophys. J. Lett. 534 (2000) L143–L146. arXiv:astro-ph/0002409, doi:10.1086/312674.

[44] H.-N. Lin, X. Li, The dark matter profiles in the milky way, Monthly Notices of the Royal Astronomical Society (2019).
URL https://api.semanticscholar.org/CorpusID:195218807

[45] S. Shankaranarayanan, J. P. Johnson, Modified theories of gravity: Why, how and what?, Gen. Rel. Grav. 54 (5) (2022) 44. arXiv:2204.06533, doi:10.1007/s10714-022-02927-2.

[46] G. Nordstrom, On the possibility of unifying the electromagnetic and the gravitational fields, Phys. Z. 15 (1914) 504–506. arXiv:physics/0702221.

[47] J. M. Overduin, P. S. Wesson, Kaluza-Klein gravity, Phys. Rept. 283 (1997) 303–380. arXiv:gr-qc/9805018, doi:10.1016/S0370-1573(96)00046-4.

[48] H. Weyl, Gravitation und Elektrizität, Sitzungsberichte der Königlich Preussischen Akademie der Wissenschaften (1918) 465–478doi:10.1007/978-3-663-19510-8_11.

[49] E. Cartan, Sur les variétés à connexion affine et la théorie de la relativité généralisée. (première partie), Annales Sci. Ecole Norm. Sup. 40 (1923) 325–412.

[50] A. Trautman, Einstein-Cartan theory (6 2006). arXiv:gr-qc/0606062.

[51] C. Brans, R. H. Dicke, Mach's principle and a relativistic theory of gravitation, Phys. Rev. 124 (1961) 925–935. doi:10.1103/PhysRev.124.925.

[52] C. H. Brans, The Roots of scalar-tensor theory: An Approximate history, in: Santa Clara 2004: 1st International Workshop on Gravitation and Cosmology, 2005. arXiv:gr-qc/0506063.

[53] K. S. Stelle, Classical Gravity with Higher Derivatives, Gen. Rel. Grav. 9 (1978) 353–371. doi:10.1007/BF00760427.

[54] S. Nojiri, S. D. Odintsov, Introduction to modified gravity and gravitational alternative for dark energy, eConf C0602061 (2006) 06. arXiv:hep-th/0601213, doi:10.1142/S0219887807001928.

[55] S. Nojiri, S. D. Odintsov, V. K. Oikonomou, Modified Gravity Theories on a Nutshell: Inflation, Bounce and Late-time Evolution, Phys. Rept. 692 (2017) 1–104. arXiv:1705.11098, doi:10.1016/j.physrep.2017.06.001.

[56] D. Lovelock, The Einstein tensor and its generalizations, J. Math. Phys. 12 (1971) 498–501. doi:10.1063/1.1665613.

[57] L. Amendola, S. Tsujikawa, Dark Energy: Theory and Observations, 2010.

[58] A. Joyce, B. Jain, J. Khoury, M. Trodden, Beyond the Cosmological Standard Model, Phys. Rept. 568 (2015) 1–98. arXiv:1407.0059, doi:10.1016/j.physrep.2014.12.002.

[59] K. Koyama, Cosmological Tests of Modified Gravity, Rept. Prog. Phys. 79 (4) (2016) 046902. arXiv:1504.04623, doi:10.1088/0034-4885/79/4/046902.

[60] J. C. Fabris, P. L. C. de Oliveira, D. C. Rodrigues, A. M. Velasquez-Toribio, I. L. Shapiro, Quantum corrections to gravity and their implications for cosmology and astrophysics, Int. J. Mod. Phys. A 27 (2012) 1260006. arXiv:1203.2695, doi:10.1142/S0217751X12600068.

[61] M. Reuter, H. Weyer, Quantum gravity at astrophysical distances?, JCAP 12 (2004) 001. arXiv:hep-th/0410119, doi:10.1088/1475-7516/2004/12/001.

[62] A. E. Evrard, C. A. Metzler, J. F. Navarro, Mass estimates of X-ray clusters, Astrophys. J. 469 (1996) 494. arXiv:astro-ph/9510058, doi:10.1086/177798.

[63] B. Famaey, S. McGaugh, Modified Newtonian Dynamics (MOND): Observational Phenomenology and Relativistic Extensions, Living Rev. Rel. 15 (2012) 10. arXiv:1112.3960, doi:10.12942/lrr-2012-10.

[64] M. Cataneo, D. Rapetti, F. Schmidt, A. B. Mantz, S. W. Allen, D. E. Applegate, P. L. Kelly, A. von der Linden, R. G. Morris, New constraints on $f(R)$ gravity from clusters

of galaxies, Phys. Rev. D 92 (4) (2015) 044009. arXiv:1412.0133, doi:10.1103/PhysRevD.92.044009.

[65] C. Arnold, M. Leo, B. Li, Realistic simulations of galaxy formation in $f(R)$ modified gravity, Nature Astron. 3 (10) (2019) 945–954. arXiv:1907.02977, doi:10.1038/s41550-019-0823-y.

[66] I. De Martino, f(R) -gravity model of the Sunyaev-Zeldovich profile of the Coma cluster compatible with Planck data, Phys. Rev. D 93 (12) (2016) 124043. arXiv:1605.08223, doi:10.1103/PhysRevD.93.124043.

[67] S. S. McGaugh, G. D. Bothun, J. M. Schombert, Galaxy selection and the surface brightness distribution, Astron. J. 110 (1995) 573. arXiv:astro-ph/9505062, doi:10.1086/117543.

[68] S. Capozziello, V. F. Cardone, A. Troisi, Low surface brightness galaxies rotation curves in the low energy limit of r**n gravity: no need for dark matter?, Mon. Not. Roy. Astron. Soc. 375 (2007) 1423–1440. arXiv:astro-ph/0603522, doi:10.1111/j.1365-2966.2007.11401.x.

[69] J. R. Brownstein, J. W. Moffat, Galaxy rotation curves without non-baryonic dark matter, Astrophys. J. 636 (2006) 721–741. arXiv:astro-ph/0506370, doi:10.1086/498208.

[70] S. Capozziello, M. De Laurentis, V. Faraoni, A Bird's eye view of f(R)-gravity, Open Astron. J. 3 (2010) 49. arXiv:0909.4672, doi:10.2174/1874381101003020049.

[71] L. Lombriser, N. A. Lima, Challenges to Self-Acceleration in Modified Gravity from Gravitational Waves and Large-Scale Structure, Phys. Lett. B 765 (2017) 382–385. arXiv:1602.07670, doi:10.1016/j.physletb.2016.12.048.

[72] J. Sakstein, B. Jain, Implications of the Neutron Star Merger GW170817 for Cosmological Scalar-Tensor Theories, Phys. Rev. Lett. 119 (25) (2017) 251303. arXiv:1710.05893, doi:10.1103/PhysRevLett.119.251303.

[73] J. M. Ezquiaga, M. Zumalacárregui, Dark Energy After GW170817: Dead Ends and the Road Ahead, Phys. Rev. Lett. 119 (25) (2017) 251304. arXiv:1710.05901, doi:10.1103/PhysRevLett.119.251304.

[74] M. Milgrom, A modification of the newtonian dynamics: Implications for galaxies, The Astrophysical Journal 270 (1983) 371–383.
URL https://api.semanticscholar.org/CorpusID:120294448

[75] K.-H. Chae, F. Lelli, H. Desmond, S. S. McGaugh, P. Li, J. M. Schombert, Testing the Strong Equivalence Principle: Detection of the External Field Effect in Rotationally Supported Galaxies, Astrophys. J. 904 (1) (2020) 51, [Erratum: Astrophys.J. 910, 81 (2021)]. arXiv:2009.11525, doi:10.3847/1538-4357/abbb96.

[76] K.-H. Chae, Distinguishing Dark Matter, Modified Gravity, and Modified Inertia with the Inner and Outer Parts of Galactic Rotation Curves, Astrophys. J. 941 (1) (2022) 55. arXiv:2207.11069, doi:10.3847/1538-4357/ac93fc.

[77] H. Haghi, P. Kroupa, I. Banik, X. Wu, A. H. Zonoozi, B. Javanmardi, A. Ghari, O. Müller, J. Dabringhausen, H. Zhao, A new formulation of the external field effect in mond and numerical simulations of ultra-diffuse dwarf galaxies – application to ngc 1052-df2 and ngc 1052-df4, Monthly Notices of the Royal Astronomical Society (2019).
URL https://api.semanticscholar.org/CorpusID:182953046

[78] A. A. Starobinsky, The Perturbation Spectrum Evolving from a Nonsingular Initially De-Sitter Cosmology and the Microwave Background Anisotropy, Sov. Astron. Lett. 9 (1983) 302.

[79] W. Hu, I. Sawicki, Models of f(R) Cosmic Acceleration that Evade Solar-System Tests, Phys. Rev. D 76 (2007) 064004. arXiv:0705.1158, doi:10.1103/PhysRevD.76.064004.

[80] R. P. Woodard, Avoiding dark energy with 1/r modifications of gravity, Lect. Notes Phys. 720 (2007) 403–433. arXiv:astro-ph/0601672, doi:10.1007/978-3-540-71013-4_14.

[81] R. H. Sanders, S. S. McGaugh, Modified Newtonian dynamics as an alternative to dark matter, Ann. Rev. Astron. Astrophys. 40 (2002) 263–317. arXiv:astro-ph/0204521, doi:10.1146/annurev.astro.40.060401.093923.

[82] F. Piazza, C. Marinoni, Model for gravitational interaction between dark matter and

baryons, Phys. Rev. Lett. 91 (2003) 141301. doi:10.1103/PhysRevLett.91.141301. URL https://link.aps.org/doi/10.1103/PhysRevLett.91.141301

[83] A. O. F. de Almeida, L. Amendola, V. Niro, Galaxy rotation curves in modified gravity models, JCAP 08 (2018) 012. arXiv:1805.11067, doi:10.1088/1475-7516/2018/08/012.

[84] K. G. Wilson, J. B. Kogut, The Renormalization group and the epsilon expansion, Phys. Rept. 12 (1974) 75–199. doi:10.1016/0370-1573(74)90023-4.

[85] S. Weinberg, ULTRAVIOLET DIVERGENCES IN QUANTUM THEORIES OF GRAVITATION, 1980, pp. 790–831.

[86] I. L. Shapiro, J. Sola, Scaling behavior of the cosmological constant: Interface between quantum field theory and cosmology, JHEP 02 (2002) 006. arXiv:hep-th/0012227, doi:10.1088/1126-6708/2002/02/006.

[87] I. L. Shapiro, J. Sola, C. Espana-Bonet, P. Ruiz-Lapuente, Variable cosmological constant as a Planck scale effect, Phys. Lett. B 574 (2003) 149–155. arXiv:astro-ph/0303306, doi:10.1016/j.physletb.2003.09.016.

[88] I. L. Shapiro, Effective Action of Vacuum: Semiclassical Approach, Class. Quant. Grav. 25 (2008) 103001. arXiv:0801.0216, doi:10.1088/0264-9381/25/10/103001.

[89] D. C. Rodrigues, P. S. Letelier, I. L. Shapiro, Galaxy rotation curves from General Relativity with Renormalization Group corrections, JCAP 04 (1) (2010) 020. arXiv:0911.4967, doi:10.1088/1475-7516/2010/04/020.

[90] P. Brax, Screening mechanisms in modified gravity, Class. Quant. Grav. 30 (2013) 214005. doi:10.1088/0264-9381/30/21/214005.

[91] J. Sakstein, Astrophysical tests of screened modified gravity, Int. J. Mod. Phys. D 27 (15) (2018) 1848008. arXiv:2002.04194, doi:10.1142/S0218271818480085.

[92] A. P. Naik, E. Puchwein, A.-C. Davis, D. Sijacki, H. Desmond, Constraints on Chameleon f(R)-Gravity from Galaxy Rotation Curves of the SPARC Sample, Mon. Not. Roy. Astron. Soc. 489 (1) (2019) 771–787. arXiv:1905.13330, doi:10.1093/mnras/stz2131.

[93] P. Brax, S. Casas, H. Desmond, B. Elder, Testing Screened Modified Gravity, Universe 8 (1) (2021) 11. arXiv:2201.10817, doi:10.3390/universe8010011.

[94] S. S. McGaugh, F. Lelli, J. M. Schombert, Radial acceleration relation in rotationally supported galaxies, Physical Review Letters 117 (20) (2016) 201101.

[95] S. S. McGaugh, The Baryonic Tully-Fisher relation of galaxies with extended rotation curves and the stellar mass of rotating galaxies, Astrophys. J. 632 (2005) 859–871. arXiv:astro-ph/0506750, doi:10.1086/432968.

[96] P. van Dokkum, R. Abraham, J. Brodie, C. Conroy, S. Danieli, A. Merritt, L. Mowla, A. Romanowsky, J. Zhang, A High Stellar Velocity Dispersion and ∼100 Globular Clusters for the Ultra-diffuse Galaxy Dragonfly 44, Astrophys. J. Lett. 828 (1) (2016) L6. arXiv:1606.06291, doi:10.3847/2041-8205/828/1/L6.

[97] P. van Dokkum, R. Abraham, A. Merritt, J. Zhang, M. Geha, C. Conroy, Forty-Seven Milky Way-Sized, Extremely Diffuse Galaxies in the Coma Cluster, Astrophys. J. Lett. 798 (2) (2015) L45. arXiv:1410.8141, doi:10.1088/2041-8205/798/2/L45.

[98] P. van Dokkum, S. Danieli, R. Abraham, C. Conroy, A. J. Romanowsky, A second galaxy missing dark matter in the NGC 1052 group, The Astrophysical Journal 874 (1) (2019) L5. doi:10.3847/2041-8213/ab0d92.
URL https://doi.org/10.38472F2041-82132Fab0d92

[99] D. C. Rodrigues, A. Hernandez-Arboleda, A. Wojnar, Normalized additional velocity distribution: Testing the radial profile of dark matter halos and MOND, Phys. Dark Univ. 41 (2023) 101230. arXiv:2204.03762, doi:10.1016/j.dark.2023.101230.

[100] J. Binney, S. Tremaine, Galactic Dynamics: Second Edition, rev - revised, 2 Edition, Princeton University Press, 2008.
URL http://www.jstor.org/stable/j.ctvc778ff

[101] T. Padmanabhan, Theoretical Astrophysics - Volume 2, Stars and Stellar Systems, Vol. 2, 2001. doi:10.2277/0521562414.

[102] W. E. Harris, G. L. H. Harris, M. Alessi, A Catalog of Globular Cluster Systems: What Determines the Size of a Galaxy's Globular Cluster Population?, Astrophys. J. 772 (2013) 82. arXiv:1306.2247, doi:10.1088/0004-637X/772/2/82.

[103] M. A. Beasley, I. Trujillo, Globular clusters indicate that ultra-diffuse galaxies are dwarfs, The Astrophysical Journal 830 (2016).
URL https://api.semanticscholar.org/CorpusID:43278454

[104] E. W. Peng, S. L. P. University, K. I. for Astronomy, Astrophysics, A rich globular cluster system in dragonfly 17: Are ultra-diffuse galaxies pure stellar halos?, The Astrophysical Journal Letters 822 (2016).
URL https://api.semanticscholar.org/CorpusID:119279033

[105] P. van Dokkum, et al., A galaxy lacking dark matter, Nature 555 (7698) (2018) 629–632. arXiv:1803.10237, doi:10.1038/nature25767.

[106] T. Islam, K. Dutta, Modified Gravity Theories in Light of the Anomalous Velocity Dispersion of NGC1052-DF2, Phys. Rev. D 100 (10) (2019) 104049. arXiv:1908.07160, doi:10.1103/PhysRevD.100.104049.

[107] E. Laudato, V. Salzano, DHOST gravity in ultra-diffuse galaxies—Part II: NGC 1052-DF4 and Dragonfly 44, Eur. Phys. J. C 83 (5) (2023) 402. arXiv:2211.08839, doi:10.1140/epjc/s10052-023-11564-1.

[108] E. Laudato, V. Salzano, DHOST gravity in ultra-diffuse galaxies – part I: the case of NGC1052-DF2, Eur. Phys. J. C 82 (10) (2022) 935. arXiv:2206.06284, doi:10.1140/epjc/s10052-022-10901-0.

[109] F. Bouchè, S. Capozziello, C. De Simone, V. Salzano, Testing non-local gravity through Ultra-Diffuse Galaxies kinematics, Phys. Dark Univ. 46 (2024) 101579. arXiv:2407.18084, doi:10.1016/j.dark.2024.101579.

[110] A. W. Graham, S. P. Driver, A Concise reference to (projected) Sersic R**1/n quantities, including concentration, profile slopes, Petrosian indices, and Kron magnitudes, Publ. Astron. Soc. Austral. 22 (2005) 118. arXiv:astro-ph/0503176, doi:10.1071/AS05001.

[111] P. van Dokkum, A. Wasserman, S. Danieli, R. Abraham, J. Brodie, C. Conroy, D. A. Forbes, C. Martin, M. Matuszewski, A. J. Romanowsky, et al., Spatially resolved stellar kinematics of the ultra-diffuse galaxy dragonfly 44. i. observations, kinematics, and cold dark matter halo fits, The Astrophysical Journal 880 (2) (2019) 91.

[112] T. Islam, Enigmatic velocity dispersions of ultradiffuse galaxies in light of modified gravity theories and the radial acceleration relation, Phys. Rev. D 102 (2) (2020) 024068. arXiv:1910.09726, doi:10.1103/PhysRevD.102.024068.

[113] J. Freundlich, B. Famaey, P.-A. Oria, M. Bílek, O. Müller, R. Ibata, Probing the radial acceleration relation and the strong equivalence principle with the coma cluster ultra-diffuse galaxies, Astronomy & Astrophysics 658 (2022) A26.

[114] S. T. Nagesh, J. Freundlich, B. Famaey, M. B'ilek, G. Candlish, R. Ibata, O. Muller, Simulations of cluster ultra-diffuse galaxies in mond, Astronomy & Astrophysics (2024). URL https://api.semanticscholar.org/CorpusID:271039723

[115] G. A. Mamon, E. L. Lokas, Confronting lambda-CDM with the optical observations of elliptical galaxies. 2. Weighing the dark matter component, Mon. Not. Roy. Astron. Soc. 363 (2005) 705–722, [Addendum: Mon.Not.Roy.Astron.Soc. 370, 1582 (2006)]. arXiv:astro-ph/0405491, doi:10.1111/j.1365-2966.2005.09400.x.

[116] L. L. Watkins, N. W. Evans, J. A. IoA, Cambridge, Nao, Beijing, China., The masses of the milky way and andromeda galaxies, Monthly Notices of the Royal Astronomical Society 406 (2010) 264–278.
URL https://api.semanticscholar.org/CorpusID:55869707

[117] J. N. Bahcall, S. Tremaine, Methods for determining the masses of spherical systems. I. Test particles around a point mass., The Astrophysical Journal 244 (1981) 805–819. doi:10.1086/158756.

[118] M. Bílek, O. Müller, B. Famaey, Discussing the first velocity dispersion profile of an ultra-diffuse galaxy in MOND, Astron. Astrophys. 627 (2019) L1. arXiv:1906.01631, doi:10.1051/0004-6361/201935840.

[119] J. W. Moffat, V. T. Toth, NGC 1052-DF2 And Modified Gravity (MOG) Without Dark Matter, Mon. Not. Roy. Astron. Soc. 482 (1) (2019) L1–L3. arXiv:1805.01117, doi:10.1093/mnrasl/sly176.

[120] F. Lelli, S. S. McGaugh, J. M. Schombert, SPARC: Mass Models for 175 Disk Galaxies with Spitzer Photometry and Accurate Rotation Curves, Astron. J. 152 (2016) 157. arXiv:1606.09251, doi:10.3847/0004-6256/152/6/157.

[121] D. Mihalas, J. Binney, Galactic Astronomy: Structure and Kinematics, W.H. Freeman, 1981.
URL https://books.google.co.in/books?id=aT2fQgAACAAJ

[122] M. H. Chan, C. Fai Yeung, Model-independent Constraints on Ultralight Dark Matter from the SPARC Data, The Astrophysical Journal 913 (1) (2021) 25. arXiv:2104.05159, doi:10.3847/1538-4357/abf42f.

[123] K.-H. Chae, H. Desmond, F. Lelli, S. S. McGaugh, J. M. Schombert, Testing the Strong Equivalence Principle. II. Relating the External Field Effect in Galaxy Rotation Curves to the Large-scale Structure of the Universe, The Astrophysical Journal 921 (2) (2021) 104. arXiv:2109.04745, doi:10.3847/1538-4357/ac1bba.

[124] L. Wang, D.-M. Chen, Comparison of Modeling SPARC spiral galaxies' rotation curves: halo models vs. MOND, Research in Astronomy and Astrophysics 21 (11) (2021) 271. arXiv:2008.04795, doi:10.1088/1674-4527/21/11/271.

[125] N. Bar, K. Blum, C. Sun, Galactic rotation curves versus ultralight dark matter: A systematic comparison with SPARC data, Physical Review D 105 (8) (2022) 083015. arXiv:2111.03070, doi:10.1103/PhysRevD.105.083015.

[126] K.-H. Chae, F. Lelli, H. Desmond, S. S. McGaugh, J. M. Schombert, Testing modified gravity theories with numerical solutions of the external field effect in rotationally supported galaxies, Physical Review D 106 (10) (2022) 103025. arXiv:2209.07357, doi:10.1103/PhysRevD.106.103025.

[127] C. R. Argüelles, S. Collazo, Galaxy Rotation Curve Fitting Using Machine Learning Tools, Universe 9 (8) (2023) 372. arXiv:2308.08420, doi:10.3390/universe9080372.

[128] M. H. Chan, K. Chung Law, A severe challenge to the MOND phenomenology in our Galaxy, arXiv e-prints (2023) arXiv:2309.05252arXiv:2309.05252, doi:10.48550/arXiv.2309.05252.

[129] S. Natalia Cisneros, R. Ott, M. Crowley, A. Roberts, M. Paz, Z. Brown, L. Joyal, R. Real Rico, E. Gutierrez-Gutierrez, P. Pham, Z. Holland, A. Livingston, L. Castrellon, S. Graham, S. J. Rubin, A. Ashleya, D. Battaglia, D. Lopez, M. Salwa, Rota-

tion Curve Fitting Model, arXiv e-prints (2023) arXiv:2310.04372arXiv:2310.04372, doi:10.48550/arXiv.2310.04372.

[130] M. Khelashvili, A. Rudakovskyi, S. Hossenfelder, SPARC galaxies prefer Dark Matter over MOND, arXiv e-prints (2024) arXiv:2401.10202arXiv:2401.10202, doi:10.48550/arXiv.2401.10202.

[131] W. El Hanafy, M. Hashim, G. G. L. Nashed, Revisiting flat rotation curves in Chern-Simons modified gravity, Physics Letters B 856 (2024) 138882. arXiv:2407.14122, doi:10.1016/j.physletb.2024.138882.

[132] M. Crăciun, T. Harko, Testing Weyl geometric gravity with the SPARC galactic rotation curves database, Physics of the Dark Universe 43 (2024) 101423. arXiv:2311.16893, doi:10.1016/j.dark.2024.101423.

[133] K. C. Freeman, On the disks of spiral and SO Galaxies, Astrophys. J. 160 (1970) 811. doi:10.1086/150474.

[134] L. Hernquist, An analytical model for spherical galaxies and bulges, The Astrophysical Journal 356 (1990) 359–364.
URL https://api.semanticscholar.org/CorpusID:122140408

[135] S. S. McGaugh, J. M. Schombert, Weighing galaxy disks with the baryonic tully–fisher relation, The Astrophysical Journal 802 (2015).
URL https://api.semanticscholar.org/CorpusID:51838921

[136] W. J. G. de Blok, S. S. McGaugh, The dark and visible matter content of low surface brightness disc galaxies, Monthly Notices of the Royal Astronomical Society 290 (1997) 533–552.
URL https://api.semanticscholar.org/CorpusID:10383298

[137] F. Lelli, S. S. McGaugh, J. M. Schombert, The small scatter of the baryonic tully–fisher relation, The Astrophysical Journal Letters 816 (2015).
URL https://api.semanticscholar.org/CorpusID:51855908

[138] P. Li, F. Lelli, S. McGaugh, J. Schombert, Fitting the radial acceleration relation to individual SPARC galaxies, Astron. Astrophys. 615 (2018) A3. arXiv:1803.00022, doi:10.1051/0004-6361/201732547.

[139] M. A. Green, J. W. Moffat, J. W. Moffat, Modified gravity (mog) fits to observed radial acceleration of sparc galaxies, Physics of the Dark Universe (2019).
URL https://api.semanticscholar.org/CorpusID:162184005

[140] V. Marra, D. C. Rodrigues, Á. O. F. de Almeida, A fundamental test for mond, Monthly Notices of the Royal Astronomical Society (2020).
URL https://api.semanticscholar.org/CorpusID:211069253

[141] X. Li, S.-P. Zhao, H.-N. Lin, Y. Zhou, Probing the universality of acceleration scale in modified newtonian dynamics with sparc galaxies, Chinese Physics C 45 (2020).
URL https://api.semanticscholar.org/CorpusID:229395519

[142] T. Islam, K. Dutta, Acceleration relations in the milky way as differentiators of modified gravity theories, Physical Review D (2019).
URL https://api.semanticscholar.org/CorpusID:216216166

[143] F. Lelli, S. S. McGaugh, J. M. Schombert, H. Desmond, H. Katz, The baryonic Tully–Fisher relation for different velocity definitions and implications for galaxy angular momentum, Mon. Not. Roy. Astron. Soc. 484 (3) (2019) 3267–3278. arXiv:1901.05966, doi:10.1093/mnras/stz205.

[144] G. Alestas, I. Antoniou, L. Perivolaropoulos, Hints for a Gravitational Transition in Tully–Fisher Data, Universe 7 (10) (2021) 366. arXiv:2104.14481, doi:10.3390/universe7100366.

[145] S. S. McGaugh, The baryonic tully–fisher relation of gas-rich galaxies as a test of λcdm and mond, The Astronomical Journal 143 (2011).
URL https://api.semanticscholar.org/CorpusID:38472632

[146] E. Papastergis, E. A. K. Adams, J. M. van der Hulst Kapteyn Astronomical Institute, Astron, An accurate measurement of the baryonic tully-fisher relation with heavily gas-dominated alfalfa galaxies, Astronomy and Astrophysics 593 (2016).
URL https://api.semanticscholar.org/CorpusID:17314711

[147] M. Milgrom, R. H. Sanders, MOND and the 'Dearth of dark matter in ordinary elliptical galaxies', Astrophys. J. Lett. 599 (2003) L25–L28. arXiv:astro-ph/0309617, doi:10.1086/381138.

[148] J. D. Bekenstein, Relativistic gravitation theory for the MOND paradigm, Phys. Rev. D 70 (2004) 083509, [Erratum: Phys.Rev.D 71, 069901 (2005)]. arXiv:astro-ph/0403694, doi:10.1103/PhysRevD.70.083509.

[149] J.-P. Bruneton, G. Esposito-Farese, Field-theoretical formulations of MOND-like gravity, Phys. Rev. D 76 (2007) 124012, [Erratum: Phys.Rev.D 76, 129902 (2007)]. arXiv:0705.4043, doi:10.1103/PhysRevD.76.129902.

[150] P. Kroupa, et al., Asymmetrical tidal tails of open star clusters: stars crossing their cluster's prah challenge Newtonian gravitation, Mon. Not. Roy. Astron. Soc. 517 (3) (2022) 3613–3639. arXiv:2210.13472, doi:10.1093/mnras/stac2563.

[151] K.-H. Chae, Breakdown of the Newton–Einstein Standard Gravity at Low Acceleration in Internal Dynamics of Wide Binary Stars, Astrophys. J. 952 (2) (2023) 128, [Erratum: Astrophys.J. 956, 69 (2023)]. arXiv:2305.04613, doi:10.3847/1538-4357/ace101.

[152] I. Banik, C. Pittordis, W. Sutherland, B. Famaey, R. Ibata, S. Mieske, H. Zhao, Strong constraints on the gravitational law from $gaia$ dr3 wide binaries, 2023.
URL https://api.semanticscholar.org/CorpusID:265043163

[153] C. M. Will, The Confrontation between general relativity and experiment, Living Rev. Rel. 4 (2001) 4. arXiv:gr-qc/0103036, doi:10.12942/lrr-2001-4.

[154] R. H. Sanders, Anti-gravity and galaxy rotation curves, AAP 136 (2) (1984) L21–L23.

[155] J. Scherk, ANTIGRAVITY: A CRAZY IDEA?, Phys. Lett. B 88 (1979) 265–267. doi:10.1016/0370-2693(79)90463-5.

[156] J. W. Moffat, Scalar-tensor-vector gravity theory, JCAP 03 (2006) 004. arXiv:gr-qc/0506021, doi:10.1088/1475-7516/2006/03/004.

[157] J. L. Cervantes-Cota, M. A. Rodriguez-Meza, D. Nunez, Flat rotation curves using scalar-tensor theories, J. Phys. Conf. Ser. 91 (2007) 012007. arXiv:0707.2692, doi:10.1088/1742-6596/91/1/012007.

[158] T. Clifton, The Parameterised Post-Newtonian Limit of Fourth-Order Theories of Gravity, Phys. Rev. D 77 (2008) 024041. arXiv:0801.0983, doi:10.1103/PhysRevD.77.024041.

[159] T. Clifton, M. Banados, C. Skordis, The Parameterised Post-Newtonian Limit of Bimetric Theories of Gravity, Class. Quant. Grav. 27 (2010) 235020. arXiv:1006.5619, doi:10.1088/0264-9381/27/23/235020.

[160] J. W. Moffat, S. Rahvar, The MOG weak field approximation and observational test of galaxy rotation curves, Mon. Not. Roy. Astron. Soc. 436 (2013) 1439–1451. arXiv:1306.6383, doi:10.1093/mnras/stt1670.

[161] F. Piazza, C. Marinoni, Model for gravitational interaction between dark matter and baryons, Phys. Rev. Lett. 91 (2003) 141301. arXiv:hep-ph/0304228, doi:10.1103/PhysRevLett.91.141301.

[162] V. Faraoni, f(r) gravity: successes and challenges, arXiv: General Relativity and Quantum Cosmology (2008).
URL https://api.semanticscholar.org/CorpusID:16207102

[163] S. Capozziello, V. F. Cardone, M. Francaviglia, f(R) Theories of gravity in Palatini approach matched with observations, Gen. Rel. Grav. 38 (2006) 711–734. arXiv:astro-ph/0410135, doi:10.1007/s10714-006-0261-x.

[164] A. Borowiec, W. Godlowski, M. Szydlowski, Accelerated cosmological models in modified gravity tested by distant supernovae snia data, Phys. Rev. D 74 (2006) 043502. arXiv:astro-ph/0602526, doi:10.1103/PhysRevD.74.043502.

[165] M. Lubini, C. Tortora, J. Naf, P. Jetzer, S. Capozziello, Probing the dark matter issue in f(R)-gravity via gravitational lensing, Eur. Phys. J. C 71 (2011) 1834. arXiv:1104.2851, doi:10.1140/epjc/s10052-011-1834-8.

[166] A. Hernandez-Arboleda, D. C. Rodrigues, J. D. Toniato, A. Wojnar, Palatini f(R) gravity tests in weak field limit: Solar system, seismology and galaxies, Int. J. Geom. Meth. Mod. Phys. 20 (Supp01) (2023) 2450028. arXiv:2306.04475, doi:10.1142/S0219887824500282.

[167] H. Wilcox, R. C. Nichol, G.-B. Zhao, D. Bacon, K. Koyama, A. K. Romer, Simulation tests of galaxy cluster constraints on chameleon gravity, Mon. Not. Roy. Astron. Soc. 462 (1) (2016) 715–725. arXiv:1603.05911, doi:10.1093/mnras/stw1617.

[168] S. Capozziello, E. De Filippis, V. Salzano, Modelling clusters of galaxies by f(R)-gravity, Mon. Not. Roy. Astron. Soc. 394 (2009) 947–959. arXiv:0809.1882, doi:10.1111/j.1365-2966.2008.14382.x.

[169] B. Jain, V. Vikram, J. Sakstein, Astrophysical Tests of Modified Gravity: Constraints from Distance Indicators in the Nearby Universe, Astrophys. J. 779 (2013) 39. arXiv:1204.6044, doi:10.1088/0004-637X/779/1/39.

[170] L. Xu, Constraints on $f(r)$ gravity through the redshift space distortion, Phys. Rev. D 91 (2015) 063008. doi:10.1103/PhysRevD.91.063008.
URL https://link.aps.org/doi/10.1103/PhysRevD.91.063008

[171] V. Vikram, J. Sakstein, C. Davis, A. Neil, Astrophysical Tests of Modified Gravity: Stellar and Gaseous Rotation Curves in Dwarf Galaxies, Phys. Rev. D 97 (10) (2018) 104055. arXiv:1407.6044, doi:10.1103/PhysRevD.97.104055.

[172] S. Capozziello, V. F. Cardone, A. Troisi, Reconciling dark energy models with $f(r)$ theories, Phys. Rev. D 71 (2005) 043503. doi:10.1103/PhysRevD.71.043503.
URL https://link.aps.org/doi/10.1103/PhysRevD.71.043503

[173] S. Capozziello, A. Stabile, A. Troisi, A General solution in the Newtonian limit of f(R)-gravity, Mod. Phys. Lett. A 24 (2009) 659–665. arXiv:0901.0448, doi:10.1142/S0217732309030382.

[174] A. Stabile, S. Capozziello, Galaxy rotation curves in f(R,ϕ) gravity, Phys. Rev. D 87 (6) (2013) 064002. arXiv:1302.1760, doi:10.1103/PhysRevD.87.064002.

[175] N. R. Napolitano, S. Capozziello, A. J. Romanowsky, M. Capaccioli, C. Tortora, Testing Yukawa-like potentials from f(R)-gravity in elliptical galaxies, Astrophys. J. 748 (2012) 87. arXiv:1201.3363, doi:10.1088/0004-637X/748/2/87.

[176] S. Capozziello, V. F. Cardone, A. Troisi, Dark energy and dark matter as curvature effects, JCAP 08 (1) (2006) 001. arXiv:astro-ph/0602349, doi:10.1088/1475-7516/2006/08/001.

[177] P. Salucci, C. Frigerio Martins, E. Karukes, R^n gravity is kicking and alive: The cases of Orion and NGC 3198, International Journal of Modern Physics D 23 (12) (2014) 1442005. arXiv:1405.6314, doi:10.1142/S021827181442005X.

[178] S. Carloni, P. K. S. Dunsby, S. Capozziello, A. Troisi, Cosmological dynamics of R**n gravity, Class. Quant. Grav. 22 (2005) 4839–4868. arXiv:gr-qc/0410046, doi:10.1088/0264-9381/22/22/011.

[179] G. G. L. Nashed, S. Capozziello, Constraining $f(\mathscr{R})$ gravity by Pulsar SAX J1748.9-2021 observations, Eur. Phys. J. C 84 (5) (2024) 521. arXiv:2405.09590, doi:10.1140/epjc/s10052-024-12866-8.

[180] S. Capozziello, V. F. Cardone, A. Troisi, Reconciling dark energy models with f(R) theories, Phys. Rev. D 71 (2005) 043503. arXiv:astro-ph/0501426, doi:10.1103/PhysRevD.71.043503.

[181] E. S. Fradkin, A. A. Tseytlin, Renormalizable asymptotically free quantum theory of gravity, Nucl. Phys. B 201 (1982) 469–491. doi:10.1016/0550-3213(82)90444-8.

[182] J. F. Donoghue, Leading quantum correction to the Newtonian potential, Phys. Rev. Lett. 72 (1994) 2996–2999. arXiv:gr-qc/9310024, doi:10.1103/PhysRevLett.72.2996.

[183] J. F. Donoghue, General relativity as an effective field theory: The leading quantum corrections, Phys. Rev. D 50 (1994) 3874–3888. arXiv:gr-qc/9405057, doi:10.1103/PhysRevD.50.3874.

[184] M. Reuter, H. Weyer, Running Newton constant, improved gravitational actions, and galaxy rotation curves, Phys. Rev. D 70 (2004) 124028. arXiv:hep-th/0410117, doi:10.1103/PhysRevD.70.124028.

[185] I. L. Shapiro, J. Sola, H. Stefancic, Running G and Lambda at low energies from physics at M(X): Possible cosmological and astrophysical implications, JCAP 01 (2005) 012. arXiv:hep-ph/0410095, doi:10.1088/1475-7516/2005/01/012.

[186] I. L. Shapiro, J. Sola, On the possible running of the cosmological 'constant', Phys. Lett. B 682 (2009) 105–113. arXiv:0910.4925, doi:10.1016/j.physletb.2009.10.073.

[187] C. Espana-Bonet, P. Ruiz-Lapuente, I. L. Shapiro, J. Sola, Testing the running of the cosmological constant with type Ia supernovae at high z, JCAP 02 (2004) 006. arXiv:hep-ph/0311171, doi:10.1088/1475-7516/2004/02/006.

[188] O. Bertolami, J. M. Mourao, J. Perez-Mercader, Quantum gravity and the large scale structure of the universe, Phys. Lett. B 311 (1993) 27–33. doi:10.1016/0370-2693(93)90528-P.

[189] J. T. Goldman, J. Perez-Mercader, F. Cooper, M. M. Nieto, The Dark matter problem and quantum gravity, Phys. Lett. B 281 (1992) 219–224. doi:10.1016/0370-2693(92)91132-S.

[190] D. C. Rodrigues, Elliptical galaxies kinematics within general relativity with renormalization group effects, JCAP 09 (2012) 031. arXiv:1203.2286, doi:10.1088/1475-7516/2012/09/031.

[191] D. C. Rodrigues, P. L. C. de Oliveira, J. C. Fabris, I. L. Shapiro, Disk and elliptical galaxies within renormalization group improved gravity, AIP Conf. Proc. 1471 (2012) 98–102. arXiv:1209.0504, doi:10.1063/1.4756820.

[192] C. Farina, W. J. M. Kort-Kamp, S. Mauro, I. L. Shapiro, Dynamics of the Laplace-Runge-Lenz vector in the quantum-corrected Newton gravity, Phys. Rev. D 83 (2011) 124037. arXiv:1101.5611, doi:10.1103/PhysRevD.83.124037.

[193] D. C. Rodrigues, P. L. de Oliveira, J. C. Fabris, G. Gentile, Modified gravity models and the central cusp of dark matter haloes in galaxies, Mon. Not. Roy. Astron. Soc. 445 (4) (2014) 3823–3838. arXiv:1409.7524, doi:10.1093/mnras/stu2017.

[194] E. Bhatia, S. Chakrabarti, S. Chakraborty, Velocity dispersion of dark-matter deficient ultradiffuse galaxies: A case for modified gravity, Phys. Rev. D 108 (6) (2023) 064021. arXiv:2306.11790, doi:10.1103/PhysRevD.108.064021.

[195] J. F. Navarro, C. S. Frenk, S. D. M. White, A Universal density profile from hierarchical clustering, Astrophys. J. 490 (1997) 493–508. arXiv:astro-ph/9611107, doi:10.1086/304888.

[196] A. A. Dutton, A. V. Macciò, Cold dark matter haloes in the Planck era: evolution of structural parameters for Einasto and NFW profiles, Mon. Not. Roy. Astron. Soc. 441 (4) (2014) 3359–3374. arXiv:1402.7073, doi:10.1093/mnras/stu742.

[197] P. A. R. Ade, et al., Planck 2015 results. XIII. Cosmological parameters, Astron. Astrophys. 594 (2016) A13. arXiv:1502.01589, doi:10.1051/0004-6361/201525830.

[198] J. Schombert, S. McGaugh, Stellar populations and the star formation histories of lsb galaxies: Iii. stellar population models, Publications of the Astronomical Society of Australia 31 (2014) e036.

[199] S. E. Meidt, et al., Reconstructing the stellar mass distributions of galaxies using S^4G IRAC 3.6 and 4.5 μm images: II. The conversion from light to mass, Astrophys. J. 788 (2014) 144. arXiv:1402.5210, doi:10.1088/0004-637X/788/2/144.

[200] D. Foreman-Mackey, D. W. Hogg, D. Lang, J. Goodman, emcee: the mcmc hammer, Publications of the Astronomical Society of the Pacific 125 (925) (2013) 306.

[201] G. Schwarz, Estimating the Dimension of a Model, Annals of Statistics 6 (2) (1978) 461–464.

[202] G. A. Mamon, A. Biviano, G. Boué, Mamposst: Modelling anisotropy and mass profiles of observed spherical systems–i. gaussian 3d velocities, Monthly Notices of the Royal Astronomical Society 429 (4) (2013) 3079–3098.

[203] D. Foreman-Mackey, D. W. Hogg, D. Lang, J. B. Goodman, emcee: The mcmc hammer, Publications of the Astronomical Society of the Pacific 125 (2012) 306 – 312.
URL https://api.semanticscholar.org/CorpusID:88518555

[204] M. A. Beasley, I. Trujillo, Globular clusters indicate that ultra-diffuse galaxies are dwarfs, The Astrophysical Journal 830 (1) (2016) 23.

[205] C. Yozin, K. Bekki, The quenching and survival of ultra diffuse galaxies in the coma cluster, Monthly Notices of the Royal Astronomical Society 452 (2015) 937–943.
URL https://api.semanticscholar.org/CorpusID:119234097

[206] O. Agertz, A. V. Kravtsov, On the interplay between star formation and feedback in galaxy formation simulations, Astrophys. J. 804 (1) (2015) 18. arXiv:1404.2613, doi:10.1088/0004-637X/804/1/18.

[207] A. E. Reines, J. E. Greene, M. Geha, Dwarf Galaxies with Optical Signatures of Active Massive Black Holes, Astrophys. J. 775 (2013) 116. arXiv:1308.0328, doi:10.1088/0004-637X/775/2/116.

[208] Y. Fujita, Pre-processing of galaxies before entering a cluster, Publ. Astron. Soc. Jap. 56 (2004) 29. arXiv:astro-ph/0311193, doi:10.1093/pasj/56.1.29.

[209] R. G. Abraham, P. G. van Dokkum, Ultra–Low Surface Brightness Imaging with the Dragonfly Telephoto Array, Publ. Astron. Soc. Pac. 126 (935) (2016) 55–69. arXiv:1401.5473, doi:10.1086/674875.

[210] L. Hernquist, An Analytical Model for Spherical Galaxies and Bulges, 356 (1990) 359. doi:10.1086/168845.

[211] P. G. van Dokkum, A. Wasserman, S. Danieli, R. G. Abraham, J. P. Brodie, C. Conroy, D. A. Forbes, C. D. Martin, M. J. Matuszewski, A. J. Romanowsky, A. Villaume, Spatially resolved stellar kinematics of the ultra-diffuse galaxy dragonfly 44. i. observations, kinematics, and cold dark matter halo fits, The Astrophysical Journal 880 (2019).
URL https://api.semanticscholar.org/CorpusID:119185644

[212] J. Freundlich, B. Famaey, P. Oriá, M. Bílek, O. Müller, R. Ibata, Probing the radial acceleration relation and the strong equivalence principle with the coma cluster ultra-diffuse galaxies, Astronomy & Astrophysics (2021).
URL https://api.semanticscholar.org/CorpusID:237485478

[213] G. Gentile, B. Famaey, W. J. G. de Blok, THINGS about MOND, Astron. Astrophys. 527 (2011) A76. arXiv:1011.4148, doi:10.1051/0004-6361/201015283.

[214] B. Famaey, J. Binney, Modified Newtonian dynamics in the Milky Way, Mon. Not. Roy. Astron. Soc. 363 (2005) 603–608. arXiv:astro-ph/0506723, doi:10.1111/j.1365-2966.2005.09474.x.

[215] C. M. Will, Theory and Experiment in Gravitational Physics, Cambridge University Press, 1993. doi:10.1017/CBO9780511564246.

[216] D. A. Wake, P. G. van Dokkum, M. Franx, Revealing velocity dispersion as the best indicator of a galaxy's color compared to stellar mass, surface mass density or morphology., The Astrophysical Journal 751 (2) (2012) L44. doi:10.1088/2041-8205/751/2/144.
URL https://doi.org/10.1088%2F2041-8205%2F751%2F2%2Fl44

[217] J. Binney, G. A. Mamon, M/L and velocity anisotropy from observations of spherical galaxies, or must M87 have a massive black hole ?, Mon. Not. Roy. Astron. Soc. 200 (1982) 361–375. doi:10.1093/mnras/200.2.361.

[218] L. Ciotti, G. Bertin, Analytical properties of the r^(1/m) luminosity law, Astron. Astrophys. 352 (1999) 447. arXiv:astro-ph/9911078.

[219] G. B. L. Neto, D. Gerbal, I. Marquez, The specific entropy of elliptical galaxies: an explanation for profile shape distance indicators?, Mon. Not. Roy. Astron. Soc. 309 (1999) 481. arXiv:astro-ph/9905048, doi:10.1046/j.1365-8711.1999.02849.x.

[220] P. Prugniel, F. Simien, The fundamental plane of early-type galaxies: non-homology of the spatial structure., AAP 321 (1997) 111–122.

[221] N. Y. Sotnikova, S. A. Rodionov, Anisotropic Models of Dark Halos, Astron. Lett. 34 (2008) 664–674. arXiv:0809.3946, doi:10.1134/S1063773708100022.

[222] B. Diemer, A. V. Kravtsov, A universal model for halo concentrations, Astrophys. J. 799 (1) (2015) 108. arXiv:1407.4730, doi:10.1088/0004-637X/799/1/108.

[223] H. Mo, F. C. van den Bosch, S. White, Galaxy Formation and Evolution, 2010.

[224] R. H. Wechsler, J. L. Tinker, The Connection between Galaxies and their Dark Matter Halos, Ann. Rev. Astron. Astrophys. 56 (2018) 435–487. arXiv:1804.03097, doi:10.1146/annurev-astro-081817-051756.

[225] I. Banik, H. Zhao, From Galactic Bars to the Hubble Tension: Weighing Up the Astrophysical Evidence for Milgromian Gravity, Symmetry 14 (7) (2022) 1331. arXiv:2110.06936, doi:10.3390/sym14071331.

[226] H. Haghi, P. Kroupa, I. Banik, X. Wu, A. H. Zonoozi, B. Javanmardi, A. Ghari, O. Müller, J. Dabringhausen, H. Zhao, A new formulation of the external field effect in MOND and numerical simulations of ultra-diffuse dwarf galaxies – application to NGC 1052-DF2 and NGC 1052-DF4, Monthly Notices of the Royal Astronomical Society 487 (2) (2019) 2441–2454. doi:10.1093/mnras/stz1465.
URL https://doi.org/10.10932%Fmnras2%Fstz1465

[227] B. Famaey, S. McGaugh, M. Milgrom, MOND and the dynamics of NGC 1052−DF2, Mon. Not. Roy. Astron. Soc. 480 (1) (2018) 473–476. arXiv:1804.04167, doi:10.1093/mnras/sty1884.

[228] P. D. Mannheim, D. Kazanas, Exact Vacuum Solution to Conformal Weyl Gravity and Galactic Rotation Curves, Astrophys. J. 342 (1989) 635–638. doi:10.1086/167623.

[229] P. D. Mannheim, Alternatives to dark matter and dark energy, Prog. Part. Nucl. Phys. 56 (2006) 340–445. arXiv:astro-ph/0505266, doi:10.1016/j.ppnp.2005.08.001.

[230] K. Dutta, T. Islam, Testing Weyl gravity at galactic and extra-galactic scales, Phys. Rev. D 98 (12) (2018) 124012. arXiv:1808.06923, doi:10.1103/PhysRevD.98.124012.

[231] T. P. Sotiriou, 6+1 lessons from f(R) gravity, J. Phys. Conf. Ser. 189 (2009) 012039. arXiv:0810.5594, doi:10.1088/1742-6596/189/1/012039.

[232] H. Motohashi, T. Suyama, Third order equations of motion and the Ostrogradsky instability, Phys. Rev. D 91 (8) (2015) 085009. arXiv:1411.3721, doi:10.1103/PhysRevD.91.085009.

[233] P. L. C. de Oliveira, J. A. F. Pacheco, G. Reinisch, Testing two alternative theories to dark matter with the milky way dynamics, General Relativity and Gravitation 47 (2015) 1–16.
URL https://api.semanticscholar.org/CorpusID:118410530

[234] R. B. Tully, J. R. Fisher, A New method of determining distances to galaxies, Astron. Astrophys. 54 (1977) 661–673.

[235] G. Bertone, D. Hooper, J. Silk, Particle dark matter: Evidence, candidates and constraints, Phys. Rept. 405 (2005) 279–390. arXiv:hep-ph/0404175, doi:10.1016/j.physrep.2004.08.031.

[236] A. J. Romanowsky, S. M. Fall, Angular momentum and galaxy formation revisited, The Astrophysical Journal Supplement Series 203 (2) (2012) 17.

[237] L. Amendola, D. Bettoni, A. M. Pinho, S. Casas, Measuring gravity at cosmological scales, Universe 6 (2) (2020) 20. arXiv:1902.06978, doi:10.3390/universe6020020.